



Technische Universität München  
TUM School of Life Sciences

## Three-dimensional imaging and modelling of the shape transition of faceted and non-faceted crystals

**Simon Alexander Schiele**

Vollständiger Abdruck der von der TUM School of Life Sciences der Technischen Universität München zur Erlangung des akademischen Grades eines Doktors der Ingenieurwissenschaften (Dr.-Ing.) genehmigten Dissertation.

**Vorsitzender:** Prof. Dr.-Ing. Timo Oksanen

**Prüfer der Dissertation:** 1. Prof. Dr.-Ing. Heiko Briesen  
2. Prof. Dr. Marco Mazzotti

Die Dissertation wurde am 03.02.2022 bei der Technischen Universität München eingereicht und durch die TUM School of Life Sciences am 13.05.2022 angenommen.



## Abstract

Crystallization is a common separation and purification process in various industries. Crystallization processes are dominated by complex dynamic interactions of crystallization phenomena like growth, nucleation, agglomeration and other physical phenomena like breakage and abrasion. These interactions are still not well understood. The present thesis deals with the influence of crystal shape on such interactions. Specifically, the interaction of crystal growth and damaging events was studied. This was done by continuing the development of three-dimensional imaging techniques for crystal shape and size analysis. In a first step, crystal populations were analyzed in three dimensions. The analysis showed that crystals underwent a shape transition from non-symmetric shapes to symmetric shapes. This transition could be explained by face-independent growth. However, at the time, it could not be explained how non-symmetric shapes could occur. The hypothesis was that damaged seed material did not grow according to established growth laws. The hypothesis motivated a second study in which growth of damaged crystals was studied. In crystallization processes, it is hard to avoid damage events like abrasion. Literature suggested that such crystals should grow at increased rates, but rates and mechanisms were not fully understood. In context of this work, three-dimensional imaging of abraded crystals enabled detailed analysis of their growth. The images were used to derive rates for a high-dimensional growth model that is able to describe the shape and size evolution of abraded crystals. The model was applied to describe how damaged seed material could lead to asymmetric crystals. In a broader picture, we have learnt that damage events in crystallization processes may not only affect processes by an increase of surface area for growth, but also render fast growing crystal surface.

## Zusammenfassung

Kristallisation ist ein gängiges Trenn- und Reinigungsverfahren in verschiedenen Industriezweigen. Das Verhalten von Kristallisationsprozessen wird von komplexen dynamischen Wechselwirkungen der Kristallisationsphänomene beherrscht. Diese Wechselwirkungen sind noch nicht gut verstanden. Diese Arbeit befasst sich mit dem Einfluss der Kristallform auf solche Wechselwirkungen. Insbesondere wurde die Wechselwirkung von Kristallwachstum und schädigenden Ereignissen untersucht. Dazu wurde die Entwicklung von dreidimensionalen Bildgebungsverfahren für die Kristallanalyse fortgesetzt. In einem ersten Schritt wurden Kristallpopulationen in drei Dimensionen analysiert. Dabei zeigte sich, dass die Kristalle einen Formübergang von asymmetrischen Formen zu symmetrischen Formen durchlaufen. Dieser Übergang konnte durch flächenunabhängiges Wachstum erklärt werden. Damals konnte jedoch nicht erklärt werden, wie die asymmetrischen Formen entstanden. Die Hypothese war, dass das beschädigte Impfmateriale nicht entsprechend der etablierten Wachstumsgesetzen wuchs. Diese Hypothese motivierte eine zweite Studie, in der das Wachstum von beschädigten Kristallen untersucht wurde. Bei Kristallisationsprozessen lassen sich Beschädigungen wie Abrieb nur schwer vermeiden. Die Literatur legt nahe, dass solche Kristalle mit erhöhten Raten wachsen, aber die Raten und zugrundeliegenden Mechanismen waren nicht vollständig verstanden. Im Rahmen dieser Arbeit ermöglichte dreidimensionale Bildgebung von abgeriebenen Kristallen eine detaillierte Analyse ihres Wachstums. Aus den Bildern wurden Raten für ein hochdimensionales Wachstumsmodell abgeleitet, das die Form- und Größenentwicklung von abgeriebenen Kristallen beschreibt. Das Modell wurde angewandt, um zu beschreiben, wie beschädigtes Impfmateriale zu asymmetrischen Kristallen wächst. Im Großen und Ganzen haben wir gelernt, dass Beschädigungen in Kristallisationsprozessen nicht nur durch eine Vergrößerung der Wachstumsoberfläche Prozesse beeinflussen können, sondern auch zu schnell wachsenden Kristalloberflächen führen.

## Danksagung

Vielen Dank an Sandra und den Rest meiner Familie für die immerwährende Unterstützung während der Promotionszeit.

Weiterhin möchte ich Heiko für die Möglichkeit danken, meine Promotion hier am Lehrstuhl zu absolvieren. Als besonders bemerkenswert empfinde ich, dass du immer erreichbar warst und auch sehr kurzfristig für Diskussionen Zeit gefunden hast.

Ich habe die Zeit hier nicht zuletzt wegen des freundschaftlichen Umgangs aller Mitarbeiter während und nach der Arbeit sehr genossen. Danke an alle und vor allen Martin. Ohne dich wäre alles doof. ♣△

Besonders möchte ich mich auch bei Michaela, Karin, Friederike, Walter und Sepp für die Unterstützung bedanken. Ohne eure Arbeit wäre meine Arbeit nicht möglich gewesen.

Vielen Dank auch an Heiko, Ramona und Mario für das Korrekturlesen und die vielen wertvollen Kommentare.



# Contents

<b>1.</b>	<b>Introduction</b> .....	<b>1</b>
<b>2.</b>	<b>Theoretical background</b> .....	<b>3</b>
2.1	The crystalline state .....	3
2.2	Crystallization as unit operation.....	3
2.3	Nucleation .....	5
2.3.1	Primary nucleation.....	5
2.3.2	Secondary nucleation .....	7
2.3.3	Seeding .....	7
2.4	Crystal growth .....	8
2.5	Breakage, attrition and abrasion.....	9
2.6	Crystal size, shape and morphology .....	9
2.6.1	Geometric crystal descriptions.....	10
2.6.2	Parametrization of geometric models.....	11
<b>3.</b>	<b>Problem definition</b> .....	<b>13</b>
<b>4.</b>	<b>Methodology</b> .....	<b>15</b>
4.1	Crystal shape and size analysis .....	15
4.1.1	Method for obtaining population data from 3D images.....	15
4.1.2	Method for tracking the growth of individual crystals.....	15
4.1.3	High dimensional Growth modelling.....	15
4.2	Paper I: Morphological Modelling and Simulation of Crystallization Processes (Schiele et al. 2020a) .....	16
<b>5.</b>	<b>Results</b> .....	<b>57</b>
5.1	Paper II: Analysis of Nonideal Shape Evolution during Potash Alum Crystallization Using Microcomputed Tomography and Three-Dimensional Image Analysis (Schiele et al. 2021a) .....	57
5.2	Paper III: Growth of abraded crystals tracked in three dimensions (Schiele et al. 2021b).....	71
<b>6.</b>	<b>Discussion</b> .....	<b>85</b>
6.1	3D methods for crystal population analysis .....	85
6.2	Studying interaction of crystallization phenomena .....	87
6.2.1	Abrasion and Growth.....	87
6.2.2	Breakage and Growth.....	88
6.2.3	Dissolution and Growth.....	89
6.2.4	Ostwald ripening.....	89
<b>7.</b>	<b>Conclusion</b> .....	<b>91</b>
	<b>Literature</b> .....	<b>V</b>
	<b>List of Publications</b> .....	<b>XIV</b>
	<b>Curriculum Vitae</b> .....	<b>XVI</b>



## List of Figures

Figure 1   Schematic of an exemplary crystallization process. ....	4
Figure 2   Illustration of disappearing faces through fast growth.....	8
Figure 3   2D Example of Miller indices (given in brackets) to describe the orientation of faces (represented as lines).....	11

## List of Abbreviations

$\mu$ CT	micro-computed tomography
2D	two-dimensional
3D	three-dimensional
API	active pharmaceutical ingredient
ATR-FTIR	attenuated total reflection Fourier transformed infrared spectroscopy
CNT	classical nucleation theory
DFG	Deutsche Forschungsgemeinschaft
FBRM	focused beam reflectance measurement
GRD	growth rate dispersion
SDG	size dependent growth

## List of Symbols

In this work, scalars and functions are written as symbols with normal font weight. Vectors are written as lower case symbols with bold font weight. Matrices are written as capital symbols with bold font weight.

This list is for chapters 1 and 2. The articles reprinted in chapters 4 and 5 have their own list of symbols.

<b>Symbol</b>	<b>Unit</b>	<b>Description</b>
$G$	m/s	Growth rate
$n$	-	Order of reaction
$\mathbf{n}$	-	Crystal face normal vector
$r, r_c$	m	Radius of nucleus, critical radius of nucleus
$T$	K	Temperature
$t$	s	Time
$w$	kg <sub>solute</sub> /kg <sub>solvent</sub>	load
$w^*$	kg <sub>solute</sub> /kg <sub>solvent</sub>	Saturation load
$\Delta G, \Delta G_S, \Delta G_V$	J/kg	Gibbs free energy, Gibbs surface and volume free energy respectively
$\Delta w$	kg <sub>solute</sub> /kg <sub>solvent</sub>	Absolute supersaturation
$\alpha$	rad	Angle between face normal vectors
$\sigma$	-	Relative supersaturation



# Chapter 1

## Introduction

Crystallization is a common unit operation in chemical, pharmaceutical and food processes. It is used to separate substances from solutions or melt. The great potential of crystallization lies in separation with high selectivity and high purity. This potential is opposed to complex dynamic interactions in crystallization processes that make them hard to predict and control. Basic phenomena that occur during crystallization are

- Nucleation – The formation of new crystals
- Growth – Incorporation of molecules or atoms in existing crystals
- Dissolution – Disintegration of molecules or atoms from existing crystals
- Agglomeration – The formation of complex geometric structures out of existing crystals
- Breakage – Shattering of crystals into pieces through intense mechanical stress
- Abrasion and Attrition – Damage induced through milder mechanical stress which leads to round crystal edges and corners

With the exception of nucleation (Myerson and Trout 2013; Zhou et al. 2019), these phenomena are well understood individually. However, their interactions are often not well understood and subject of recent research activities (Ma et al. 2008; Kovačević and Briesen 2019; Bötschi 2019; Ahn et al. 2021a, 2021b; Bosetti et al. 2021). The main working hypothesis of this thesis is that the lack of understanding is because crystal shape is often insufficiently considered. Crystal shape is a general term that describes the appearance of crystals. One essential component of shape is that it describes the relation of surface area and volume. Crystal shape is particularly important because crystal growth is a surface reaction that increases crystalline volume. The rate of this surface reaction depends on how much material is solved. Therefore, surface and volume of crystals are coupled. In addition, different types of surfaces exist and influence rates in processes.

In many crystallization processes, crystal growth is a dominating phenomenon. It is often the preferred separation phenomenon and many batch processes aim at maximizing growth while minimizing the other before mentioned phenomena. This is because growth leads to pure and large crystals. Purification is often a goal of crystallization and large crystals are easily handled in downstream processes. In order to describe crystal growth, one often assumes idealized crystal shapes that are described by perfectly faceted crystals (Briesen 2006; Ma and Wang 2008; Borchert and Sundmacher 2012; Borchert et al. 2014; Eisenschmidt et al. 2014; Reinhold and Briesen 2015; Eisenschmidt et al. 2016). The established growth model assumes that faces are displaced in a direction normal to their surface. Different faces lead to different growth behavior and hence different process behavior (Puel et al. 1997; Reinhold and Briesen 2015). Therefore, crystal shape is long accepted as important process variable.

However, in reality idealized growth behavior is seldom achieved. That is, crystals may significantly deviate from their idealized shapes depending on which other phenomena occur. For example, crystallization vessels are agitated in order to reduce temperature and concentration gradients. The corresponding fluid dynamical conditions impose mechanical stress on crystals and lead to their damage and secondary nucleation (i.e. production of fine material). In continuous crystallization processes (e.g. mixed suspension mixed product removal), particles would be washed out of the system over

time if no nucleation occurred. Nucleation is, therefore, needed to keep continuous processes running. In such cases, nucleation must be induced e.g. through abrasion or milling of suspended crystals. Nuclei are composed of only a few dozens of atoms or molecules. For such small numbers it is inherently hard to achieve faceted shapes and it may even be hard to define a distinct phase boundary (Zhou et al. 2019). On larger size scales, broken crystals may deviate from idealized faceted shapes (Hill and Reeves 2019; Ma and Roberts 2019), dissolution (Eisenschmidt et al. 2016; Elts et al. 2016) or abrasion (Reinhold et al. 2015) yield rounded shapes, and agglomeration leads to complex geometric structures (Kovačević 2018). Such shape deviations make the common growth laws inapplicable. In consequence, it is likely that non-ideally shaped crystals affect behavior of crystallization processes differently as predicted by assuming ideal shapes. In addition, breakage (Hill 2004), abrasion (Briesen 2007) and dissolution (Snyder and Doherty 2007) not only affect shape, but are also affected by shape. It is hence evident that crystal shape is an important crystal property and process variable when describing dynamic interactions between crystallization phenomena and that it is important to consider non-ideal shapes.

In addition to shape as process variable, the shape of crystals is an important quality criterion of a crystalline product as well (Buffham 2000; Tung 2012; Dandekar et al. 2013). Shape has a decisive influence on the bioavailability of active pharmaceutical ingredients (APIs) (Blagden et al. 2007; Dandekar et al. 2013) and on the efficiency of further downstream processes like solid/liquid separation and drying (Variankaval et al. 2008; Beck and Andreassen 2012; Cornehl et al. 2014).

As mentioned earlier, crystal growth is often promoted and abundant in crystallization processes. Understanding growth is, therefore, an important engineering task in order to predict and control crystallization processes. In addition, growth of nuclei is considered an important topic that may help to understand crystal nucleation (Myerson and Trout 2013). However, growth of non-ideally shaped crystals (i.e. not faceted crystals) is not studied much in the literature. Ma and Roberts (2019) modeled growth of broken crystals. However, the shape of the crystals was highly simplified by the assumption that all broken crystals broke in the same way. The assumption was that all broken crystals had the same new face. They further assumed that this face would grow as any other face but at an arbitrarily higher rate. Their study showed that fast growth resulted in healing of broken regions within seconds. However, they discussed that the rates that were applied for the broken region should be experimentally determined. In addition, it is unknown whether growth laws of ideal faces can be applied to damaged regions. Increased growth rates are according to experimental studies that have shown that damaged crystals grow at increased rates in terms of increase of mass (Ulrich and Stepanski 1987).

In consequence, the present thesis focuses on the influence of crystal shape on crystallization processes. Specifically, the interaction of crystal growth and damage events during crystallization from solution are studied.

- **Chapter 2** motivates this work and summarizes crystallization basics.
- **Chapter 3** defines the problem that is tackled in the present work.
- **Chapter 4** summarizes methods that have been developed and applied in context of this work and explains the preliminary work done by Reinhold (2015) and Kovačević (2018) within DFG priority program SPP 1697. That work laid the theoretical foundation of the methods developed and the results obtained in context of the present thesis.
- **Chapter 5** combines the results that advance towards a solution of the defined problems.
- **Chapter 6** discusses the progress of this work
- **Chapter 7** concludes the present thesis

## Chapter 2

# Theoretical background

### 2.1 The crystalline state

In a crystalline phase, molecules or atoms are aligned according to a material specific lattice. The term *crystal* describes a crystalline particle. The term *crystallization* describes a phase transition into a crystalline state. Crystallization may occur in unordered phases (e.g. solutions, melts, amorphous solids) or in crystalline phases (Mullin 2001). In latter case, aligned molecules align according to another, more stable crystal lattice (polymorphism). The term *crystallization* is also used to describe a unit operation that uses the phase transition crystallization for material separation. Ideally, only molecules that fit into the crystal lattice are included in crystals, due to the ordered alignment of molecules in crystalline phases. This is why high purity and selectivity can be achieved and crystallization is used as purification technique.

### 2.2 Crystallization as unit operation

The present work focuses on crystallization from solution. In this case, a solution of a material is present. The solution consists of a *solute* (material to be crystallized), a *solvent* (liquid in which the solute is solved) and potentially other components that are dissolved, too. To induce crystallization, the thermodynamic potential of the solution is altered in such a way that the formation of a crystalline phase becomes thermodynamically favorable. This is expressed by the term *supersaturation*. Mathematically supersaturation can be expressed as relative supersaturation  $\sigma$

$$\sigma = \frac{w}{w^*} - 1 \quad 1$$

In equation 1,  $w$  is the load of solute in solution.  $w^*$  is the corresponding solubility. Instead of using concentration defined as amount of material solved per solution volume, it is common practice to use load  $w$  with the unit mass solute per mass solvent for crystallization. Using load makes calculations simpler because solution volume changes through crystallization. The mass of solvent, however, is easily calculated from mass balances and is constant in many cases. Conversion of solvent mass to volume of solution needs information on the density, which changes through crystallization as well and often needs experimental data. In the following, the term concentration is used as general term to describe how much of a certain material is dissolved. The mathematical formulation may be in form of a load or any type of concentration (e.g. mass or mole based concentration).

Solubility  $w^*$  is generally a function of thermodynamic state variables (e.g. temperature, composition). For  $\sigma > 0$  a solution is super-saturated and thermodynamically unstable. But the state may be meta-stable at low supersaturation. Crystallization may occur. For  $\sigma = 0$  a solution is saturated i.e. the solution is in thermodynamic equilibrium. For  $\sigma < 0$  a solution is under-saturated. The under-saturated state enables dissolution. The same relations apply for the absolute supersaturation  $\Delta w$

$$\Delta w = w - w^* \quad 2$$

Because supersaturation is the driving force in crystallization, measuring supersaturation is highly desirable. However, a direct and explicit sensor for it does not exist. In order to determine supersaturation, the concentration of solute has to be measured together with the state variables that define saturation. The saturation has to be measured as function of relevant state variables in laborious experiments if no data

is available in the literature. Then equations 1 or 2 can be used to calculate supersaturation. Calibration of concentration measurements may be altered by possibly unknown impurities. This makes concentration measurements for solubility measurements and process monitoring especially challenging. Concentrations are often measured using refractometry (Mullin 2001; Alvarez Rodrigo et al. 2004; Mimouni et al. 2005), conductivity (Mullin 2001; Schiele et al. 2021a) or spectroscopy (Nagy et al. 2013; Eisenschmidt et al. 2016; Eder and Briesen 2019; Rao et al. 2020; Schiele et al. 2020b).

For example, Schiele et al. (2020b) describe how lactose concentrations can be measured for its crystallization using attenuated total reflection fourier transformed infrared spectroscopy (ATR-FTIR)<sup>1</sup>. In lactose crystallization, two anomers of lactose are present in solution, and are in dynamic equilibrium. However, only one of them— $\alpha$ -lactose—crystallizes due to its lower solubility at common process conditions. Hence, the individual concentration and supersaturation of  $\alpha$ -lactose needs to be measured. The anomers have very similar physiochemical properties and are, therefore, hard to distinguish using classical calibration methods. ATR-FTIR spectra of the anomers are similar but can be distinguished using suitable calibration (Schiele et al. 2020b). This illustrates that supersaturation is not always easily accessible. Still it is the driving force of crystallization and hence an important process variable.

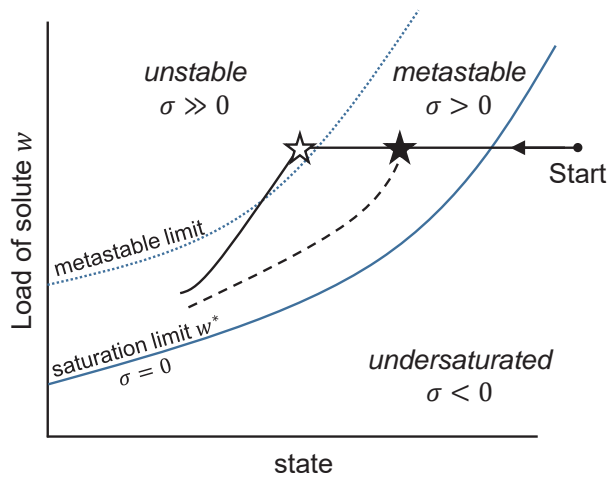


**Figure 1 | Schematic of an exemplary crystallization process.**

Figure 1 shows a crystallization process that starts in the top right of the schematic and follows the black line in direction of the arrow. The first step is to generate supersaturation by changing the state of the system. Independently of how (or if) supersaturation is measured, there are different ways how supersaturation can be achieved and/or maintained:

- reducing solubility (decreasing  $w^*$  in eq. 1)
  - altering temperature (e.g. cooling crystallization<sup>2</sup>)
  - altering pH (pH-shift crystallization)
  - addition of antisolvent (antisolvent crystallization)
- increasing concentration (increasing  $w$  in eq. 1)
  - removal of solvent (e.g. evaporation crystallization)
  - reactions (integrated crystallization)

<sup>1</sup> The work of Schiele et al. (2020b) was conducted in context of this PhD work. However, it is not included in the present thesis because it does not deal with the shape of crystals.

<sup>2</sup> Note that some material systems (e.g. Calcium Carbonate in water) have lower solubility at elevated temperatures and can be crystallized through an increase of temperature.

Which of these methods is used in technical applications depends on the material system and process requirements. However, all methods have in common that a supersaturation is induced and thermodynamics drive the system towards a saturated solution. Once supersaturation is generated, crystallization can occur. In principal, this can happen through two pathways:

- Nucleation i.e. formation of new crystals and
- Crystal growth i.e. deposition of molecules to present crystal surfaces.

In Figure 1, initially, no change in load is achieved, because no crystalline phase is present. The phase can either be added (*seeding*, black star in Figure 1) or occurs spontaneously at high supersaturation (*primary nucleation*, white star in Figure 1) around the metastable limit. The metastable limit should be thought of a region rather than a strict limit. It depends on many factors including how fast the state is changing and is not fully understood, yet (see section 2.3). Once a crystalline phase is present, growth can occur in order to equilibrate the solution. If the state further changes, supersaturation is maintained and the process is driven towards a low final load until thermodynamic equilibrium is reached. The pathway that is taken by a process is dominated by complex dynamic interactions of the different crystallization phenomena that are discussed in the following sections. That is, this work aims to improve the understanding of these interactions by considering crystal shape.

## 2.3 Nucleation

Nucleation is a phenomenon in which a new phase is generated from a supersaturated initial phase. *Nucleus* (pl. *Nuclei*) is a term that refers to a new—initially small—particle of the new phase. Nucleation occurs in all phase transitions, including crystallization. In general, nucleation results in a change of density. However, nucleation of crystals is more complex because molecules need to align according to the crystal lattice in addition to the change in density. This interplay between change in density and alignment during nucleation is the reason why nucleation of crystals is not yet fully understood (Zhou et al. 2019).

Nucleation is divided into two main groups. A) primary and B) secondary nucleation. Primary nucleation can again be divided into two subgroups: A.1) homogeneous and A.2) heterogeneous nucleation.

### 2.3.1 Primary nucleation

In primary nucleation, nuclei are generated from solutions where no crystals of the solute are present.

#### Homogeneous nucleation

One speaks of homogeneous nucleation when nuclei are generated from clear solutions and nuclei are made of only the solute. Today, homogeneous nucleation from solution is not fully understood. Research on primary nucleation is abundant. A comprehensive summary would be out of the scope of this text. In context of the present work, a summary of the most basic version of nucleation theory and a summary of some recent progress on the topic should suffice.

Most theory is based on Gibbs' classical nucleation theory (CNT) which was initially designed for vapor condensation but is also employed for liquid/solid phase transitions (e.g. Crystallization, (Fokin and Zanotto 2000; Ahn et al. 2021a)).

According to the theory, molecules aggregate through local concentration fluctuations due to Brownian motion, to form vapor droplets. In a supersaturated environment it is energetically favorable to form a new phase. Hence a phase transformation energy is released (volume free energy  $\Delta G_V \propto r^3$ ) when molecules aggregate. At the same time a new phase boundary is generated. The formation of a phase boundary costs energy

(surface free energy  $\Delta G_S \propto r^2$ ). The sum of these two energies decides whether it is thermodynamically favorable to form a new phase or not and is a function of nuclei size.

$$\Delta G(r) = \Delta G_S(r) + \Delta G_V(r) \quad 3$$

For small nuclei (small radius  $r$ ) the surface energy is larger than the phase transition energy. With increasing size, the phase transition energy becomes larger than the surface energy. The total free energy  $\Delta G$  has a maximum and becomes negative for even larger nuclei. The size where the total energy has its maximum is called critical nuclei size  $r_c$ . For nuclei that are smaller than  $r_c$ , disintegration into the initial phase is thermodynamically more favorable. Nuclei larger than  $r_c$  favor growth and are hence stable.

This model assumes that density and surface tension of a nucleus are size independent (i.e. capillary assumption), isotropic and that the nucleus is spherical. In addition, the growth of nuclei is assumed to entirely rely on addition of single molecules to a growing nucleus and ignores merging or division of nuclei. Further, for applications to crystallization, CNT ignores the fact that to form crystalline solids molecules do not only need to aggregate but also need to align according to the crystal lattice. In consequence, CNT yields poor results in crystallization and in some cases may not even qualitatively describe nucleation of crystals (Erdemir et al. 2009).

Therefore, more advanced non-classical nucleation theories are developed (Vekilov 2019). One family of such advanced theories are the so called two-step (Kashchiev et al. 2005; Erdemir et al. 2009) or multi-step nucleation mechanisms (Wang et al. 2014). Therein, one assumes that not only the density is a distinctive feature of a nuclei but also its structuredness. Erdemir et al. (2009) suggest that as an initial step in nucleation disordered clusters are formed. As further steps in the nucleation pathway molecules may pass several conformations until they reach their stable crystalline conformation and a crystal nucleus is generated.

Zhou et al. (2019) were able to capture the solid-solid phase transition in three dimensional images of crystals on atomic level over time with electron atomic tomography. They induced phase transitions within the crystals through heating (annealing) and identified nucleation sites where the atoms in the crystals would start to rearrange to form different crystal polymorphs. They found that these nuclei grow, fluctuate in size or dissolve. For some of the nuclei, merging and division was observed. In a next step, they calculated a structuredness parameter for each atom in the crystal lattice and found that the overall structuredness of nuclei increased during the annealing process. They further showed that a gradient from an ordered center of the nuclei to its unordered outside was present. These experimental results show that indeed (A) structuredness plays an important role in nucleation, (B) nuclei are anisotropic and (C) that some nuclei would not only grow or dissolve, but could also divide, merge or fluctuate between growth and dissolution. All these three phenomena cannot be described by CNT (Zhou et al. 2019). In contrast to what is assumed in two-step nucleation theories, nucleation seems to be a continuous process where an increase in structuredness over time and space along with change of the size of a nucleus is observed rather than a two-step phenomenon where first aggregation and then rearranging of aggregated molecules occurs.

While Zhou et al. (2019) studied a solid-solid phase transition experimentally, Wiedenbeck et al. (2019) studied the crystallization from solution of the API ibuprofen. They found that ibuprofen solutions first undergo a liquid-liquid phase separation. A dense liquid ibuprofen intermediate phase is kinetically stabilized due to high viscosity giving time for rearrangement of the molecules into a crystal lattice. Similar studies propose more complex nucleation pathways that may describe nucleation of certain materials.

In context of interpreting experimental data on nucleation, Ahn et al. (2021a) discuss that cluster formation reduces the concentration of molecules in solution. For material systems in which clusters are easily formed, the concentration of free molecules may be significantly lower than estimated with clusters neglected. Hence, different parameters may be identified from the same experiments depending on whether clusters are considered or not. The authors state that their work is discussed in context of two-step nucleation, however, calculations were done based on CNT. The results are, therefore, only qualitative.

In conclusion, nucleation is not fully understood and research is ongoing.

### **Heterogeneous nucleation**

In heterogeneous nucleation some sort of foreign surface is in contact with a supersaturated solution. Molecules need to overcome a smaller energy barrier to attach to such surfaces since less surface free energy is needed (Kelton and Greer 2010). In consequence, heterogeneous nucleation can accelerate nucleation processes. Such foreign surfaces may be provided by particles of a substance other than the solute or may even be a scratch in the reactor.

#### **2.3.2 Secondary nucleation**

Secondary nucleation occurs when crystals are already present in solution. In most crystallization processes slurries are somehow agitated and, therefore, crystals in a process have a momentum in the direction of the flow. Gahn and Mersmann explain secondary nucleation through impact of crystals on reactor internals like stirrer blades or baffles (Gahn and Mersmann 1999a, 1999b). Additionally, the presence of solute crystals may also decrease the energy barrier for nucleation in their vicinity (Bosetti et al. 2021; Ahn et al. 2021b).

#### **2.3.3 Seeding**

As discussed above, the exact mechanisms involved in primary nucleation are not yet well understood. It is hard to control and hence effort is made to avoid it in many processes. One concept to avoid primary nucleation in order to gain controllability of crystallization processes is *seeding*. Seeding describes the addition of crystals to a supersaturated solution. In some cases, seeding is used to define the starting point of crystallization by inducing secondary nucleation (Mullin 2001; Guu and Zall 1991). In other studies, the aim is to prevent nucleation and to predominantly grow the seed crystals (Aamir et al. 2010; Chung et al. 1999; Schiele et al. 2021a). Another important goal of seeding is to obtain a certain crystal polymorph that may not nucleate spontaneously (Beckmann 2000). Seeding is considered as the most favorable method to start crystallization processes (McLeod et al. 2011).

Seeds have two important properties. (A) The amount of seeds that is added and (B) their appearance that is often described with a size distribution. It was mentioned before, and will be discussed in greater detail later in this text, that a description of the appearance by size alone is not sufficient. However, in the literature shapes of seed crystals are largely ignored.

Chung et al. (1999) found that seeding has an immense effect on the course of crystallization. They found that seeding has a greater effect on the final size distribution in modeled batch cooling crystallization of potassium nitrate in water than the supersaturation trajectory. Aamir et al. (2010) defined multi modal target crystal size distributions and temperature profiles. They then used a crystallization model to calculate seed distributions that would produce the target size distributions by following the predefined temperature profile. These calculations were also validated by experiments (Aamir et al. 2010). Rachah and Noll (2015) studied the effect of seeding for modeled fed-batch lactose crystallizations. They optimized both seed size distribution and temperature profile of the cooling jacket to produce crystals with narrow particle size distributions and high mean diameter. In an experimental study Guu and

Zall (1991) found that seeding leads to higher yields in lactose crystallization. In a more recent study, Simone et al. (2019) experimentally determined the effect of seeding in batch cooling crystallization of lactose on size, morphology, yield, crystal structure and anomeric purity of the produced crystals. They found that seeding can produce very pure (97 %  $\alpha$ -lactose) crystals with unimodal size distribution. Only little agglomeration occurred. The yield of seeded cooling crystallization, however, was below 60 % while yields above 90 % could be achieved with antisolvent crystallization.

## 2.4 Crystal growth

Crystal growth occurs in supersaturated solutions at phase boundaries between solution and crystalline phase. Solute molecules align according to the crystal lattice and are built in the lattice. On the micro scale, faces grow in a direction normal to their surface. The rate of growth increases with increasing supersaturation and—usually to a lesser extent—with increasing temperature. The growth rate also depends on the orientation of a face in respect to the crystal lattice: faces grow at face specific rates. This is called face dependent growth. Growth rates ( $G$ ) are often expressed by an empirical exponential growth law (Mullin and Garside 1967a; Ma et al. 2012; Borchert et al. 2014)

$$G = G_0(T) \cdot \sigma^n \quad 4$$

$G_0(T)$  is a face specific rate constant that may be temperature dependent. Its unit is unit length per unit time. The order  $n$  of the reaction is not necessarily an integer value.

In theory, infinitive number of face directions are possible. However, in reality, only few faces are observed for a given crystal. Figure 2 illustrates that this is because faces disappear through fast growth. In the figure it is assumed that at  $t_0$  (dark grey) two kinds of faces are expressed: a horizontal one growing at a fast rate (indicated by long growth vectors with length  $G_{fast}$ ) and diagonal ones growing at a slower rate (indicated by short growth vectors with length  $G_{slow}$ ). Within a time  $\Delta t$ , the faces are displaced by these vectors and the horizontal face becomes smaller. As growth continues, the horizontal face becomes even smaller and finally vanishes ( $t = t_0 + 2\Delta t$ ).

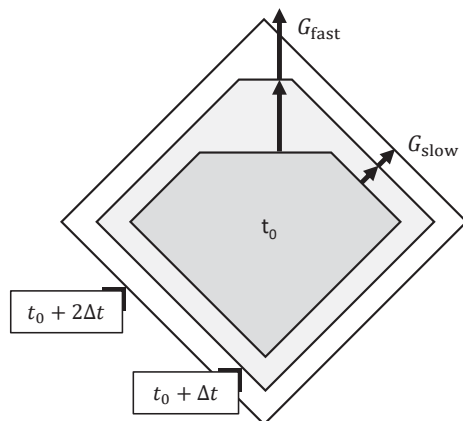


**Figure 2 | Illustration of disappearing faces through fast growth**

Whether a face disappears or not depends on the relation of growth rates and the angle between the growth vectors. Mullin and Garside (1967a) derive that for

$$\frac{G_{fast}}{G_{slow}} > \frac{1}{\cos \alpha} \quad 5$$

the fast growing face disappears. Where  $\alpha$  is the angle between the normal vectors ( $\alpha = 45^\circ$ , in Figure 2). Growth of a crystal in terms of mass is, therefore, often not affected by the growth of the fast growing faces, but of that of the slowly growing faces.

This idealized model applies to faceted crystals. It is discussed in the introduction that other crystallization phenomena may yield crystal shapes that do not correspond to the ideally faceted model. Growth of non-faceted crystals has not been well studied in the literature. In one of the few studies that address growth of non-ideally shaped crystals Ma and Roberts (2019) consider growth of broken crystals by considering an additional face that grows at an arbitrarily chosen higher rate. The authors discuss that such a rate should be experimentally determined in order to quantitatively consider the dynamic interaction of crystal growth and breakage. This thesis aims at improving the understanding of the interaction of growth and damage events by considering shape as a variable.

## 2.5 Breakage, attrition and abrasion

Breakage, attrition and abrasion are terms that describe damage of particles. Breakage describes events through which a particle is shattered into numerous pieces such that the original particle (parent particle) cannot be easily identified. For attrition and abrasion, in contrast, the original crystal remains identifiable as such and only minor but relevant changes in size and shape occur. Attrition is caused by contacts of crystals with e.g. the stirrer of a reactor or impeller of a pump. Crystal-crystal contacts cause abrasion.

Breakage, attrition and abrasion are phenomena that are not limited to crystallization and are discussed in the literature predominately for particles in general. A comprehensive study of attrition of crystals was conducted by Gahn and Mersmann (1999a; Gahn and Mersmann 1999b). They calculated a loss in volume in case of impact of a parent particle based on measurable material properties and crystal mass. In addition, they derived a formulation for the size distribution of the fragments (Gahn and Mersmann 1999a). These formulations were then used for process simulations (Gahn and Mersmann 1999b). Briesen (2007) extended the model to account for different geometries and considered the effect of shape on attrition in processes by means of population balance modelling in another study (Briesen 2009). Growth was considered but assumed to have no effect on crystal shape. That is, shapes that result from damaging events often do not correspond to the idealized faceted shape (Reinhold et al. 2015; Hill and Reeves 2019). It is currently not fully understood how such crystals would grow.

## 2.6 Crystal size, shape and morphology

Details on the importance of shape in crystallization are explained by Schiele et al. (2020a) (Chapter 4) and have been discussed in the previous sections. Here, the key facts are summarized.

*Form, shape, morphology* and *habit* are terms that are used to describe the appearance of crystals. However, terminology is quite inconsistent. The quote “morphology and shape have been used interchangeably, and we do the same here.” (Dandekar et al. 2013) shows that little effort is made towards consistent terminology. In this text, *form* describes the appearance of crystals in respect to which crystal faces are expressed (i.e. polymorphic form). *Shape* in contrast, describes the appearance in a more general context to describe whether a crystal is for example needle shaped, spherically or a cuboid. In the literature, *morphology* (Borchert and Sundmacher 2012) or *habit* (Mullin 2001; Puel et al. 1997) are found as synonyms for *shape*. *Habit* is primarily used to refer to faceted shapes.

For particles in general, it is common to assume a spherical shape when measuring their size. In such cases, the size can be conveniently described through a diameter. For spheres, this measure is exact and can be used to calculate particle properties such as volume and surface area. However, it is quite obvious that most particles—especially

crystals—are not spherical. Spherical particle models are often chosen because there is either no information on shape, or shapes are too complex to be described accurately. In some cases, the errors made through such assumptions are low. Describing crystals by spheres is usually not sufficiently accurate (Reinhold 2015; Kovačević 2018).

Depending on the crystal lattice and resulting growth rates, a crystal has defined faces that may appear in a crystal. The form describes which of these faces are present. The shape of crystals is then defined by—among other factors to be discussed later—how large the faces are. In this respect it is important to know that fast growing surfaces tend to disappear and those faces that grow slower will dominate shape (see section 2.4). In context of this work, *ideal shape* describes faceted crystals that are symmetric according to their unit cell. Agglomeration (Kovačević and Briesen 2019), nucleation (section 2.3), and damage (section 2.5) may yield shapes that can usually not be described by faces. Such shapes are discussed in chapters 3, 4 and 5 and are referred to as *non-ideal shapes*.

One reason for that shape has a decisive influence on crystallization processes is that crystal growth is a surface reaction. Growth rates depend on the surface itself and how much solute is solved (i.e. supersaturation). Therefore, the evolution of crystal surface and crystal volume are coupled. In order to describe a crystallization process, both crystal volume and surface area need to be accurately described. For example, face dependent growth may occur and hence different types of surface need to be considered (Zhang and Doherty 2004; Snyder and Doherty 2007; Reinhold and Briesen 2015; Puel et al. 2003). Face dependent growth can be considered using ideal shape models. However, matters become more complex when non-ideal crystal shapes occur.

Section 2.5 discusses that damaging events render non-ideal shapes and section 2.3 explains that nuclei are usually also not faceted. Agglomerates may be faceted but are concave and hence considered non-ideal as well (Kovačević and Briesen 2019). In consequence, assuming convex, faceted shapes is often inaccurate because damage, nucleation and agglomeration are common in crystallization processes. In addition, damaging events are themselves affected by shape (Hill and Reeves 2019; Briesen 2007, 2009). In consequence, the commonly assumed growth laws for faceted shapes do often not apply. It is hence evident that crystal shape is an important crystal property and process variable when describing dynamic interactions between crystallization phenomena and that it is important to consider non-ideal shapes.

Crystal shape may also be an important product quality criterion. It influences bulk properties like compressibility, filterability, tendency to cake, or flow ability of a powder (Buffham 2000; Tung 2012; Dandekar et al. 2013; Variankaval et al. 2008; Beck and Andreassen 2012; Cornehl et al. 2014). In the case of APIs, shape and polymorphic form affect bioavailability (Blagden et al. 2007; Dandekar et al. 2013).

### **2.6.1 Geometric crystal descriptions**

Along with such findings, the framework of crystal shape engineering (Lovette et al. 2008) has emerged. In consequence, the need for crystal shape analysis has developed.

Instead of using only one size parameter (e.g. diameter or length), it is common to use additional geometric parameters to describe crystal shapes (Garside and Ristić 1983; Puel et al. 1997; Puel et al. 2003; Schorsch et al. 2014; Heisel et al. 2017; Ma and Roberts 2019; Bötschi et al. 2019). Shape factors such as an aspect ratio are one typical way of introducing a geometric property. Hill and Reeves (2019) used an aspect ratio to study the effect of breakage of cuboid crystals on their shape. In the case of needle shaped crystals one can measure the size of the needles as their length and describe their thickness using an aspect ratio (Ma and Roberts 2019). This is a very similar approach to those of Puel et al. (2003), Schorsch et al. (2014) and Bötschi et al. (2019) where two lengths are used to describe cuboid crystals. Other shape factors include the

roundness (Reinhold et al. 2015) or sphericity (Snyder et al. 2007) of crystals. It is possible to distinguish between fundamentally different shapes using shape factors (Heisel et al. 2017). However, such methods often oversimplify crystal shape and may only provide little understanding of the underlying crystallization phenomena.

Researchers have, therefore, tried to find more meaningful shape representations. For crystals, Miller indices have long been established (Mullin 2001). They are used to describe the orientation of crystal faces. The Miller index of a face is given as normal vector of a face that is multiplied with a scalar to produce a vector of the smallest possible integers. A two-dimensional (2D) example of this representation is given in Figure 3. Therein, a normal vector of the green line is  $\mathbf{n} = (0 \ 1)^T$ . It is multiplied by 1 to yield the Miller index  $[0 \ 1]$ . The normal vector of the blue line is  $\mathbf{n} = (0.7 \ 0.7)^T$ . It is multiplied by 1.4 to yield the Miller index  $[1 \ 1]$ . The normal vector of the orange line is  $\mathbf{n} = (0.4 \ 0.9)^T$ . It is multiplied by 2.2 to yield the Miller index  $[1 \ 2]$ . The same principle can be applied to three-dimensional (3D) cases.

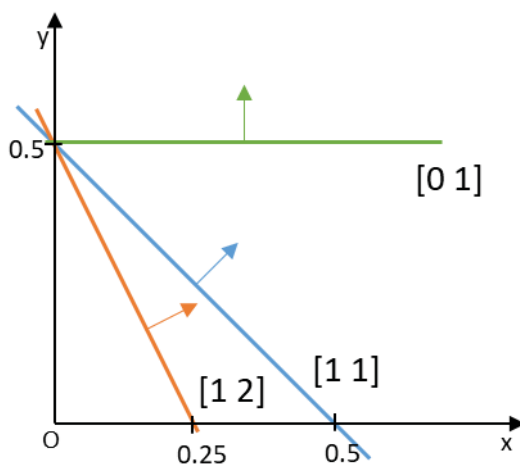


**Figure 3 | 2D Example of Miller indices (given in brackets) to describe the orientation of faces (represented as lines)**

A disadvantage of this representation is that it describes only the form of crystals. There is no size and hence no shape information included. An extension of the representation through Miller indices is the mathematical concept of so called H- or V-representations which are explained in chapter 4, in detail. These representations are used to describe ideal crystal shapes.

Non-ideal shapes can be accounted for by considering additional faces that would not occur according to the form of a crystal (Briesen 2009; Ma and Roberts 2019). Multiple H-representations can be used for the description of agglomerates (Kovačević et al. 2017; Kovačević and Briesen 2019). Spheres can be added to V-representations according to Reinhold et al. (2015) for the description of abraded crystals. Chapter 4 summarizes how H- and V-representations are applied for non-ideal shape description.

## 2.6.2 Parametrization of geometric models

State of the art methods use 2D image analysis for shape analysis (Larsen et al. 2007; Borchert and Sundmacher 2012; Ma et al. 2012; Borchert et al. 2014; Eisenschmidt et al. 2014; Ochsenein et al. 2015; Eisenschmidt et al. 2016; Heisel et al. 2017; Bötschi et al. 2019). One strategy for such crystal analysis is to detect crystal features such as edges and corners in order to parametrize a geometric crystal model that may be an H- (Borchert and Sundmacher 2012; Borchert et al. 2014; Eisenschmidt et al. 2014; Eisenschmidt et al. 2016) or similar to a V-representation (Ma et al. 2012). However, the challenge of all 2D methods is that they are mostly able describe ideal crystal shapes (Nagy et al. 2013). They are fundamentally not able to capture the shape of 3D particles

when asymmetrical or concave shapes occur. Such cases often occur when damaged or agglomerated crystals are present.

Researchers, therefore, attempt to increase the information content of their measurements. Kempkes et al. (2008) and Agimelen et al. (2018) have combined focused beam reflectance measurements (FBRM) with 2D image analysis. However, due to the non-uniqueness of FBRM measurements it is hard to draw definitive conclusions from them (Kail et al. 2007) and such methods do not yield much additional information compared to traditional 2D image analysis methods (Puel et al. 2003). Another method is stereoscopy. Therein, two stereoscopic images are obtained of crystals at the same time. It was first introduced to crystallization by Schorsch et al. (2014) as on-line technique. Recently, also an in-line technique was proposed (Huo et al. 2020). Although these methods may improve shape analysis, they are still not able to overcome the inherent limitations that come with the restriction to two dimensions that are discussed by Nagy et al. (2013). Even with stereoscopic imaging it is challenging to parametrize the shape of flattened crystals (Jaeggi et al. 2021).

To overcome such limitations Kovačević et al. (2014) and Kovačević et al. (2016) developed image analysis tools to extract crystal shape information from 3D micro-computed tomography ( $\mu$ CT) data. A summary of this work is provided in chapter 4.

## Chapter 3

### Problem definition

Crystallization is dominated by dynamic interaction of the crystallization phenomena nucleation, crystal growth, agglomeration, and the damaging phenomena breakage, attrition and abrasion. Each of these phenomena are extensively studied individually. However, their dynamic interactions are understood to a lesser extent. Exploring the effect of crystal shape is key to improved understanding of dynamic interaction during crystallization.

Above, it is described how faceted crystals can have different shapes. This work deals with how non-ideal crystal shapes can influence crystallization. Non-idealities can be described from two perspectives. (A) Crystals can be damaged through breakage, attrition or abrasion. Such crystals will then have features that cannot be described with the material specific crystal faces. (B) From another perspective, faceted crystals can also not fit the idealized shape that would be expected for them. Such non-idealities may be caused by agglomeration and are studied by Kovačević (2018). In that work, also faceted, not agglomerated but non-symmetric potash alum crystals were observed. Even though these non-idealities were not discussed in detail they were interesting, because only [111] faces occurred. These faces all grow at equal rates and should hence lead to symmetric, octahedral crystals.

From these considerations, two main working hypotheses for the present work are derived:

**Application of 3D crystal shape analysis will improve the understanding of crystal growth and its interaction with damage events.** State of the art shape analysis methods are based on 2D images. Even advanced methods based on stereoscopic 2D imaging struggle to detect rather simple crystal shapes such as flattened crystals (Jaeggi et al. 2021). In contrast,  $\mu$ CT can be used to obtain 3D images that contain full shape information of crystals. Therefore, methods based on 3D image analysis promise enhanced shape analysis and will provide an increased understanding of crystallization phenomena. Such 3D image analysis methods have been developed in previous work, but have not been applied to larger populations yet. This will allow in-depth analysis of the growth of crystal populations and the influence of damaged seed material.

**Damaged crystals do not grow according to established growth laws.** Lower dimensional analysis methods must rely on simple shape models for crystal analysis. Most crystallization models assume perfectly faceted crystals. However, in reality, crystallization slurries are agitated to suspend crystals and to equilibrate temperature and concentration gradients. This imposes mechanical stress on crystals which yields damaged crystals. Damaged crystals are often asymmetrical and have features that cannot be described by classical shape models. Non-ideal shaped crystals make imaging and hence analysis of damaged crystals very challenging, especially if data is limited to one or two dimensions. In previous work (Reinhold et al. 2015), 3D shape modelling has proven itself as powerful tool for the analysis of the effect of abrasion on crystal shape. Such methods are also highly promising to study the effect of non-ideal crystal shape on growth. This will help to understand the dynamic interaction between damaging phenomena and crystal growth.



## Chapter 4

### Methodology

#### 4.1 Crystal shape and size analysis

It is discussed above that state of the art methods based on 2D imaging are only able to analyze crystal shape to a limited extent. In consequence, 3D imaging has emerged as tool for crystal shape analysis. Because 3D imaging for crystallization is a rather new field, the present work comprised considerable development of 3D imaging and modelling methods. This section provides a short summary of the developed methods. Details are found in chapter 5.

##### 4.1.1 Method for obtaining population data from 3D images

3D image acquisition was achieved by  $\mu$ CT. The first hurdle to overcome was to increase the number of crystals that could be imaged by  $\mu$ CT. Kovačević (2018) was able to image about 10 crystals per  $\mu$ CT scan. In context of the work of Schiele et al. (2021a) this limit was increased to almost 800 crystals per  $\mu$ CT scan. This enabled the analysis of populations and their transient behavior instead of only the appearance of single crystals. Considering crystal mass in the binarization step enabled the extraction of accurate crystal volume distributions for the analysis of crystal populations. For more detailed crystal shape analysis the methods of Kovačević (2018) were used and are explained in detail in section 4.2. Further analysis of the shape models was enabled by the definition of two new shape factors that describe the symmetry of faceted crystals and the proportion of non-ideal surface.

##### 4.1.2 Method for tracking the growth of individual crystals

Another goal of this work was to analyze the transient behavior of single crystals (Schiele et al. 2021b). For this, an imaging method was developed that prevents movement of crystals during experiments and provides reference points for image analysis. Crystals were glued to 3D-printed racks. The racks contained geometric features that could be recognized by appropriate image analysis. From the raw  $\mu$ CT images two images were generated. The first contained only the rack and was used to determine the orientation and location of the crystals in each measurement relative to the last measurement. The second image contained the crystals. This image was cut such that it yielded one image for each individual crystal. Images of the crystals at different states of their growth were superposed using the information from the rack images and an optimization procedure based on crystal symmetry. Surface displacement was calculated using a newly developed algorithm. The resulting data yielded growth rates for modelling. Growth rates were described using spherical harmonics functions.

##### 4.1.3 High dimensional Growth modelling

Growth models were based on H-representations as described in section 4.2. The main contribution of this work in this regard was that the orientation of modeled face normals was not motivated by crystal form, but were sampled in such high accuracy (1200 faces) that they were able to describe non-faceted convex shapes with sufficient accuracy. This enabled the simulation of non-faceted shapes and showed convergence into faceted shapes that were expected from measured rates and literature data. The model describes the evolution of size and non-faceted shape of abraded crystals.

## 4.2 Paper I: Morphological Modelling and Simulation of Crystallization Processes (Schiele et al. 2020a)

The methods and results of the present thesis built upon the methods developed by Reinhold (2015) and Kovačević (2018) in context of the DFG priority program SPP 1679.

### Summary

This section reviews their work and thereby explains how convex geometry can be used to describe crystal shapes in 3D both experimentally and for modelling. This lays the theoretical foundation for the results section in chapter 5.

In section 2 of the review, the mathematical concepts of H-representations and V-representations are explained in context of convex crystal shape description. This section is most relevant for the present work as it summarizes the crystal shape analysis methods applied by Schiele et al. (2021a; 2021b). The work of Reinhold et al. (2015) is summarized and it is thereby explained how rounded (i.e. non-ideally shaped) crystals can be described using Minkowski addition based on 2D images. Most importantly, it is explained how single faceted shape models can be parametrized based on 3D images (Kovačević et al. 2014) and how the concept is extended to crystal agglomerates (Kovačević et al. 2016; Kovačević et al. 2017).

Section 3 reviews the work of Heisel et al. (2017) who classified images into the categories *single crystals*, *agglomerates* and *air bubbles*. This work emphasizes that shape characterization based on 2D imaging is possible but leads to certain limitations. Such limitation motivates the application of 3D imaging techniques.

Section 4 summarizes advances in crystallization modelling (Reinhold and Briesen 2015; Kovačević and Briesen 2019). The concept of the 26-dimensional growth model of Reinhold and Briesen (2015) is the basis of the 1200-dimensional growth model proposed by Schiele et al. (2021b). However, there are conceptual differences discussed in sections 5 and 6 of this thesis.

Section 5 of the review describes minor contributions to the DFG project in context of this thesis. A state of the art crystallization population balance model (Qamar et al. 2007) was implemented for the process simulation platform Dyssol (Skorych et al. 2017), used for integrated process simulations and compared to results from the literature (Kulikov et al. 2005). Section 6 summarizes the review.

This article was not peer-reviewed.

### Author contributions

S. Schiele summarized the work of Reinhold (2015) and Kovačević (2018) and implemented the MSMPR crystallizer model (section 5.1). T. Kovačević implemented the hydrocyclone model (section 5.2). S. Schiele conducted the presented simulations in Dyssol (sections 5.3.). The conclusion was written by S. Schiele. H. Briesen supervised all work. The article was corrected and proofread by H. Briesen and T. Kovačević.

### Copyright

The following section is reprinted by permission from Springer Nature Customer Service Centre GmbH: Springer Nature, "Morphological Modelling and Simulation of Crystallization Processes" by Simon Schiele, Tijana Kovačević, and Heiko Briesen in "Dynamic Flowsheet Simulation of Solids Processes" Stefan Heinrich (ed.), (Heinrich 2020, pp. 435–473; Schiele et al. 2020a), Copyright (2020).

# Chapter 13

## Morphological Modelling and Simulation of Crystallization Processes



Simon Schiele, Tijana Kovačević, and Heiko Briesen

**Abstract** The shape of crystals is an important property that has a great impact on their physical behavior. Examples are flowability, dissolution, and growth kinetics. Still, crystals are often described by a single size parameter. One reason is, that today shape information is still hard to measure. Additionally, only few modeling techniques exist that are able to describe the shape of crystals. In this chapter, these issues are addressed by accurately describing crystals with mathematical models, making the full morphological structure of crystals and their agglomerates accessible by stereoscopic and three-dimensional (3D) imaging techniques and using these methods to model crystallization while considering the complex shape of the crystals. In addition, artificial neural networks (ANN) are used to classify whether projections of crystals show single crystals or agglomerates. As a final step, a case study of a model of a mixed suspension mixed product removal (MSMPR) crystallizer and a hydrocyclone are integrated into the software platform Dyssol and used to dynamically simulate a crystallization process with recycling stream.

### 1 Introduction

Crystallization is an important process step in many pharmaceutical, chemical and food processes. It is used to purify and formulate solid products. After crystallization the products are initially suspended in the crystallization mother liquor. Subsequent process steps then deal with the separation of the valuable solids from the rest of the suspension. Such processes are typically centrifugation, filtration, and/or drying. All of the mentioned downstream processes and crystallization itself are highly dependent on the morphology of the particles. The morphology also affects physical properties such as dissolution rates that are particularly interesting for pharmaceutical substances.

---

S. Schiele · T. Kovačević · H. Briesen (✉)  
Chair for Process Systems Engineering, Technische Universität München, 85350 Freising,  
Munich, Germany  
e-mail: [heiko.briesen@tum.de](mailto:heiko.briesen@tum.de)

Commonly, crystals are still described with only few size parameters (such as a diameter or other characteristic lengths). Such descriptions neglect the complex shape that crystals may express. It is not uncommon that crystals have e.g. needle-like shapes or form even more complex structures through agglomeration that are impossible to describe with only one or even a few size parameters.

Today, morphology of crystals is gaining increasing attention not only as a quality criterion, but also as process parameter. Therefore, it is of great interest to describe the morphology of crystals correctly in order to be able to model crystallization with correct consideration of crystal morphology.

The aim of this article is to summarize the efforts that was made in context of a collaborative research project (DFG SPP 1679) towards correct description of crystals and crystallization modeling [1–9]. Such models could then be used in future to optimize and control crystallization processes with respect to downstream process performance and product quality.

## 2 Mathematical Description of Crystals

This section summarizes the basic mathematical crystal representation used in Reinhold et al. [9] and Kovačević et al. [1, 2, 4], which all used potash alum as an exemplary substance. The crystal structure of potash alum is shown in Fig. 1 along with the corresponding miller indices of their faces.

A common way to describe the form of faceted crystals is by Miller indices of their specific faces. This description however, brings two major drawbacks for morphological modeling. First of all, the Miller indices describe each face of a crystal independently and they do not contain any size information. The second drawback

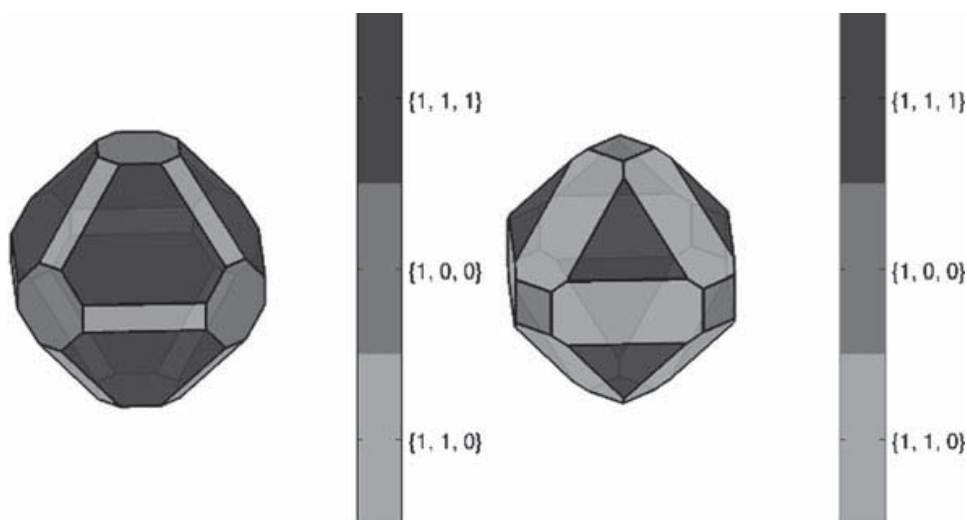


**Fig. 1** Crystalline structure of potash alum crystals according to Ma et al. [10]. The crystals have different morphologies depending on which faces are most expressed. (Reprinted with permission from [8], Copyright (2015) Elsevier)

is that only ideal crystals can be described. More complex crystal shapes that may result from abrasion or agglomeration cannot be described. Therefore, alternative descriptions are explained here.

In mathematical terms, faceted convex shapes consisting of points  $\mathbf{x}$  in space can be described by  $\mathcal{H}$ -representations [11]:

$$C(\mathbf{h}) = \{\mathbf{x} | \mathbf{A}\mathbf{x} \leq \mathbf{h}\} \quad (1)$$

where  $\mathbf{A}$  is a matrix with normal vectors of facets in space  $\mathbf{a}_i$ , and  $\mathbf{h}$  is a vector with the length of these vectors. The  $\mathcal{H}$ -representation describes all points that are within the facets defined by  $\mathbf{A}$  and  $\mathbf{h}$ . For crystals, rows of  $\mathbf{A}$  can be interpreted as normal vectors of the faces of such a crystal.  $\mathbf{A}$  is therefore specific for each crystal morphology. The vector  $\mathbf{h}$  then describes the exact shape and size of an ideal crystal of form  $\mathbf{A}$ . Herein, the dimension of  $\mathbf{x}$  is either two or three dimensional (2D/3D).

For crystals it is common that symmetry conditions apply. To reduce the dimension of  $\mathbf{h}$ , one can, therefore, introduce a crystal model-specific group mapping matrix  $\mathbf{M}_{\mathbf{h}_C \rightarrow \mathbf{h}}$  [11]

$$\mathbf{h} = \mathbf{M}_{\mathbf{h}_C \rightarrow \mathbf{h}} \cdot \mathbf{h}_C \quad (2)$$

This operation can also be formulated in a reverse way with the pseudo inverse matrix  $\mathbf{M}_{\mathbf{h}_C \rightarrow \mathbf{h}}^+$  [11]

$$\mathbf{h}_C = \mathbf{M}_{\mathbf{h}_C \rightarrow \mathbf{h}}^+ \cdot \mathbf{h} \quad (3)$$

These constrained crystal models are called constrained  $\mathcal{H}_C$ -representations [11–13].

Because  $\mathcal{H}$ -representations only allow the description of ideal single crystals, the representation is extended so that also more complex shapes can be described. Abraded crystals, for instance, may not have sharp edges that would be described by an  $\mathcal{H}$ -representation, but may appear with round edges and corners. Agglomerates on the other hand may be concave and can therefore also not be represented by simple  $\mathcal{H}$ -representations.

For the description of rounded particles, an ideal kernel crystal (index  $k$ ) was combined with a sphere. The combination of sets in general can be performed by the so-called Minkowski addition [14]. The combination of  $i$  sets  $S_{1\dots i}$  can be written as

$$S = \sum S_i = \left\{ \sum \mathbf{x}_i | \mathbf{x}_i \in S_i \forall i \right\}. \quad (4)$$

The addition of an ideal kernel crystal  $C(\mathbf{h}_k)$  and a sphere  $B$  that has the radius  $\lambda_r$  [11] is accordingly written as

$$C(\mathbf{h}_k, \lambda_r) = C(\mathbf{h}_k) + \lambda_r B. \quad (5)$$

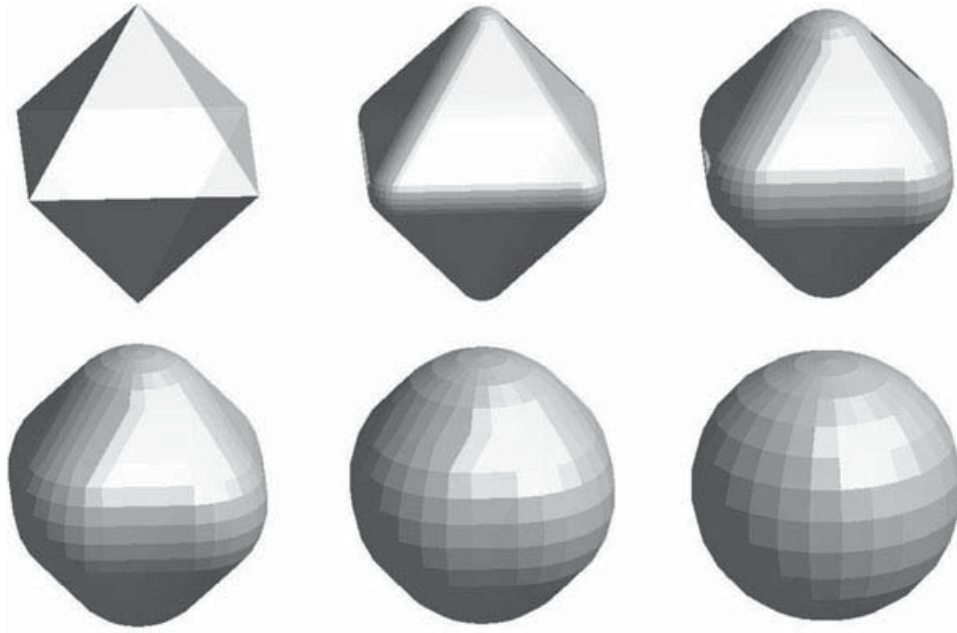


**Fig. 2** 3D models with increasing roundness obtained by the addition of octahedral potash alum kernel crystals with spheres. (Reprinted with permission from [9], Copyright (2015) Elsevier)

A graphical representation of Eq. (5) for six different radii and an octahedral potash alum kernel crystal can be seen in Fig. 2.

The representation as a 3D body allows the calculation of the volume  $\mu^{\text{vol}}$ , surface area  $\mu^{\text{sur}}$ , and mean width  $\mu^{\text{mw}}$  from the corresponding measures  $\mu_k^{\text{vol}}$ ,  $\mu_k^{\text{sur}}$ , and  $\mu_k^{\text{mw}}$  of the kernel crystal and the radius of the sphere  $\lambda_r$  [14]:

$$\mu^{\text{vol}} = \mu_k^{\text{vol}} + \mu_k^{\text{sur}} \lambda_r + 2\pi \mu_k^{\text{mw}} \lambda_r^2 + \frac{4}{3} \pi \lambda_r^3 \quad (6)$$

$$\mu^{\text{sur}} = \mu_k^{\text{sur}} + 4\pi \mu_k^{\text{mw}} \lambda_r + 4\pi \lambda_r^2 \quad (7)$$

$$\mu^{\text{mw}} = \mu_k^{\text{mw}} + 2\lambda_r \quad (8)$$

For 2D bodies only  $\mu_k^{\text{sur}}$ , and  $\mu_k^{\text{mw}}$  can be calculated.

Agglomerates can be described by an  $\mathcal{H}$ -representation for each primary crystal. Additionally, information on orientation and location of the center of mass of the primary crystals is needed. Details are described in Sect. 2.3.

Another way to describe crystals is by a matrix  $\mathbf{V}$  that contains vectors that point to the vertices of a crystal.

$$\mathbf{V} = [\mathbf{v}_1, \dots, \mathbf{v}_{n_v}]^T \quad (9)$$

Kovačević et al. call this a V-representation [1].

## 2.1 Description of Crystal Projections and Roundness Measurement

A fundamental question in crystal or particle representation is, how to deal with roundness instead of sharp edges and corners. A framework in this respect was introduced by Reinhold et al. [9]. The roundness of a crystal can be used as a parameter that describes how much attrition occurs in a process. To achieve this, first 3D crystals were modeled and then projections of these models were generated. They were used to validate the experimental procedures that are described in the end of this section. The comparison of the exact roundness obtained from 3D models and the roundness obtained from 2D projections of the model crystals allowed an evaluation of how well the roundness can be measured when only 2D information is available and how non-ideal images affect the roundness measurement. This is particularly interesting because it is currently not possible to obtain 3D images of crystals in real time and on-line analysis of particulate systems is often done by 2D image analysis.

To define the roundness of a particle, several definitions exist in the literature [15–18]. Here, a new descriptor for roundness  $\mu^B$  was defined so that it can be calculated from the geometric properties of the Minkowski addition [9]. A spherical crystal which is by definition perfectly round, can be described by Eq. (5) with  $h_k = 0$  and hence  $\mu^{mw} = 2\lambda_r$  results from Eq. (8). A crystal that has sharp edges and is therefore as little round as possible for a given kernel crystal, is described by Eq. (5) with  $\lambda_r = 0$  and hence  $\mu^{mw} = \mu_k^{mw}$  results from Eq. (8). To reflect this concept of roundness the roundness parameter  $\mu^B$  is written as

$$\mu^B = 1 - \frac{\mu_k^{mw}}{\mu^{mw}} = \frac{2\lambda_r}{\mu_k^{mw} + 2\lambda_r} \quad (10)$$

Note that it can be calculated for a body of any dimension, in this case for 2D and 3D bodies equivalently.

3D crystals with roundness between 0 and 1 and defined mean width were simulated using Eq. (5). A potash alum model with 26 faces was used for the kernel crystal model (see Fig. 3 left-hand side). This gained numerous crystal models with

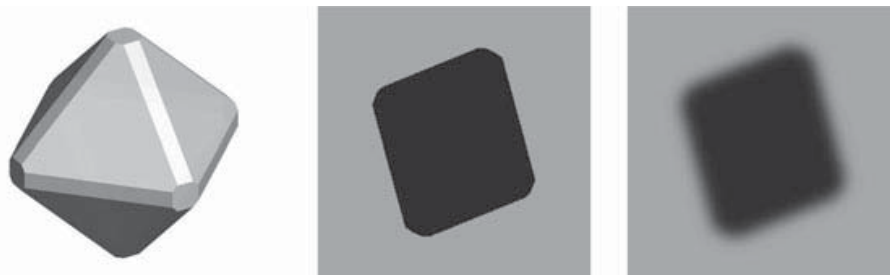


**Fig. 3** Rendered 3D model of a potash alum crystal model with 26 faces (left), a 2D projection of this crystal (middle) and the same 2D projection to which blur was added (right). (Reprinted with permission from [9], Copyright (2015) Elsevier)

known, exact measure of their roundness and mean width (grey line in Fig. 2). From each body, multiple 2D projections  $\Pi_p$  were generated and blur was added to the images, as described in [9] (see Fig. 3 middle and right-hand side). Finally, two additive roundness parameters were calculated for each particle from its 2D projections with the sharp and blurred 2D images (black lines in Fig. 2). The additive roundness estimates the roundness parameter of the real 3D particle from its  $n_{proj}$  projections:

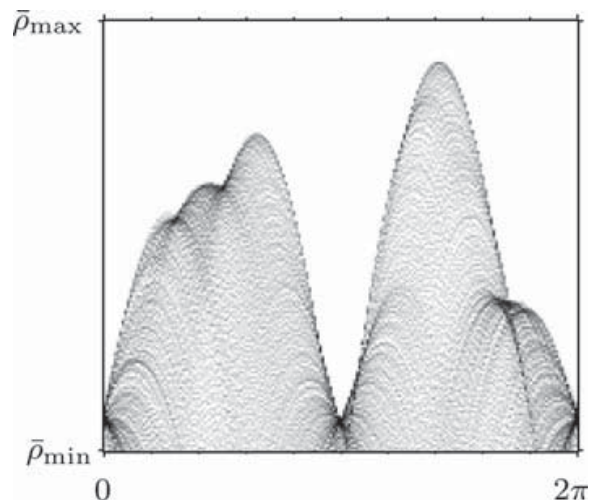
$$\mu^B \approx 1 - \frac{\mu^{mw} - \sum_p \frac{1}{n_{proj}} \lambda_{r, \Pi_p}}{\mu^{mw}} \quad (11)$$

In the following, it is described how  $\mu^{mw}$  and  $\lambda_{r, \Pi_p}$  were obtained from  $n_{proj}$  projections of a particle in order to be able to calculate the roundness  $\mu^B$  according to Eq. (11). The first step was to find a 2D  $\mathcal{H}$ -representation of each individual projection. It was found by Hough transform [19] performed as follows. First, the center of mass of a projection was determined and considered as the center of a Cartesian coordinate system. Lines on the border of a projection can be described by an angle  $\bar{\varphi}$  and distance from the center of mass  $\bar{\rho}$ . The vector  $(\cos \bar{\varphi}, \sin \bar{\varphi})^T$  describes a normal vector of such a line. Then any point on the line  $\mathbf{x}$  is described by the scalar product

$$\bar{\rho} = \left\langle \mathbf{x}, \begin{pmatrix} \cos \bar{\varphi} \\ \sin \bar{\varphi} \end{pmatrix} \right\rangle \quad (12)$$

The pixels on the outline of a projection  $\Pi_p$  were considered as data points.  $\bar{\varphi}$  and  $\bar{\rho}$  were discretized in pieces  $\bar{\varphi}_j$  and  $\bar{\rho}_l$ . Each point  $\mathbf{x}$  could be described by several lines defined by Eq. (12) and a combination of  $\bar{\rho}_l$  and  $\bar{\varphi}_j$ . A bin value was introduced for each combination of  $\bar{\rho}_l$  and  $\bar{\varphi}_j$  that represented how many data points  $\mathbf{x}$  were described by such a line. This yielded a grey scaled image with the coordinates  $0 \leq \varphi_i \leq 2\pi$  and  $\bar{\rho}_{\min} \leq \bar{\rho}_l \leq \bar{\rho}_{\max}$  (see Fig. 4). High bin values (represented as dark points in Fig. 4) indicate coordinates which describe many points of the outline

**Fig. 4** Bin values of a Hough transform. (Reprinted with permission from [9], Copyright (2015) Elsevier)



of a projection. In other words, these lines represent long sections of the outline. The corresponding distance  $\bar{\rho}_l$  and normal vector  $(\cos \bar{\varphi}_j, \sin \bar{\varphi}_j)^T$  were hence potential values for an  $\mathcal{H}$ -representation.

To reduce the number of outlines, only local maximum bin values (index  $m$ ) were considered as detected lines. They were described by the vectors

$$\mathbf{a}_{c,\Pi_p,m} = (\cos \bar{\varphi}_m, \sin \bar{\varphi}_m)^T \quad (13)$$

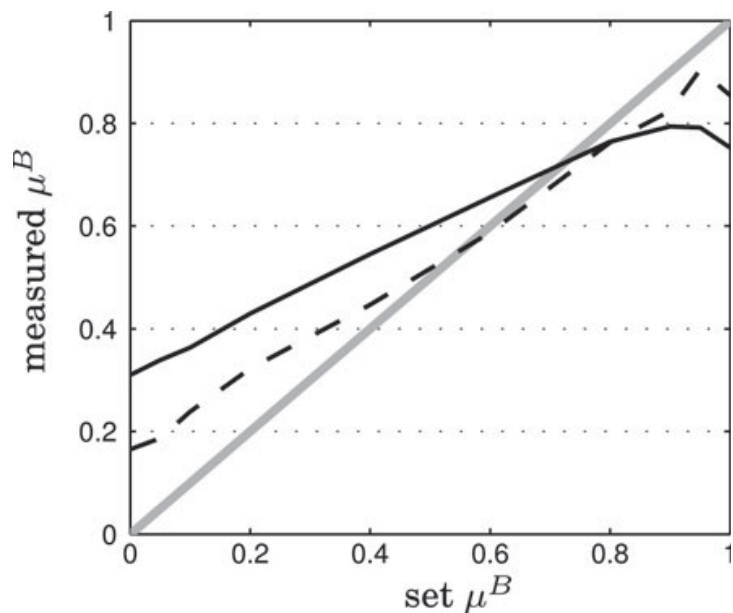
that make up the matrix  $\mathbf{A}$  of a 2D  $\mathcal{H}$ -representation. The face distances  $\mathbf{h}$  were given by all  $\bar{\rho}_m$ . Like this, a 2D  $\mathcal{H}$ -representation of a projection was found.

To describe not only the kernel crystal but also the roundness, a disc with radius  $\lambda_r$  was added to the  $\mathcal{H}$ -representation using the Minkowski addition. The size of this disc was determined by solving a minimization problem: The experimental data contained the outline of a projection. This outline was also described by the Minkowski addition of the previously found  $\mathcal{H}$ -representation and a disk of unknown radius  $\lambda_r$  (Eq. 5). An appropriate disc radius was then found by minimizing the distance between these two lines. A detailed description is given by Reinhold and Briesen [9].

From the Minkowski additions of each projection  $\Pi_p$ , a mean width  $\mu_{\Pi_p}^{\text{mw}}$  was obtained according to Eq. (8) and used to calculate the additive roundness defined in Eq. (11).

It can be seen in Fig. 5, that even for crystals that had perfect edges (set  $\mu^B = 0$ ) a roundness of 0.17 was measured. This was caused by the discretization of the boundary points during image analysis. This error was even more pronounced for blurred images. As it can be seen in Fig. 3 that corners of the projections were not as expressed as in the sharp images. For very round particles, 2D analysis yielded lower roundness than one should expect (c.f. Fig. 5). This was caused by the fact that small line segments fitted well to a hand-full of boundary points, hence faces

**Fig. 5** Simulated roundness (solid gray line) and the roundness obtained based on ideal (dashed black line) and blurred (solid black line) 2D images. (Reprinted with permission from [9], Copyright (2015) Elsevier)



were found and the kernel crystal never fully disappeared. Overall, the roundness of particles can be measured well for roundness values below 0.85.

Going one step further, stereoscopic 2D images of real abraded potash alum crystals were obtained on-line from suspension with the stereoscopic imaging method described by Schorsch et al. and Reinhold et al. [9, 20]. Stereoscopic images were taken of potash alum crystals in a saturated, agitated solution at three points in time (start of the experiment, two hours and five hours after the start). Both the mean width and the additive roundness of the particles were calculated with Eqs. (14) and (11). A high stirring rate (1800 rpm) was used so that excessive abrasion occurred. Because the crystals were suspended in a saturated solution, neither growth nor dissolution was expected. Stereoscopic imaging as performed here yielded two orthogonal projections of a particle. For each of these projections a Minkowski addition was found by appropriate image analysis as described above.

The mean width of the real 3D particle was estimated by the weighted addition of the mean widths of the two obtained stereoscopic projections  $\Pi_p$ .

$$\mu^{mw} \approx \sum_p \frac{1}{n_{proj}} \mu_{\Pi_p}^{mw} \quad (14)$$

Figure 6 shows that at the beginning of the abrasion experiment the crystals were large (mean width between 450 and 850  $\mu\text{m}$ ) and have sharp edges (roundness around 0.3). With increasing experiment time, roundness increased (up to 0.7) and the mean width decreased (250  $\mu\text{m}$ ). Following the theory of Gahn and Mersmann

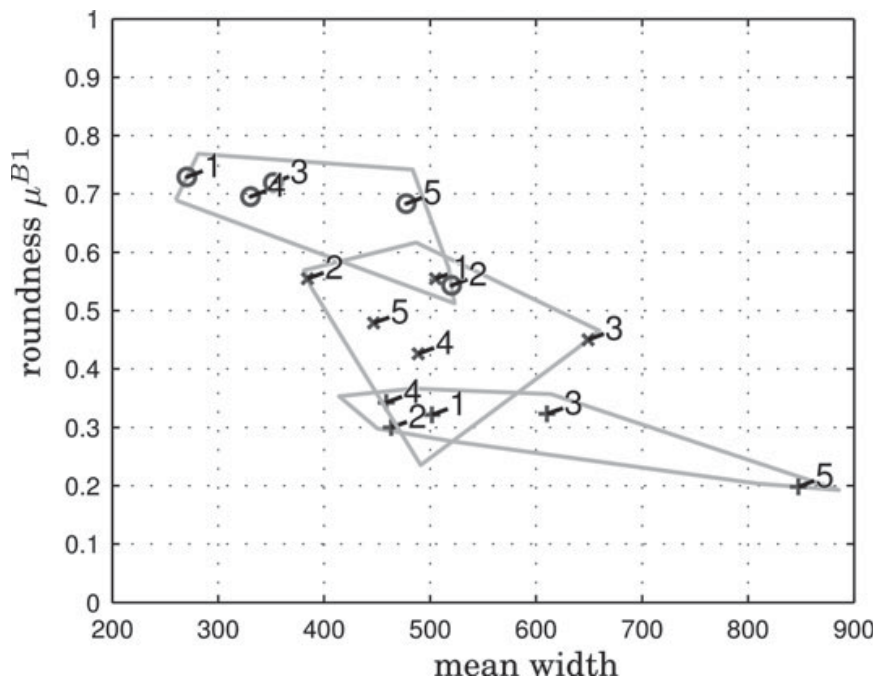


**Fig. 6** Measured roundness of real crystals over their measured mean width at different time of the crystallization experiment. + indicate samples obtained at the start of the experiment, x after two hours and o after 5 h. (Reprinted with permission from [9], Copyright (2015) Elsevier)

[21], abrasion occurs through impact of crystals on the stirrer. This impact causes breakage predominantly at corners and edges of the particles [22, 23]. This explains that roundness increased and the mean width of the particles decreased through intensive agitation.

In conclusion, limitations of the measurement of roundness from 2D projections of particles were revealed and quantified. Further, a new method was demonstrated that is able—under the previously mentioned limitations—to quantify the particle roundness and mean width during crystallization by using stereoscopic imaging in combination with appropriate image analysis.

## 2.2 Shape Identification of 3D Single Crystals

Similar image analysis concepts as described in the previous subsection can be applied to 3D images of crystals. 3D images can be obtained by micro-computed tomography ( $\mu$ CT) as described by Kovačević et al. [1]. This imaging technique allows capturing the full shape information of particles. However, images are much harder to obtain.

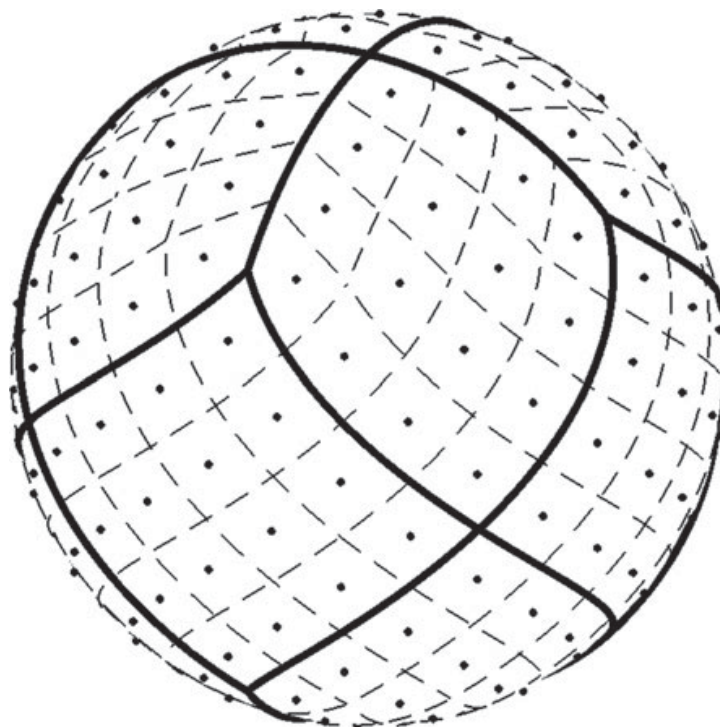
The goal here was to find faces of measured crystals and fit them to a predefined crystal model. Here again, the image analysis involved face identification using Hough transform. Subsequently face normals of the predefined crystal models—given by a crystal specific matrix  $\mathbf{A}$ —were matched to the faces found in a 3D image. The main difference to the problem in Sect. 2.1—except for the higher dimensionality—is that a crystal model was predefined and then fitted to the 3D images. The goal was to find faces that appear in a measured crystal.

In a first step, it was assumed that a 3D image of a crystal is given as a set of regularly distributed surface points. This data set was extracted from  $\mu$ CT measurements. A 3D polar coordinate system was chosen so that it originated from the arithmetic mean of these surface points. In this coordinate system face normal vectors were described by an azimuthal angle  $\theta$  and a polar angle  $\phi$ . Distances from the origin were described by  $\rho$ . Both angles  $\theta$  and  $\phi$  were then discretized using the HEALPix algorithm [24].

Figure 7 visualizes the HEALPix discretization of a unit sphere with 12 principal elements (solid outline), with  $N_{\text{side}}^2 = 16$  subelements of equal area (dashed outline). For calculations in this work  $N_{\text{side}}$  was chosen as 20. Each of these  $12 \cdot N_{\text{side}}^2$  subelements were represented by a potential face normal vector and face distance. The face distance was also discretized. To apply the Hough transform, each grid point that was defined by  $\theta_i$ ,  $\phi_j$  and  $\rho_l$  was assigned a bin value  $b(\theta_i, \phi_j, \rho_l)$  that represented the number of surface points within it. To obtain the directions of the face normals it was sufficient to define one bin value  $\tilde{b}(\theta_i, \phi_j)$  per subelement:

$$\tilde{b}(\theta_i, \phi_j) = \max_{\rho} b(\theta_i, \phi_j, \rho_l) \quad (15)$$

**Fig. 7** HEALPix discretization of a unit sphere [25]. (Reprinted with permission from [1], Copyright (2014) American Chemical Society)



Local maxima of this function represent orientations of face normals. A typical function with its local maxima is shown in Fig. 8. Such local maxima were found by a non-maximum suppression search [19, 26]. This algorithm was slightly adapted to be used for points on a sphere as described by Kovačević et al. [1].

The points of the local maxima led to measured face normals that can be written as

$$\mathbf{n}_F(\theta_i, \phi_j) = [\cos(\theta_i) \sin(\phi_j), \sin(\theta_i) \sin(\phi_j), \cos(\theta_i)] \quad (16)$$

in a Cartesian coordinate system. All the measured face normals were summarized in the matrix  $\mathbf{A}_F$ .

The next challenge was to match the face normals of a crystal model  $\mathbf{A}$  to these measured face normals. This task was subdivided into three individual problems. First, the measured vectors may have had different order in  $\mathbf{A}_F$  than their corresponding model vectors in  $\mathbf{A}$ , and  $\mathbf{A}$  may contain faces that were not measured in a real crystal because faces had disappeared e.g. due to fast growth. Second, the measured matrix  $\mathbf{A}_F$  may contain faces that were not included in the crystal model. This may have happened due to agglomeration or breakage of the real crystals. Third, measured face normal vectors needed to be rotated to point in the directions of the model.

The first problem was solved by defining a mapping matrix  $\mathbf{S}_M$  that permuted the vectors in  $\mathbf{A}$  and excluded normal vectors which had no corresponding face in  $\mathbf{A}_F$ . For the second problem, a filter matrix  $\mathbf{S}_D$  that excluded all faces in  $\mathbf{A}_F$  that had no corresponding face in  $\mathbf{A}$  was defined. For the rotation of the measured into the model vectors a rotation matrix  $\mathbf{R}$  was defined. With these definitions, a real crystal was approximated by a crystal model with

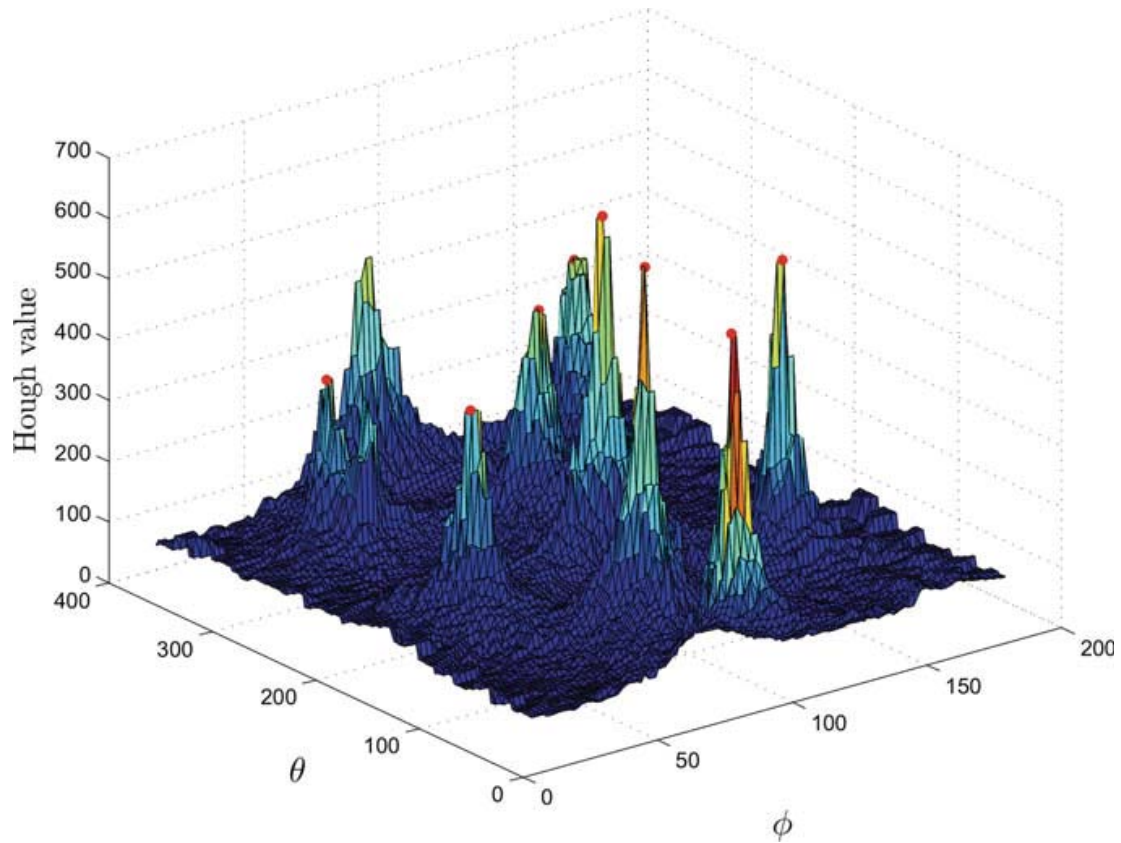


**Fig. 8** Bin values of the Hough transform. Red dots mark local maxima. (Reprinted with permission from [1], Copyright (2014) American Chemical Society)

$$S_D \cdot A_F \approx (S_M \cdot A) \cdot R^T \quad (17)$$

The problem to rotate a set of vectors  $r_i$  into the vectors  $b_i$  was formulated by Wahba [27] and solved by Markley [28] by minimizing the least-square cost function

$$L(R) = \frac{1}{2} \sum_i \omega_i \|b_i - Rr_i\|^2 \quad (18)$$

We chose to use equal weights  $\omega_i$  that satisfy  $\sum_i \omega_i = 1$ . The rotation matrix  $R$  was calculated from

$$R = UMW^T \quad (19)$$

Therein,  $U$  and  $W$  resulted from the singular value decomposition of the matrix  $B$

$$B = \sum_i b_i r_i^T \quad (20)$$

into

$$\mathbf{B} = \mathbf{U}\mathbf{D}\mathbf{W}^T \quad (21)$$

and

$$\mathbf{M} = \text{diag}(1, 1, \det(\mathbf{U}), \det(\mathbf{W})) \quad (22)$$

Provided  $\mathbf{S}_M$  and  $\mathbf{S}_D$  were known, one could solve Wahba's problem given in Eq. (18). However,  $\mathbf{S}_M$  and  $\mathbf{S}_D$  were unknown and one could have found a solution to the problem by testing all possible combinations of  $\mathbf{S}_M$ ,  $\mathbf{S}_D$  and  $\mathbf{R}$ :

$$L(\mathbf{R}, \mathbf{S}_D, \mathbf{S}_M) = \frac{1}{2} \sum_i \omega_i \left\| (\mathbf{S}_D \cdot \mathbf{A}_F)_i - [(\mathbf{S}_M \cdot \mathbf{A})\mathbf{R}^T]_i \right\| \quad (23)$$

This had involved the optimization over a huge parameter space, which is computationally inefficient. Kovačević et al. [1] developed an algorithm to efficiently solve this problem and described it in detail. Within the scope of this contribution it is sufficient to understand that a numerically efficient solution exists that yields  $\mathbf{R}$ ,  $\mathbf{S}_D$  and  $\mathbf{S}_M$ .

To obtain a description of a measured crystal by a crystal model so far a rotation matrix, a mapping, and a filtering matrix has been found. The face distances remained to be determined. This could have been done quite easily by finding the  $\rho_l$  that maximize Eq. (15) for faces that have been measured. However, for faces that have grown out of the crystal, and are hence not found in the measurement data, this does not work. For these cases, the measured data was cut into planar slices that are orthogonal on a face normal vector, and are therefore defined by  $\rho \mathbf{n}(\theta_i, \phi_j)$ . The triangles in Fig. 9 show, that slices inside the measured data contain an outline of the crystal at distance  $\rho$  from the center. The ratio between the number of pixels on the outline and the area of the convex hull of the outline was then maximized by finding an appropriate face distance  $\rho$ . This principle is illustrated in Fig. 9. Therein the arrow indicates a normal vector of a face of a potash alum crystal that is not expressed in the measured data. The triangles represent the outline for a face distance that is too small, and squares indicate a slice where the mentioned ratio reaches its maximum.

In the last two steps towards a successful fit, it needed to be assured that all identified faces lied within the crystal model and fulfilled the symmetry conditions defined by the crystal model. The first issue is illustrated in Fig. 10: If a face distance was identified to be too long, a face lied outside of the model.

To assure that all identified crystal faces lied within the fitted model, invalid entries in the vector  $\mathbf{h}$  were identified according to Reinhold and Briesen [11], and Borchert and Sundmacher [12] and then modified according to

$$h_i = \max_{1 \leq i \leq n_H, 1 \leq j \leq n_V} \langle \mathbf{a}_i, \mathbf{v}_j \rangle \quad (24)$$

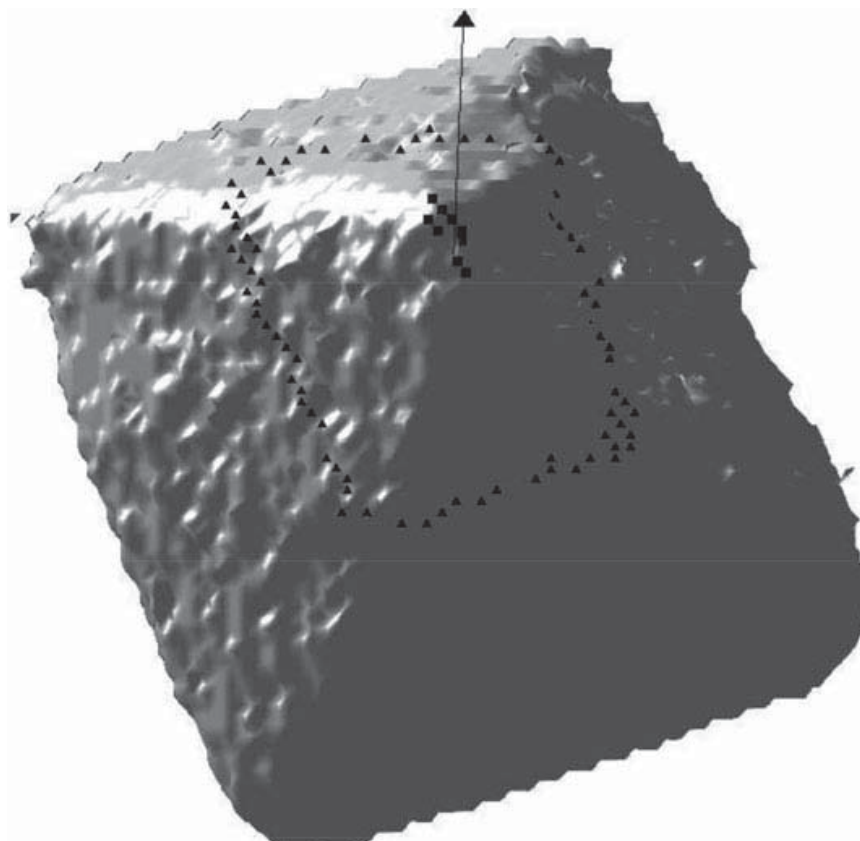


**Fig. 9** Measured hull of a potash alum crystal with a model normal vector of a face that is not expressed in the measurement (arrow). Triangles indicate points in a slice that is orthogonal to the vector and that has a distance that is too small to appropriately describe the face distance. Squares indicate the length of the normal vector that describes a disappearing face of the crystal. (Reprinted with permission from [1], Copyright (2014) American Chemical Society)

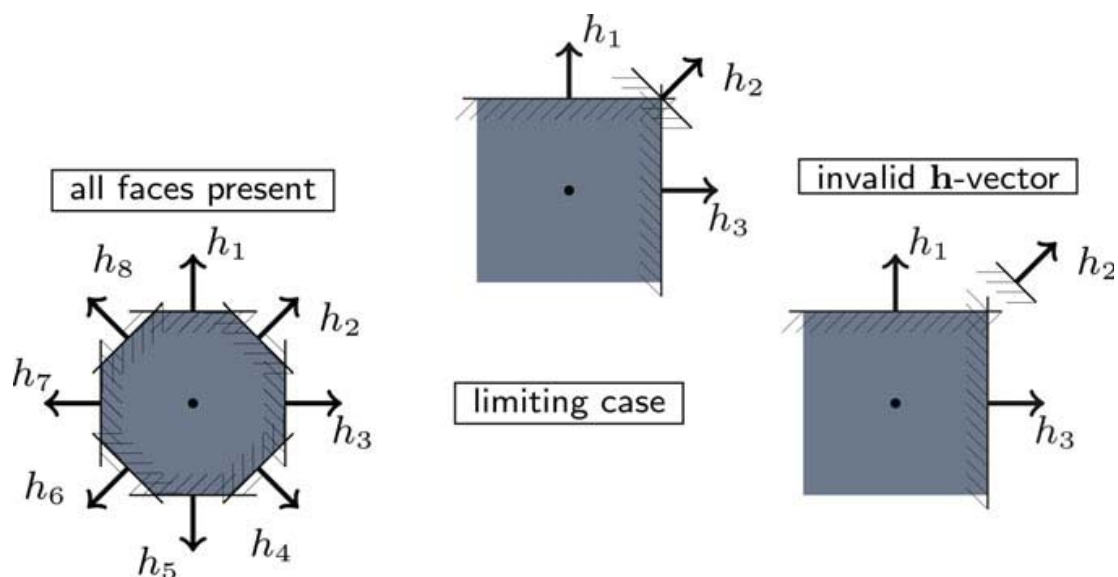


**Fig. 10** Illustration of the problem of faces lying outside of a crystal model as discussed by Reinhold and Briesen [11]. An invalid face vector is shown on the right-hand side of the figure. (Reprinted with permission from [1], Copyright (2014) American Chemical Society)

where the vector  $v_j$  represents vertices in the crystal's V-representation as defined in Eq. (9).

Finally, symmetry conditions were applied to ensure that all faces belonging to the same facet group had the same distance to the crystal center. The procedure is described by Kovačević et al. [1].

As measures how well investigated crystals were fitted, the mean quadratic deviation,  $d_{\text{quad}}$ , a volume ratio,  $r_{\text{vol}}$ , and the volume deviation,  $d_{\text{vol}}$  were introduced.  $d_{\text{quad}}$  is a measure to determine how much measured points differ from their fit. Therein long distances between model and measurement are weighted stronger. The volume ratio is a measure how well the volume is conserved and the volume deviation is a scaled measure of how much the fitted shape mismatches the measured shape. Details on how these measures were calculated can be retrieved from Kovačević et al. [1].

The method described in this section enables to fit crystal models to 3D  $\mu$ CT images obtained from regular potash alum crystals. Results of the fits are shown in Fig. 11. Irregular particles that resulted from e.g. breakage or agglomeration were identified by high volume deviations and high quadratic deviations.

In conclusion, the methods that were developed enable face identification in 3D images. It was described how these faces can be matched to predefined particle models. The method was applied to the model substance potash alum and it was shown that single particles can be described with only few parameters by appropriate crystal models.

### 2.3 Shape Identification of Crystal Agglomerates

Even more challenging than identifying single crystals is the identification of several primary crystals constituting a crystal agglomerate. Kovačević et al. [2] presents an approach how concepts of identification of single crystals can be transferred to the identification of agglomerates.

Generally, one needs to find all primary particles in an agglomerate and then use the methods described by Kovačević et al. [1] and in the previous section to model their structure with individual  $\mathcal{H}$ -representations. Thus, each agglomerate would be described by a hand full of  $\mathcal{H}$ -representations of its primary particles.

To separate agglomerates into their primary particles an algorithm based on the seeded watershed segmentation and region recombination was developed (see Fig. 12). The steps defined in Fig. 12 are illustrated with an example agglomerate in Fig. 13. The first step of the agglomerate segmentation algorithm is to find concavity points that are an indicator for contact points of primary particles. The 2D approach of Fernandez et al. [29] and Indhumathi et al. [30] was used and transferred to the presented 3D problem: A cubic mask was centered at each surface point of the measurement and a concavity value  $c_p$  was calculated. It was defined as the quotient of the number of voxels that contain material  $N_{\text{foreground mask}}$  and the number of voxels inside the mask  $N_{\text{mask}}$ .

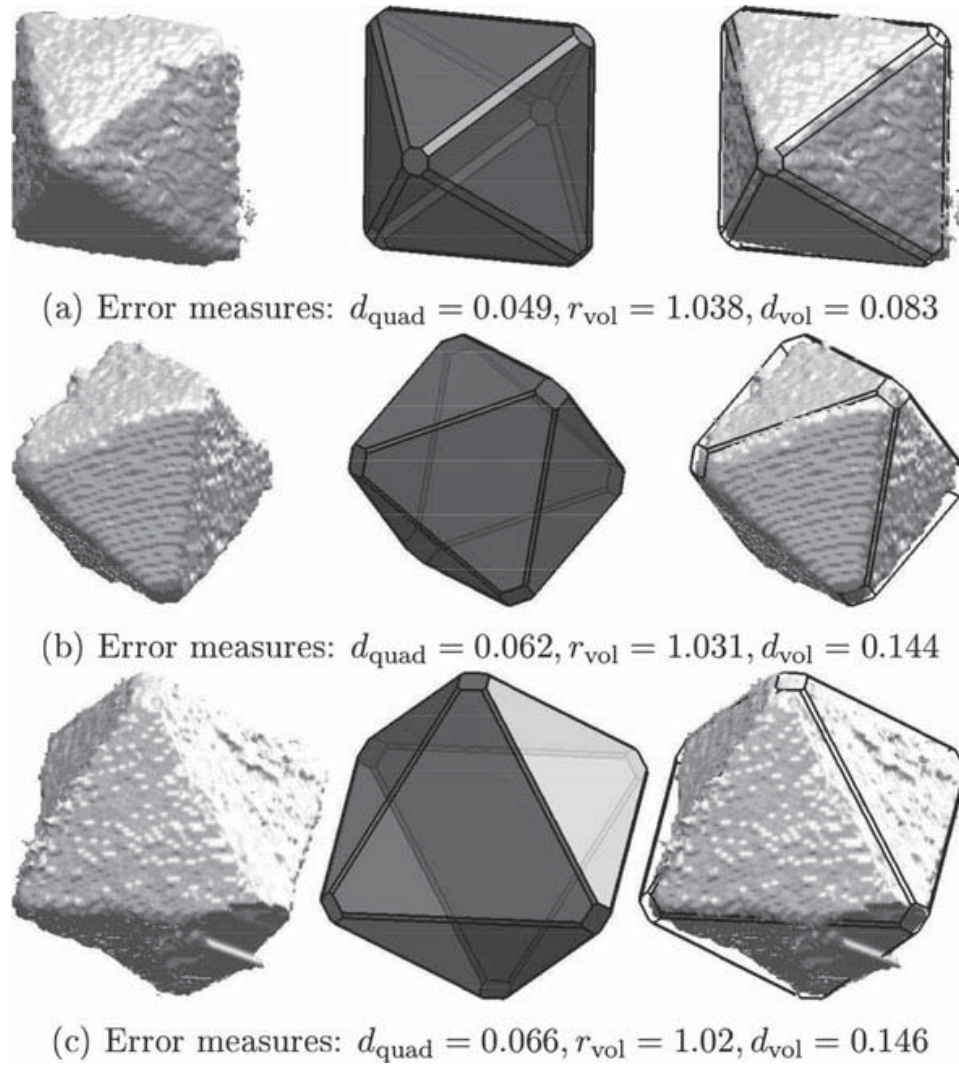


**Fig. 11** Successful fits of regular potash alum crystals. (Reprinted with permission from [1], Copyright (2014) American Chemical Society)

In measurements with infinite resolution a concave region is identified by a concavity value higher than 0.5, meaning that more than half of the mask is filled. However, this is not a reasonable threshold for real measurement data. Due to the discretization of an image into voxels, surfaces appear rough even if they may be flat in reality. The concavity value also depends on the orientation and size of the mask. Therefore, the mask edge length was set to  $2a + 1$  where  $a = \sqrt[3]{0.0013N_{\text{voxels}}}$ .  $N_{\text{voxels}}$  is the total number of voxels inside a measured agglomerate. The concavity threshold was then calculated using

$$c_t = 1.2 \frac{(2a + 1)^2(a + 1)}{(2a + 1)} \quad (25)$$

The factor 1.2 was used to compensate for boundary roughness, different orientations of the masks, and measurement inaccuracies. Finally, concavity points were

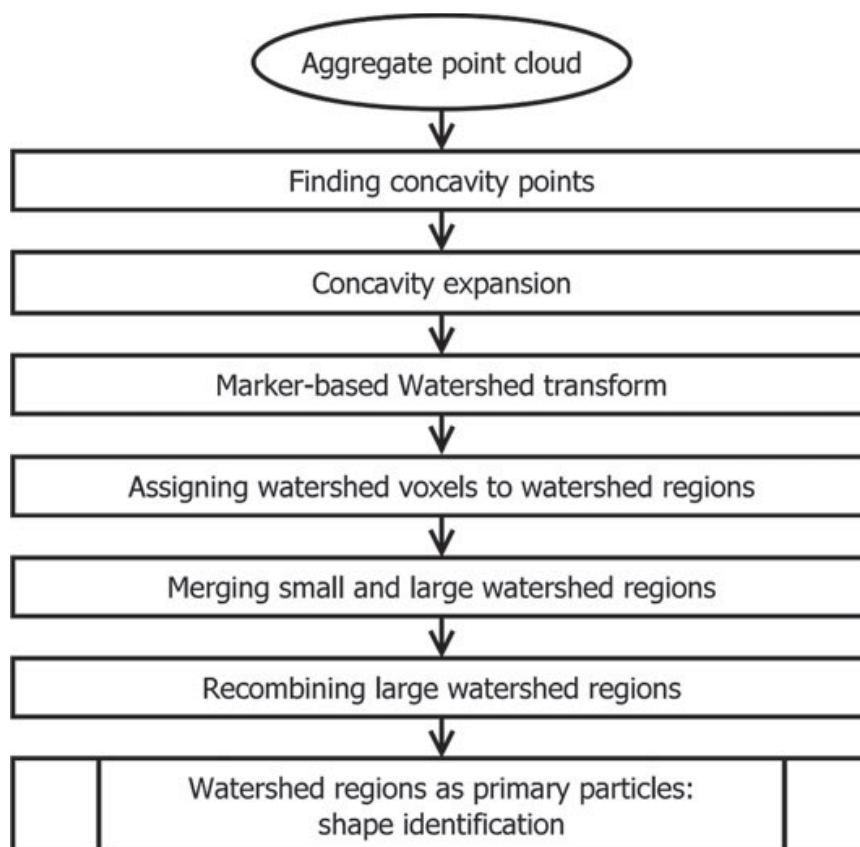


**Fig. 12** Algorithm to separate agglomerates into their primary particles. (Reprinted with permission from [2], Copyright (2016) American Chemical Society)

identified by the local maxima of all points on the surface that satisfied  $c_p > c_t$ . This was done by a non-maximum suppression peak search in cube shaped windows with an edge length of  $a + 1$  [19, 26]. These concavity points were then expanded to prevent under-segmentation of the following distance transform-based watershed segmentation. The expansion was done in a way that a hole was drilled into the measured structure at every concavity point perpendicular to the surface (c.f. Fig. 13b). For details on the concavity expansion refer to Kovačević et al. [2]. Finally, watershed transform was applied to segment the agglomerate into primary particles. A description of the watershed transform algorithm can be found in the work of Vincent and Soille [31] and Gonzales et al. [32].

Although the concavity point expansion prevented under-segmentation by the watershed algorithm (under-segmentation shown in Fig. 13a), it often led to over-segmentation (Fig. 13c). Therefore, segments that belonged to the same primary particle needed to be identified and subsequently merged. To achieve this, first neighboring regions were identified. Then small regions that each made up less than 3% of the total number of voxels were merged with an adjacent region so that the concavity of the resulting larger region was minimized (Fig. 13e). The concavity of the merged region was calculated from Eq. (26):

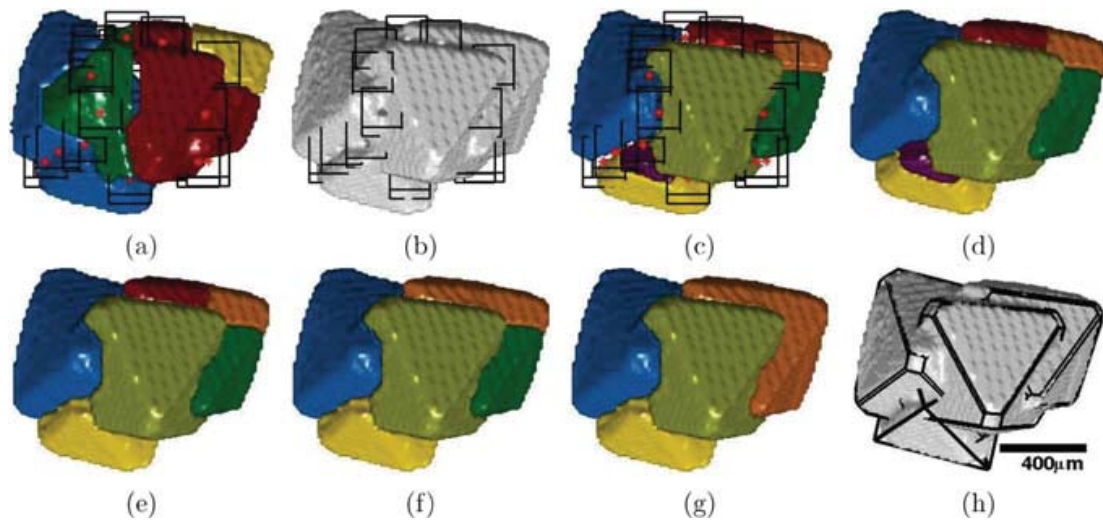


**Fig. 13** Segmentation of an exemplary potash alum agglomerate with the algorithm summarized in Fig. 12. The images **a** and **c** show the difference of the result of the watershed transform when concavities are (c) or are not (a) expanded. Concavities are marked as red stars with their corresponding masks as black cubes. **b** shows the agglomerate with expanded concavity points. Image **c** shows the result of the watershed transform. In **d** the boundary voxels that have been identified by the watershed transform are merged into adjacent regions. In **e** the small, purple region in **d** is merged with the yellow region, **f**, **g** show the first and second iteration of the large region merging, so that (**g**) is the result of the segmentation algorithm. **h** shows the rendered measured crystal together with a successful fit obtained with the methods described in Sect. 2.2. (Reprinted with permission from [2], Copyright (2016) American Chemical Society)

$$c_r = \left| 1 - \frac{N_i + N_j}{V} \right| \quad (26)$$

$N_i$  and  $N_j$  are the number of voxels of the two regions to be merged and  $V$  is the volume of their convex hull. For details on the exact procedure refer to Kovačević et al. [2].

After the small regions were merged, it was checked whether merging of large regions also led to a smaller average concavity of a merged region. Examples are the combination of the red and orange regions in Fig. 13e and the green and orange regions in Fig. 13f. While this was done, concavity points were considered. If the mask of a concavity point included exactly two regions, the merging of these two regions was forbidden. Another case where merging was forbidden is when merging would have been allowed according to the first condition, but the concavity value of a concavity point was increased through merging over some threshold. This could have been the case if a concavity point contained e.g. three regions. For details on this procedure again refer to Kovačević et al. [2].

Once an agglomerate was divided into its primary particles, the methods described in Sect. 2.2 could be adopted and applied to find  $\mathcal{H}$ -representations for each primary particle, as shown in Fig. 14h.

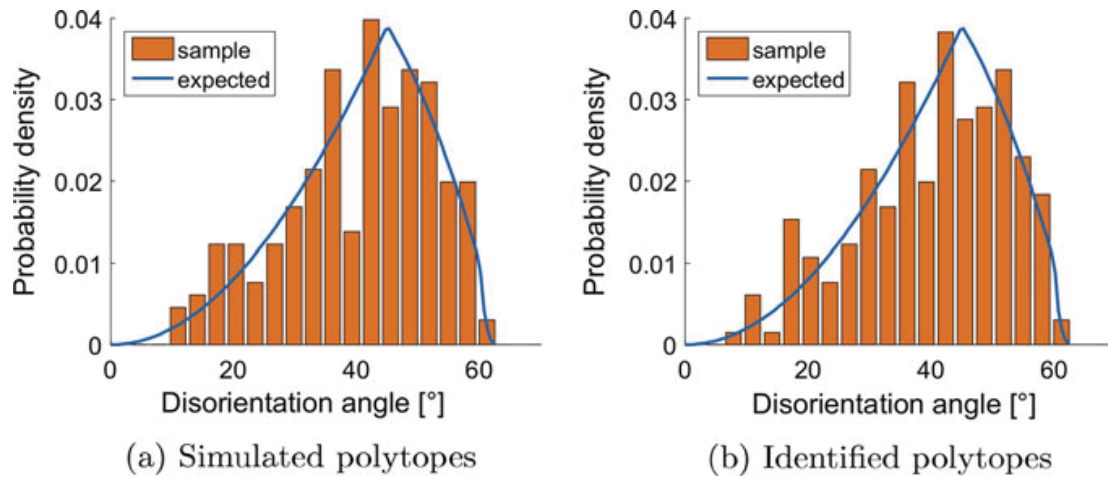


**Fig. 14** In both panels the theoretical probability density of disorientation angles according to Mackenzie and Thomson [31] is shown as a blue line. Panel **a** shows the disorientation angles obtained with exact rotation matrices of a simulated sample population. **b** shows the angles obtained with rotation matrices that were identified with the algorithm summarized in [4] of the same population as used for panel (a). (Reprinted with permission from [4], Copyright (2017) Elsevier)

Kovačević et al. [2] also describe how non-ideal cases in which the segmentation algorithm produced regions that could not be fitted with the algorithm described in Sect. 2.2 were treated.

In conclusion, this section describes how agglomerates can be represented in their full geometric complexity. A seeded watershed algorithm was applied to separate a measured particle into several segments. The segments were then merged under consideration of certain criteria to yield primary particles inside an agglomerate. Finally, the methods described in Sect. 2.2 were applied to describe each primary particle separately.

## 2.4 Disorientation Angles in Potash Alum Agglomerates

The procedures described in Sects. 2.2 and 2.3 enable the mathematical description of measured 3D crystal images. The mathematical description allows detailed analysis of the complex structures. One particular feature of crystal agglomerates which is accessible with the presented tools is the angle between the primary particles. To check whether there is a preferred orientation Kovačević et al. [4] used their techniques to measure disorientation angles between primary crystals in potash alum agglomerates comprising two primary particles. They compared the distribution of measured disorientations with simulated agglomerates that have randomly orientated primary particles. Agglomerates were represented using  $\mathcal{H}$ -representations as shown in Eq. (1). The simulated agglomerates also provided the opportunity to validate the algorithms described in Sects. 2.2 and 2.3.

Two primary crystals A and B were considered and it was assumed that B could be rotated into A by an arbitrary rotation matrix  $\tilde{\mathbf{R}}$ . If the crystal model of A and B has  $n_s$  symmetry operations, then the rotation of B into A can also be performed by additionally applying the  $n_s$  rotation matrices  $\tilde{\mathbf{R}}_i$  that perform a symmetry operation. This was possible because the symmetry operations do not change the appearance of the shape and thus give  $n_s$  identically-looking crystals. According to Mackenzie and Thomson [33], a disorientation angle  $\Theta$  is the smallest of angles  $\Theta_i$  which can be calculated for each rotation with

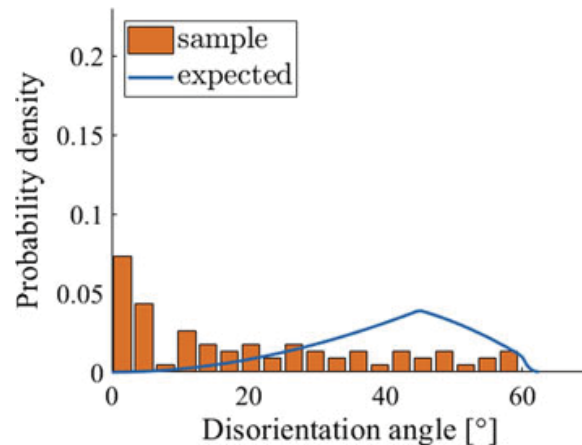
$$\Theta_i = \arccos \left( \frac{\text{tr}(\tilde{\mathbf{R}}_i \tilde{\mathbf{R}}) - 1}{2} \right) \quad (27)$$

In this work, potash alum crystals were considered to be octahedral. For an octahedron, there are 24 symmetry operations. Thus, to compute the disorientation angle between two primary particles, one must first find the rotation matrix  $\tilde{\mathbf{R}}$  between these two primary crystals. This could be easily computed provided a shape fit for each primary particle. Then, 24 symmetry operations were applied and the 24 angles  $\Theta_i$  were computed according to Eq. (27). The disorientation angle is the smallest of these angles. A disorientation angle of  $0^\circ$  means that particles are oriented the same way.

In order to validate the algorithm, agglomerates were first simulated. For the simulated agglomerates, it was possible to compute the distribution of the disorientation angles because the rotation matrices of the simulated primary crystals were known exactly. Figure 14a shows the probability density of the resulting angles together with the theoretical distribution that would be expected to result from an infinite number of samples. This theoretical distribution is given in the literature for cubes and also holds for octahedra [33]. In the next step, simulated 3D images of these agglomerates were created and the disorientation angle was computed based on the shapes identified in the images. The result is shown in Fig. 14b. The comparison of Fig. 14a, b shows that the proposed algorithms work well for simulated ideal agglomerates and yield meaningful disorientation angles.

In a next step, a potash alum crystal population was grown in a lab scale reactor and sampled at the end of the crystallization. The agglomerates of these samples were visualized using  $\mu$ CT measurements. The 3D images were then processed with the algorithms described in Sects. 2.2 and 2.3. The segmentation procedure was adapted to include user-interaction steps which made the segmentation more accurate. The shape identification procedure was also adapted to work with asymmetrical crystals observed in the measurement. Then the disorientation angle of the agglomerates was calculated. Details on the experimental procedures are provided by Kovačević et al. [4]. Exemplary results are shown in Fig. 15. It was observed, that agglomeration of potash alum crystals tends to show lower disorientation angles than it was expected if randomly oriented particles form agglomerates. This expectation is shown by the blue line in Fig. 15, obtained from theoretical considerations in the literature. Kovačević

**Fig. 15** Disorientation angles of a population of 74 experimentally obtained potash alum agglomerates. (Reprinted with permission from [4], Copyright (2017) Elsevier)



et al. [4] further discriminate between two different types primary particle contact: *slightly touching* and *growth together*.

In conclusion, the methods described in Sects. 2.2 and 2.3 were applied to potash alum crystals to yield geometric representations of crystals. The main contribution of this work was to use these models to analyze the particles. By measuring the disorientation angle of primary particles in agglomerates—a measure that is inaccessible by traditional 2D imaging methods—it was demonstrated that 3D image analysis is a powerful tool for particle characterization.

### 3 Classifiers for Agglomerates

The previous sections deal with the exact characterization of crystal populations. This section follows a more basic approach where particles are only classified whether they are agglomerates or not. It is common that particle populations are characterized by a size distribution. A common way to measure particles size distributions is by dynamic image analysis. Therein size information is retrieved from image analysis of projections of a sample of particles from a bulk.

A bulk property that can be used to characterize the quality is the degree of agglomeration which represents the ratio of the number of particles that are agglomerates to total number of particles. The aim here was to additionally retrieve the degree of agglomeration from the same images used for particle size measurements.

The identification of the degree of agglomeration has been studied in Heisel et al. [5] by comparing artificial neural networks (ANN) and discriminant factorial analysis (DFA) with respect to their accuracy. Further a procedure to set up appropriate training sets and to select appropriate discriminant variables was proposed. The experimental work and the parts regarding DFA are conducted by the work group of Prof. Schembecker whereas the work concerning ANN has been conducted in the group of Prof. Briesen.

Projections of L-alanine and adipic acid crystals in suspension were obtained by dynamic image analysis. Example images can be seen in Fig. 16. For the scope of

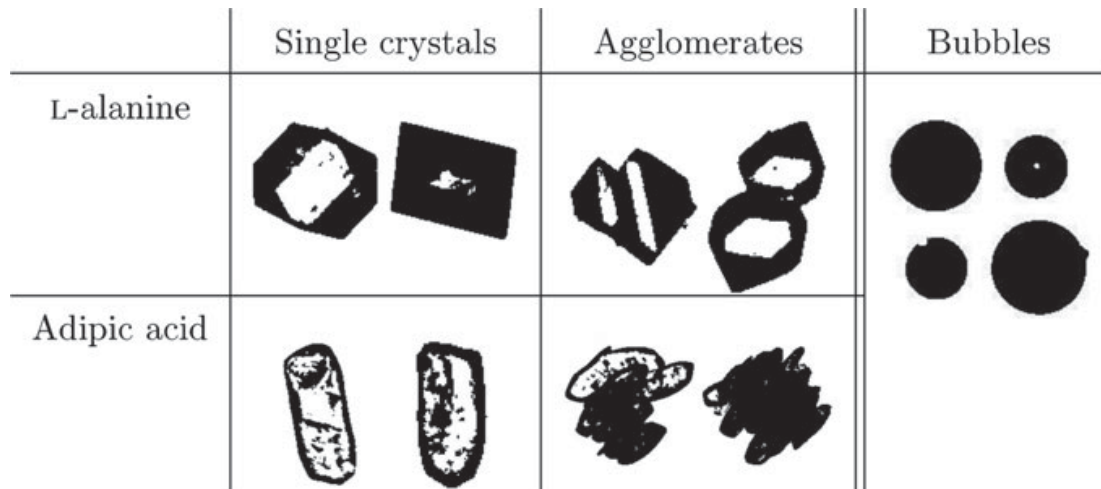


**Fig. 16** Example images of the three categories single crystals, agglomerates, and bubbles of both material systems L-alanine and adipic acid. (Reprinted with permission from [5], Copyright (2017) Elsevier)

this section it is important that the obtained images may contain images of crystals that either were (1) agglomerates or (2) single crystals. The images also contained (3) artefacts of measurements, specifically, gas bubbles (c.f. Fig. 16). For classification 19 image descriptors were studied. The image descriptors provided information about particle size and shape such as the area, equivalent diameter, or number of concavity points. A full list and description of how they can be calculated is provided by Heisel et al. [5].

The quality of the descriptors in respect to their potential to distinguish between the three classes was ranked using proportional similarity [34, 35]. This statistical tool yields the  $PS$  value that is one for two identical distributions and zero for two completely different distributions. One  $PS$  value that evaluates the potential to distinguish between single crystals and agglomerates was calculated ( $PS_{sa}$ ). Another  $PS$  value that evaluates the potential to distinguish between crystals and bubbles ( $PS_{cb}$ ) was calculated for each descriptor. These two values were used to rank the descriptors in respect to their potential in distinguishing between the classes.  $PS_{mn}$ —the mean of  $PS_{sa}$  and  $PS_{cb}$ —was also used to rank the image descriptors. Only the latter is considered in the present summary. For more results regarding the other two  $PS$  values see Heisel et al. [5].

To obtain three training data sets per material system, six crystallization experiments were conducted. From each experiment thousands of images were acquired of which the first 600 images of single crystals and 600 images of agglomerates were selected manually. These experiments produced only few images of gas bubbles. This is why 600 images of gas bubbles were created by a separate experiment with only water and extensive stirring. Using these 1800 images per experiment various training (TR), test (TE) sets were created. The training sets were *combined* training sets (C) if images of different experiments of one material system and gas bubbles were used, or *separate* training sets (S) if images of only one experiment and gas

bubbles were used. The training sets were also varied in total number of images between 27 and 1800.

The training sets were then used to train DFA and ANN classifiers. For evaluation of the performance of the classifiers, two quality criteria were introduced. The first one was the performance index  $PI_{All}$  which represents the fraction of correctly classified objects. The aim was to reach values above 0.9. The second value was the error made in the degree of agglomeration  $Ag$ . Since the test sets were made of the same number of agglomerated crystals and single crystals, the value for each test set was known to be  $Ag = 0.5$ . The error in degree of agglomeration  $\delta Ag$  made by the classifier was therefore defined as:

$$\delta Ag = \frac{|Ag_{classifier} - 0.5|}{0.5} \quad (28)$$

This value should be below 0.1 for a well-trained classifier. Some exemplary results for the material system adipic acid/water and the ANN classifier are summarized in Fig. 17.

Both ANN and DFA are able to accurately distinguish between the three classes. Figure 17 shows that there are only three descriptors necessary to classify images with ANN. For DFA 7 descriptors are necessary.

Heisel et al. [5] discuss that training a DFA classifier is easier than that of an ANN classifier. However, DFA needs more descriptors. Which leads to the conclusion that ANN is an attractive alternative if much effort needs to be put in the development of calculation procedures of the image descriptors. It was further shown that PS is a powerful tool to select appropriate image descriptors even for the classification into three classes. It was also discussed that the classifiers could be used for different

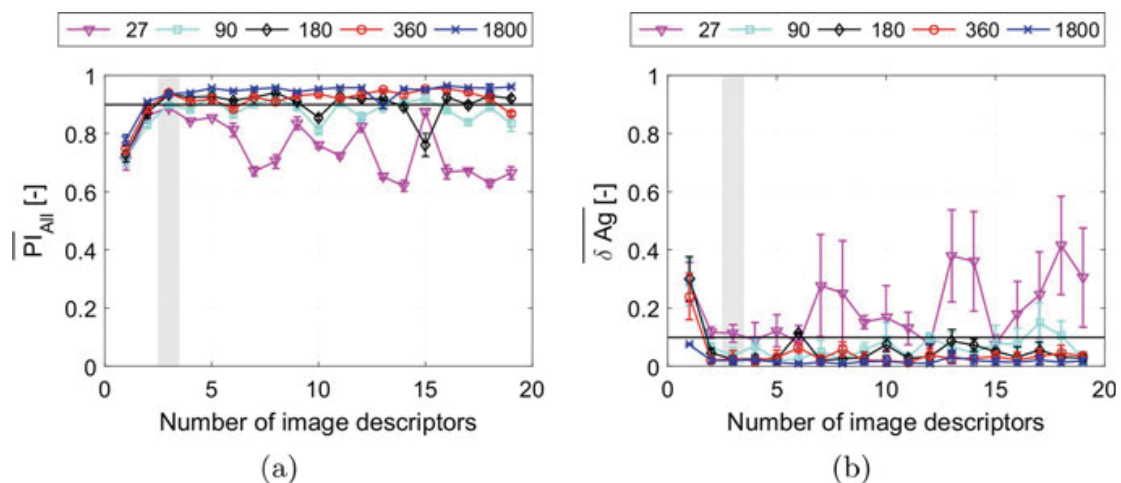


**Fig. 17** Results for a ANN classifier for different numbers of image descriptors (in order of their PS rank) and number of samples in the training data sets (27, 90, 180, 360 or 1800). Gray areas indicate the number of image descriptors necessary to reach the predefined classification quality (horizontal black lines). Error bars indicate standard deviations compared between different test sets. (Reprinted with permission from [5], Copyright (2017) Elsevier)

experimental conditions. That is, provided the size of the particles remains similar to the particles in the training set. It was proposed to optimize the developed procedure so that it works for differently sized particles, too.

## 4 Modelling of Crystallization with Consideration of Morphology

The previous sections explain how crystal morphology can be mathematically described or classified into categories. This section focuses on the effects of complex morphology on growth of single crystals and agglomerates.

For simulations of crystallization processes it is common to assume populations of crystals that can be described with only one size parameter (e.g. diameter for spherical particles) [36]. However, Fig. 11 shows that this a bad assumption for complex crystalline structures and complex single crystals (Fig. 3 left-hand side). The problem with this assumption is that one can often not correctly describe both the volume and the surface area of crystals at the same time with only one size parameter. Authors then often chose volume-equivalent diameters to model e.g. growth of the crystals because so at least the mass is conserved. However, growth depends on the surface area that is available for growth. Therefore, significant inaccuracies are introduced by simplifying the morphology of crystals.

### 4.1 Modelling of the Growth of Faceted Crystals

Reinhold and Briesen [8] addressed the growth of potash alum crystals under consideration of their morphology. The behavior of populations—such as crystals in suspensions—is frequently modeled with population balance models [37]. A simplified version that considers only growth of a constant number of particles can be written as [8]:

$$\frac{\partial n}{\partial t} + \nabla(gn) = 0 \quad (29)$$

where  $n$  is the number density distribution of a population of, in this case, crystals and  $g$  is the growth rate of crystal surfaces. Equation (29) describes the problem studied by Reinhold and Briesen [8]: 26-faced potash alum crystals (as shown in Fig. 1) were considered to grow in an ideally mixed batch crystallizer. A constrained  $\mathcal{H}_C$ -representation was employed to reduce the dimension of the face distances to seven entries in  $\mathbf{h}_C$ . This means that the growth rate  $g$  in Eq. (29) was actually a vector with seven entries that each described the growth rate of one crystal face group. Therefore, the number density distribution also features seven internal coordinates.

Even though only growth was considered in this model equation, its solution is not trivial.

Because growth rates depend on the supersaturation which is again dependent on the volume of the crystals, a solution of the problem involved the evaluation of the integral for the total volume of the population. The integral for the volume can be generalized for any geometric property of the crystals  $\mu$  and can be written as

$$I_{\mu}(t) = \int \mu(\mathbf{h}_C) n(\mathbf{h}_C, t) d\mathbf{h}_C \quad (30)$$

Because of the high dimension of the problem the solution becomes numerically challenging. It was solved using a Monte Carlo method that calculated solutions at  $n_{\text{sample}}$  random points  $\mathbf{h}_{C,i}$ . The probability functions  $w(\mathbf{h}_{C,i}, t)$  of these points were assumed to be known. Then the integral in Eq. (30) was estimated by [38, 39]

$$I_{\mu}(t) \approx \frac{1}{n_{\text{sample}}} \sum_i \mu(\mathbf{h}_{C,i}) \frac{n(\mathbf{h}_{C,i}, t)}{w(\mathbf{h}_{C,i}, t)} \quad (31)$$

Based on a simplified model with only three faces, for which an analytical solution is available, Reinhold and Briesen [8] describe which effect the choice of the initial probability function  $w(\mathbf{h}_{C,i}, 0)$  and  $n_{\text{sample}}$  has on the accuracy of the numerical integration. They finally conclude that

$$w(\mathbf{h}_C, 0) = \frac{1}{2} \left( \frac{\mu_{\text{volume}}(\mathbf{h}_C)}{I_{\text{volume}}(0)} + \frac{1}{I_1(0)} \right) n_0(\mathbf{h}_C) \quad (32)$$

was a reasonable choice that balances between the relative errors for the volume and surface area integration.  $n_{\text{sample}} = 2 \times 10^4$  was determined to be a sufficient number of samples for the Monte Carlo integration to achieve relative errors below  $10^{-3}$  at reasonable computational cost.

To be able to numerically solve the partial differential Eq. (29) it needed to be transferred to a system of ordinary differential equations. This was done employing the method of characteristics. For details refer to Reinhold and Briesen [8].

With these parameters the growth of a batch of  $7.66 \times 10^7$  26-faced potash alum crystals was simulated over a time span of 1 h. The initial distribution of the constrained face distances  $\mathbf{h}_C$  was chosen as a multivariate Gaussian normal distribution with mean face distances of 10  $\mu\text{m}$  and 1  $\mu\text{m}$  standard deviation. The growth rates were taken from the literature [40] and vary between 0.2 mm/s for the (100) and (010) faces and 6 mm/s for the (111) faces. These different growth rates led to the disappearance of the fast-growing crystal faces during growth (Fig. 18); which has an influence on the growth of the particles—and, therefore, also on the course of supersaturation—that could not be modeled with growth models that do not consider each face separately.

To determine which faces were disappearing during simulation it was important to detect face distances that would result in faces that were outside of a crystal. The

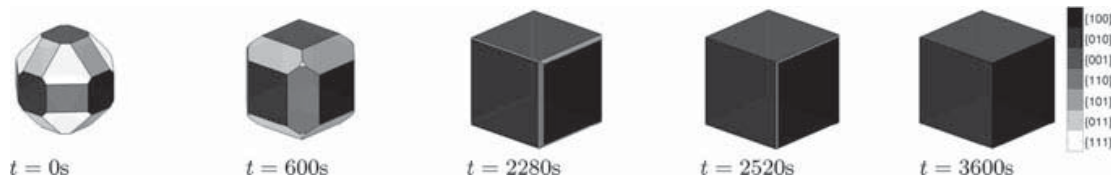


**Fig. 18** Visualization of the evolution of one  $h_{C,i}$  vector over the course of the simulation. (Reprinted with permission from [8], Copyright (2015) Elsevier)

concept is illustrated for a 2D case in Fig. 10 and is discussed by Reinhold and Briesen [11]. In context of this work Reinhold and Briesen [8] described how they detected that face distances became too large and limited their growth accordingly.

The evolution of the constrained face distances of a single crystal of the simulated population is displayed in Fig. 19. The corresponding surface areas of the same crystal are displayed in Fig. 20. It can be observed that the fast growing (111) face was initially able to grow with its maximum growth rate until its surface area became very small. Then its growth rate was limited by the growth of the (110), (101), and

**Fig. 19** Evolution of the face distances of a single crystal over the course of the simulation. (Reprinted with permission from [8], Copyright (2015) Elsevier)

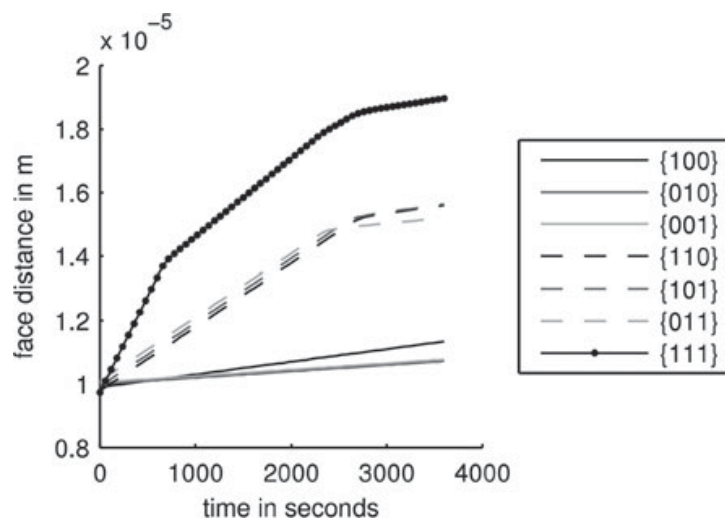


**Fig. 20** Evolution of the surface areas of specific crystal faces over the course of the simulation. (Reprinted with permission from [8], Copyright (2015) Elsevier)

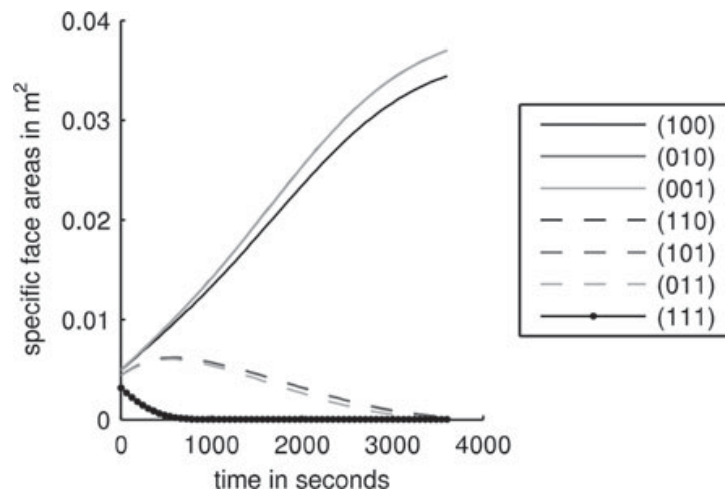
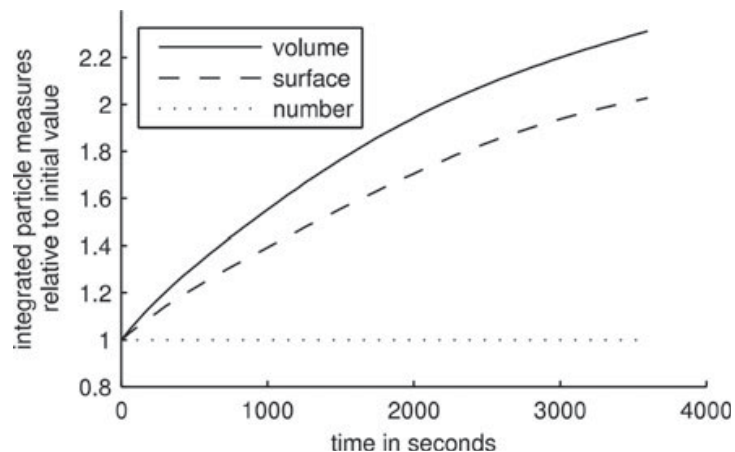


**Fig. 21** Evolution of the total number, surface area and volume relative to their corresponding initial values. (Reprinted with permission from [8], Copyright (2015) Elsevier)



(011) faces. Once also these areas became small due to the slow growth of the (100), (010), and (001) faces the growth of all faces was limited through the growth rates of these faces.

The population balance model also yielded the evolution of the total area and volume of all crystals of the population. The evolution of the volume and area of all crystals relative to the initial condition is displayed in Fig. 21. Note that the number of crystals remained constant because neither agglomeration nor breakage were modeled.

In conclusion, it was demonstrated how a population balance model for face-specific growth of single crystals can be solved. For the solution it was necessary to estimate integrals in a high dimensional space. This was achieved with a Monte Carlo based scheme, that allows to determine the error of the integral estimate. To solve the differential equations, the method of characteristics was applied. The accuracy of the method was evaluated based on a lower dimensional problem for which an analytical solution is available. It was further applied to solve a high dimensional population balance model for the growth of single potash alum crystals under consideration of their full morphology. It was thereby demonstrated that disappearing faces have an impact on the growth of the crystals that could not be modeled by conventional crystal models.

## 4.2 Modelling of the Growth of Crystal Agglomerates

While Reinhold and Briesen [8] focused on the growth of single crystals, Kovačević and Briesen [3, 6] studied agglomeration and growth of crystals. The challenge was that upon agglomeration of two primary particles the agglomerate should be described in a way that preserves both the surface area and the volume of the primary particles. In conventional models it is often assumed that upon agglomeration a new particle is generated that has a single size parameter (e.g. a diameter or a face distance as shown in Fig. 22) that preserves the volume of the two primary particles. The area

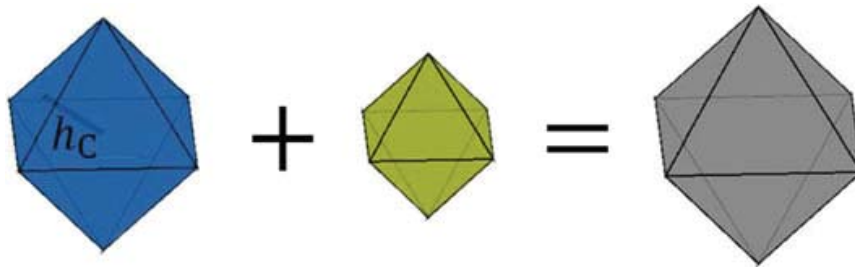


**Fig. 22** Agglomeration following the simple approach: When the blue and green crystal agglomerate the volume equivalent grey crystal is generated. The surface area is way too smaller than the sum of the surface areas of the constituting primary particles. (Reprinted with permission from [6], Copyright (2019) American Institute of Chemical Engineers)

is then calculated for the larger particle. This introduces a high error for the surface area and therefore for subsequent growth of the agglomerate.

Kovačević and Briesen [6] studied three different modeling approaches: The first one, the *simple approach*, represents the state of the art in which only the volume of particles is conserved after agglomeration (Fig. 22). The second approach is called the *2D approach* where a 2D population balance equation that considers particle volume and area as internal coordinates was set up. Therein both particle volume and surface area are conserved upon agglomeration. However, modeling the growth rate of the surface was not as straightforward as the increase of volume by additive agglomeration. The third method they studied was a Monte Carlo based, highly accurate, but also very computationally expensive method that was previously published by Briesen [41] and adapted for the agglomeration of octahedral potash alum crystals in Kovačević and Briesen [3]. It describes agglomerates with their full morphological complexity and was therefore able to accurately describe both the volume and surface area of agglomerates (Fig. 23). This was made possible by using the appropriate functionality of the MATLAB framework of Reinhold [42] and the cdd library [43]. This *complex method* was also used to parametrize the 2D approach.

The complex approach considers a sample number of crystals that was assumed to be representative for the whole population that was to be simulated. It was computationally expensive to calculate the volume of the agglomerates, which makes the method infeasible for simulations of long process times [3].

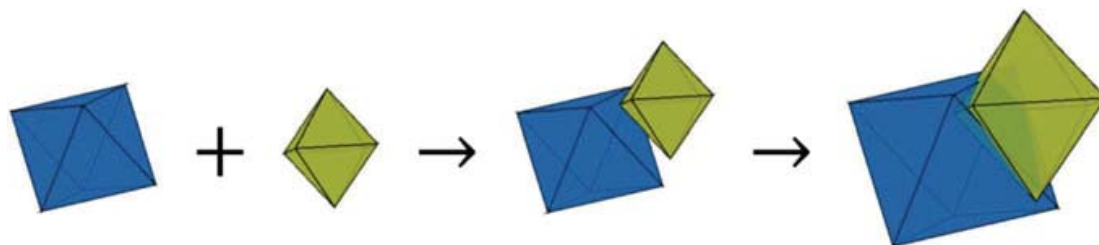


**Fig. 23** Aggregation following the complex approach: The agglomerate is described with its full geometric complexity. (Reprinted with permission from [6], Copyright (2019) American Institute of Chemical Engineers)

With the 2D approach a compromise was made between the complex and simple approach. A 2D population balance is more complex to solve than a 1D one, but still leads to a manageable computational effort. The corresponding 2D population balance equation that describes growth and agglomeration can be written as [44–46]

$$\begin{aligned} & \frac{\partial f(V, A)}{\partial t} + \frac{\partial(G_V f(V, A))}{\partial V} + \frac{\partial(G_A f(V, A))}{\partial A} \\ &= \frac{1}{2} \int_{V'=0}^V \int_{A'=0}^A \beta f(V - V', A - A') f(V', A') dA' dV' \\ & - f(V, A) \int_{V'=0}^V \int_{A'=0}^A \beta f(V', A') dA' dV' \end{aligned} \quad (33)$$

$f(V, A)$  is the 2D crystal size distribution with the volume  $V$  and surface area  $A$  as internal coordinates. The growth terms  $G_V$  and  $G_A$  describe the increase of particle volume and area through growth respectively.  $\beta$  is the agglomeration rate kernel. Upon agglomeration it is easy to add the volume and surface area of the two primary crystals to yield their respective values for the agglomerate. The increase of the volume can easily be derived from face displacement rates. However, it was not as straightforward to model the growth of the surface area.

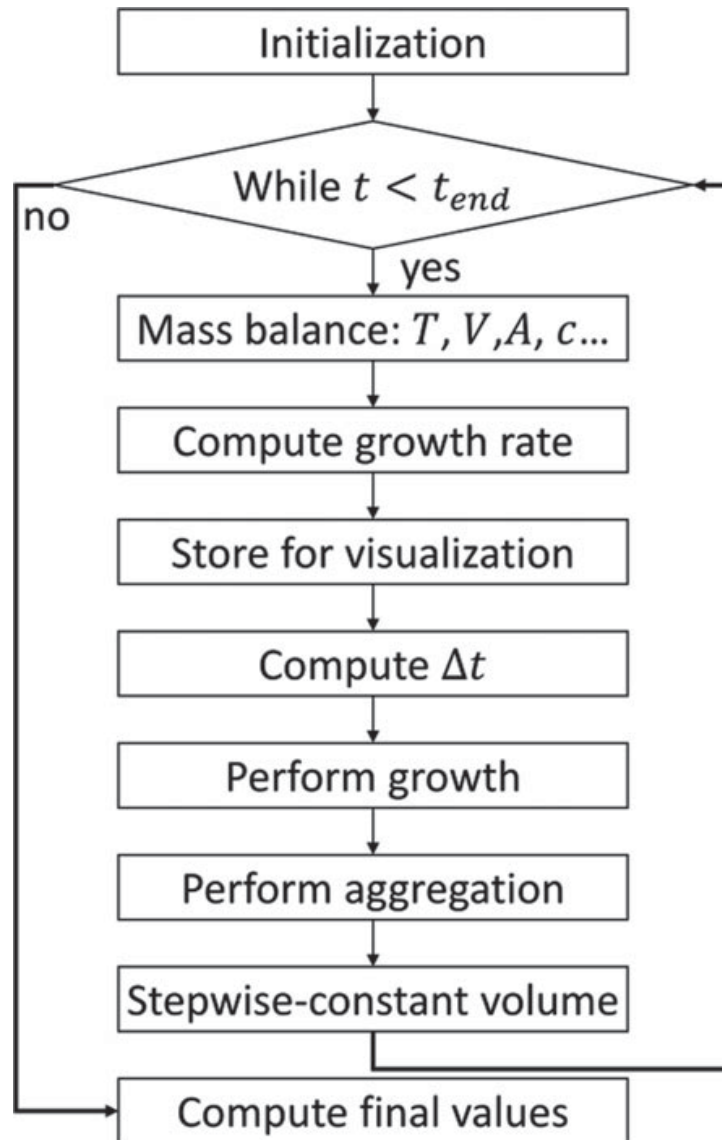
All of the three approaches were solved with the same numerical scheme to ensure that no numerical differences of the results could occur. The solver was an event-driven Monte Carlo approach that determines time steps according to agglomeration events. Between the time steps constant supersaturation was assumed and used to calculate growth. The procedure is summarized in Fig. 24.

In the initialization step an initial crystal population that was assumed to be representative for the population in the process was generated. Octahedral potash alum crystals were described with one size parameter, the constrained face distance  $h_C$  (displayed in Fig. 22). A number of  $N_{\text{part}}$  crystals with normally distributed face distances and uniformly distributed orientations was generated to be further simulated. The respective orientations were held constant throughout the simulation. The particles existed in a small control volume  $V_{MC}$  that was chosen so that the number density concentration in the control volume was the same as in the total suspension volume.

Following the initialization, the main simulation loop was entered by evaluating mass balances. This yielded the present supersaturation that is the driving force for growth. Based on the supersaturation the face displacement rates were calculated according to literature [47]. It was assumed to be constant in each time step.

The length of such a time step was determined based on agglomeration events. It was assumed that all particles have the same probability to agglomerate (constant  $\beta = \beta_0$ ) for some calculations. For others a shear rate and particle size dependent agglomeration rate kernel was introduced according to Briesen [48]. For the constant

**Fig. 24** The numerical solver of all three simulation approaches. (Reprinted with permission from [6], Copyright (2019) American Institute of Chemical Engineers)



agglomeration kernel, the agglomeration rate was calculated from the agglomeration kernel and was also dependent on the size of the control volume and the number of crystals in it:

$$r = \beta_0 \left( \frac{N_{part}}{V_{MC}} \right)^2 \quad (34)$$

This means that, on average, in 1 s  $rV_{MC}$  particles will agglomerate, which again means that the average time step size is  $\overline{\Delta t} = (rV_{MC})^{-1}$ . For the Monte Carlo solver, the time step size was sampled from an exponential distribution according to [49]

$$\Delta t = -\overline{\Delta t} \cdot \ln(x) \quad (35)$$

where  $x$  is a uniformly distributed random number between 0 and 1. The calculation of the time steps for the shear rate dependent agglomeration kernel was more complex and explained in detail by Briesen [48] and Kovačević and Briesen [6].

With the time step size at hand, growth of the particle population was calculated. For the simple and complex approach this was done in a straightforward way with  $h_{C,new} = h_C + \Delta t G_h$  for each particle in the simple approach or with  $h_{C,part\ new,i} = h_{C,part,i} + \Delta t G_h$  for each face distance  $i$  of each primary particle for the complex approach.

The population balance of the 2D approach did not directly contain the face distances. The growth was modeled based on the growth of the volume and surface area directly:  $V_{new} = V + \Delta t G_V$  and  $A_{new} = A + \Delta t G_A$ . The growth rate of the volume is given as  $G_V = A G_h$ . Until this point  $G_A$  remained unknown. An empirical relation with the parameters  $p_1$  and  $p_2$  was proposed:

$$G_A = p_1 A^{p_2} V^{\frac{1-2p_2}{3}} G_h \quad (36)$$

Kovačević and Briesen [6] derived that for single crystals  $p_1$  is in fact a function of  $p_2$ . For octahedral particles the following function was found:

$$p_1 = \frac{24\sqrt{3}}{(12\sqrt{3})^{p_2} (4\sqrt{3})^{\frac{1-2p_2}{3}}} \quad (37)$$

$p_1$  and  $p_2$  can be interpreted as geometric factors that are specific for certain geometries and do not only differ depending on whether a particle is an agglomerate or not, but also on the geometry of each individual agglomerate. Kovačević and Briesen [6] studied various values for  $p_1$  and  $p_2$  and find that—even though the values slightly vary for different simulation cases—reasonable average values can be found to describe particles in a process. To study different parameters, they used the complex method to generate 1000 *isolated agglomerates*. The term *isolated* stems from the fact that they are not simulated within a reaction environment.  $p_1$  and  $p_2$  are only dependent on the geometry. How a certain geometry is reached is not important for their calculation. To produce a set of agglomerates, two particles were brought to contact. Subsequently their face distances were displaced in several steps without consideration of a supersaturation. Therefore, the time-consuming calculation of the mass balances was not necessary. After each face displacement step, both volume and area were calculated and then allowed a correlation between growth rate by means of face displacement, and the change of the surface area. The procedure is illustrated in Fig. 25.

With  $p_2 = 1.135$  a hypothetical crystallization process was simulated with the scheme displayed in Fig. 24. The results are shown in Fig. 26. The agglomeration kernel was chosen relatively high compared to a real crystallization problem to make the effect of agglomeration clearer.

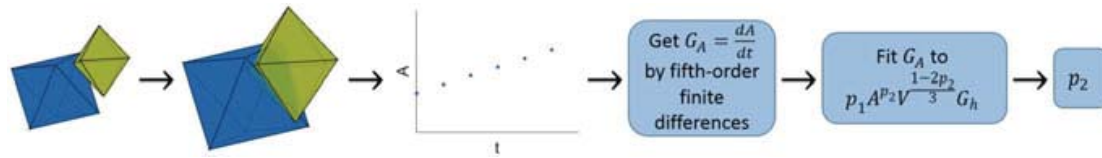


**Fig. 25** Illustration of the procedure to determine  $p_2$ : First particles are brought to contact, then their faces are displaced in several steps  $t$  which produces an increase in the surface area  $A$  of their agglomerate. The growth rate of the surface area is determined and used to calculate  $p_2$  from Eq. (37). (Reprinted with permission from [6], Copyright (2019) American Institute of Chemical Engineers)

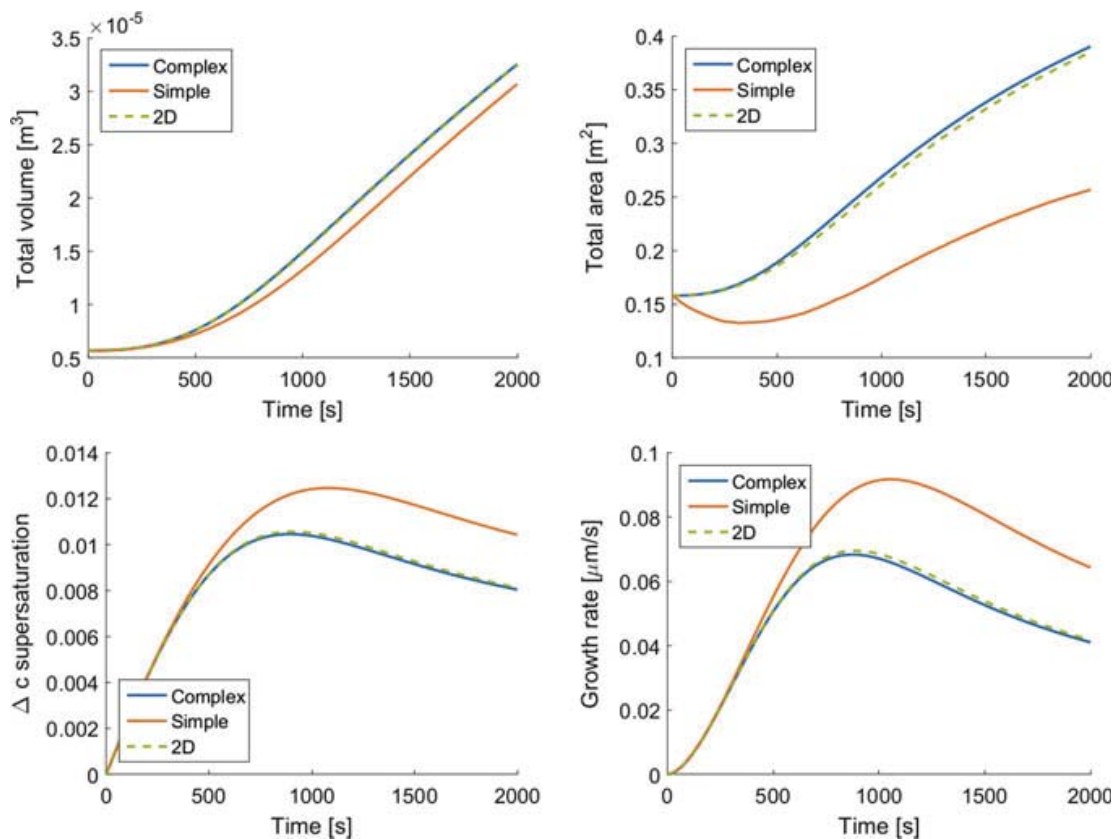


**Fig. 26** Simulation results for the complex (blue line), simple (orange line), and 2D (green dashed line) approaches with a constant agglomeration kernel. (Reprinted with permission from [6], Copyright (2019) American Institute of Chemical Engineers)

Figure 26 shows the evolution of the volume of the crystals (top left), the total surface area (top right), the supersaturation (bottom left) and the growth rate (bottom right). It can be seen that the 2D approach is able to reproduce the results of the complex approach, while it used much less computational recourses. It further strikes that even though the simple approach makes a relative error of up to two compared to the complex approach when calculating the surface area, the supersaturation, and the growth rate, the total volume was calculated quite accurately. The reason for this is that due to the underestimation of the surface area, less material was built into

the crystals. This led to a higher supersaturation, which again led to higher growth rates. These higher growth rates were therefore able to compensate for the error that is made for the surface area.

In conclusion, a procedure to accurately model agglomeration and growth of crystals with a 2D population balance was proposed. The population balance equation considers the volume and surface area of the particles as internal coordinates and was therefore able to conserve both of these values upon agglomeration. The growth is also expressed with respect to growth of volume and area. The second subsection summarizes how both of these rates can be determined. While the growth rate of the volume was determined on a straightforward way, the growth rate of the surface area needed to be estimated with a Monte Carlo based scheme. The scheme proposed here was applied for potash alum crystals but is formulated in a way that it can be applied to other material systems.

## 5 Integrated Crystallization Modelling in Dyssol

The crystallization models proposed in the previous sections are able to describe the crystallization phenomena growth and agglomeration in an accurate way; however, they are computationally expensive. They are, therefore, with currently available hardware hardly suitable for process simulations that span long process times and include complex flowsheets. There are, however, simpler crystallization models available in the literature, that are able to describe several crystallization phenomena simultaneously, and have less computational cost. A case study on the implementation of such a crystallization process within Dyssol was presented by Kulozik et al. [7].

Kulikov et al. [50] study the performance of the dynamic flow sheet integration platform CHEOPS [51]—that is in some ways similar to Dyssol—based on an integrated crystallization flowsheet. Therefore, a similar process was implemented for Dyssol and compared to the results of Kulikov et al. [50]. The main difference between CHEOPS and Dyssol is that CHEOPS is used to couple models that are generated in different simulation environments. Dyssol now allows simulations in one combined software package that can be used to model each unit operation and couple different unit operations to form a flowsheet.

The flowsheet of Kulikov et al. [50] contains four units: (1) a mixed suspension mixed product removal (MSMPR) crystallizer, (2) a hydrocyclone, (3) an evaporator and (4) an ideal mixer. For all of the units a model was implemented in Dyssol. They were then combined to an integrated flowsheet and Dyssol was used to simulate the behavior of this exemplary process over a process time of 72 h. The first two of the mentioned units will be briefly explained in the following sections. The mixer is considered trivial and is not explained. It accepts two feed streams that are ideally mixed to a product stream of the mixer. The evaporator is implemented in a way that a constant ratio of pure solvent is withdrawn to concentrate its feed. It has a vapor stream and a concentrate stream as outputs.

## 5.1 MSMPR Crystallizer

The central equation of the mixed suspension mixed product removal (MSMPR) crystallizer model is again a population balance equation. In this case growth of spherical particles (diameter  $d$ ) with a growth rate  $G$ , and nucleation with a birth rate  $B$  were considered. In addition, the crystallizer accepts a feed stream and has a vapor and a product stream as output.

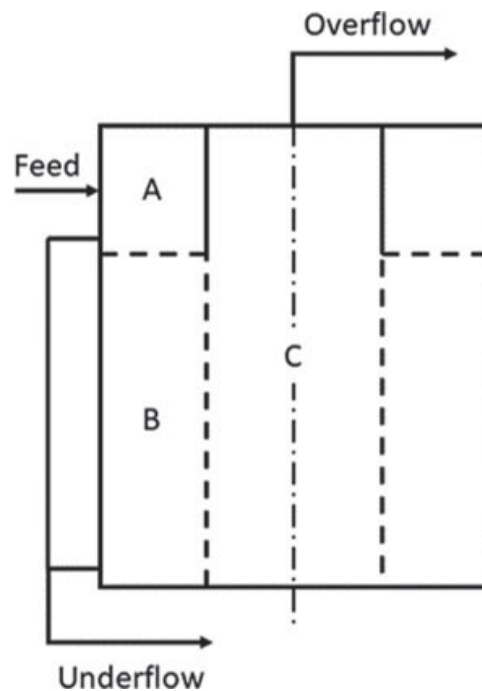
$$\frac{\partial n(d)}{\partial t} + \frac{\partial(G(d)n(d))}{\partial d} + \frac{1}{V} \sum_j^{n_{streams}} (n_j(d)\dot{V}_j) + n(d)\frac{d \ln V}{dt} = \frac{\partial B(d, n)}{\partial d} \quad (38)$$

Growth and nucleation kinetics were as proposed by Jones and Mydlarz [52]. The discretization as done with the method of classes and a flux limiter was used as proposed by Qamar [53]. Additionally, mass balances were introduced. The resulting set of differential algebraic equations is then solved using Dyssol [54].

## 5.2 Hydrocyclone

The implementation of the hydrocyclone is based on the work of Braun [55] and the descriptions of Kulikov et al. [50]. The static model proposed by Braun divides a hydrocyclone into four zones (c.f. Fig. 27): Zone A is a tube-like inlet zone to which a suspension is fed and forced onto a circular downward movement. The suspension then enters an outer tube-like zone B where the fluid continues to move downward on

**Fig. 27** Abstraction of the hydrocyclone as proposed by Braun [55]



its circular path. Inside the outer zone B Braun considers a cylindrical inner zone C where the fluid moves upwards towards the outlet where the overflow is withdrawn.

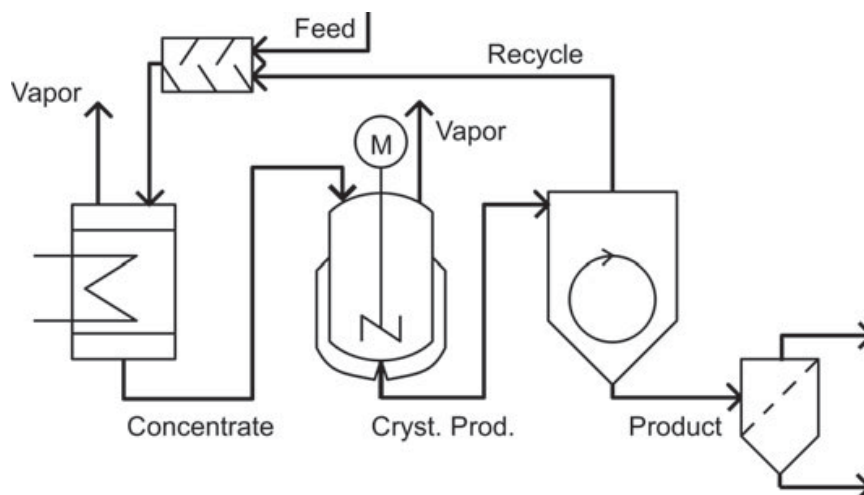
The model assumes material transport between the zones that is dependent on particle sizes. Larger particles are drawn to the outer wall by centrifugal force and are added to the underflow if they are large enough to touch the outer wall of the zones A and B. Particles that reach the top of zone C are added to the overflow. The reflux parameter  $R_f = \frac{\dot{V}_{\text{overflow}}}{\dot{V}_{\text{feed}}}$  is used to define which proportion of a feed suspension is leaving the cyclone through the overflow.

### 5.3 Flowsheet and Simulation Results

The units were combined to a flowsheet as shown in Fig. 28: Feed material is mixed with a recycle stream and then concentrated in an evaporator. The concentrate is fed to the crystallizer where vapor is withdrawn at a constant rate to induce crystallization. The product suspension is then classified in the hydrocyclone. The fine fraction is recycled and the coarse product leaves the process. For this study the material system water/potash alum was used.

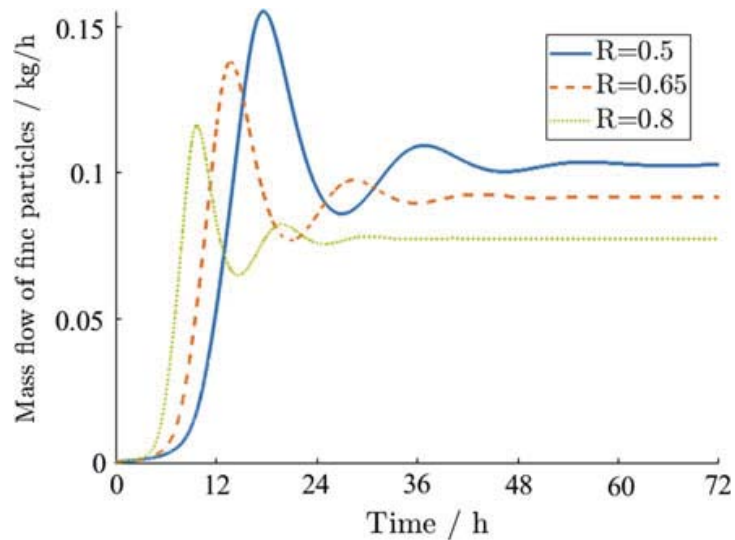
For a simulation scenario, a sieve or filter unit at the end of the process was assumed but not included in the model. It is further assumed, that this unit should not be fed with a product that is too fine to prevent blocking. This scenario is also studied by Kulikov et al. [50]. The goal of the simulation is, therefore, to reduce the mass stream of fine particles ( $d < 50 \mu\text{m}$ ). Here, the effects of the reflux ratio  $R_f$  (as also studied by Kulikov et al. [50]) and the feed stream were studied.

Figure 29 shows that after the start of the process, the mass stream of fines rapidly raised, reached a maximum and finally approaches an equilibrium state. For higher



**Fig. 28** Crystallization flowsheet with reflux. The sieve is not considered in the model but used in the optimization discussion

**Fig. 29** Mass stream of fine particles dependent on reflux ratio. The feed mass stream was 0.5 kg/s

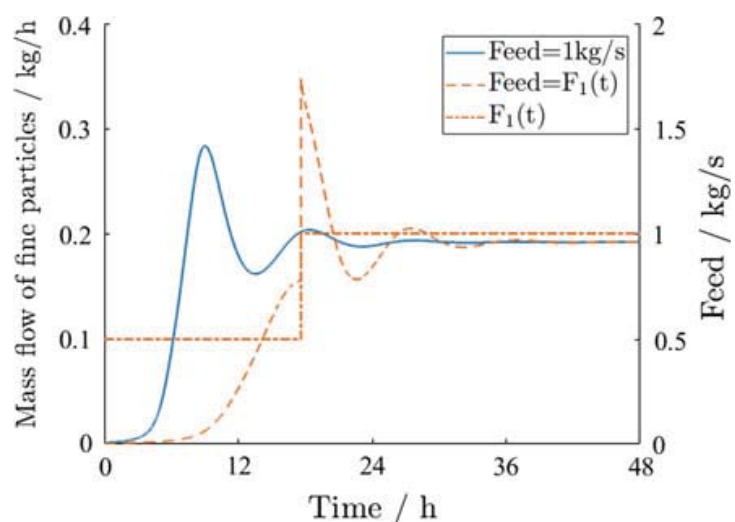


reflux ratios less fine particles were contained in the product. This is also observed by Kulikov et al. [50] for a different material system.

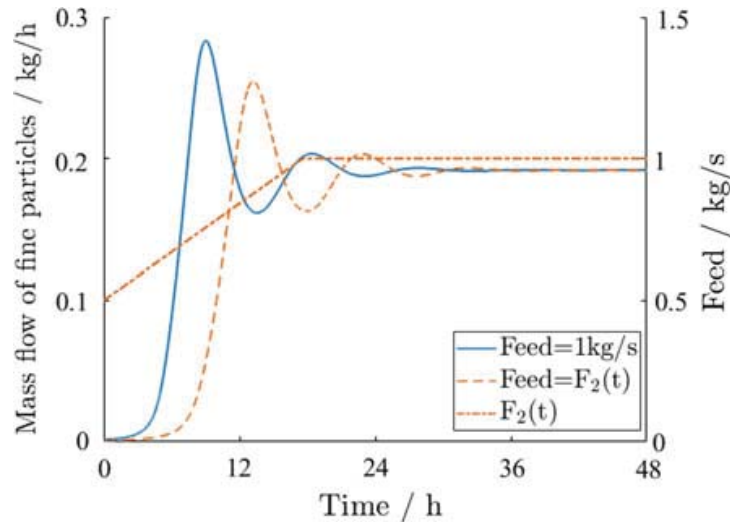
Figure 29 suggests that for all cases the highest mass flows of fine crystals can be observed within one day after startup of the process. A further simulation goal was to reduce the maximum mass flow by appropriate adaption of the feed stream. For this case the reflux ratio was fixed to 0.5. The simulation result for this reflux ratio and a feed mass stream of 1 kg/s was used as a benchmark (blue solid lines in Figs. 29, 30, and 31). In a first attempt, the feed rate was kept at only 0.5 kg/s for the first 18 h and was then rapidly increased to 1 kg/s.

Figure 30 shows that this procedure led to a slower increase of the mass stream of fine particles. Once the feed rate was increased a sharp increase in the mass stream of fine particles was observed. The peak was higher than in the benchmark simulation. It rapidly decreased and converged towards the expected equilibrium. A second simulation was done where the feed stream was gradually increased from 0.5 to 1 kg/s within 18 h (c.f. Fig. 31). In this case it was observed that the peak of

**Fig. 30** Simulation result for a rapidly increased feed rate (orange dashed line) and comparison to the benchmark result (blue solid line)



**Fig. 31** Simulation result for a gradually increased feed rate (orange dashed line) and comparison to the benchmark result (blue solid line)



the mass flow of fine particles was delayed and was not as pronounced as for the benchmark. The equilibrium was still reached at a similar time.

In conclusion, it was demonstrated that Dyssol can be used to dynamically simulate crystallization flowsheets. Even complex cases such as reflux streams can be handled and Dyssol can be used for long process time calculations.

## 6 Conclusion

Sections 2 and 3 deal with the analysis of crystal morphology. Section 4 focuses on the modelling of crystallization under consideration of morphology and discusses errors that are made by the classical assumptions that neglect morphology. Finally, in Sect. 5 a crystallization process was modeled using the dynamic flowsheet simulator Dyssol and it was shown that it can be efficiently used to dynamically simulate integrated flowsheets.

The analysis of crystal morphology is often done by 2D on-line image analysis in both industry and science. It was demonstrated that certain errors with respect to morphology have to be accepted when only 2D information is available. This concept has been demonstrated for the measurement of a roundness parameter of abraded crystals. It was further demonstrated that morphological bulk properties such as the degree of agglomeration can be extracted from particle projections. Procedures for the calibration of artificial neural networks were proposed.

To overcome the limitations of measurements where only 2D information is available, 3D particle images were acquired and analyzed. It was demonstrated that the full morphological information that was provided by 3D particle description can be used to measure properties that are inaccessible from 2D images—such as disorientation angles in agglomerates. Even though 3D image acquisition and analysis are much

more sophisticated than of 2D images, the proposed methods help to understand morphological influences on important phenomena like crystal growth, agglomeration and breakage.

Another aspect of the work was the modeling of crystallization under consideration of the influence of morphology. Using a high dimensional population balance model the important influence of multiple surfaces with different growth rates on crystal growth was demonstrated. For the effective solution of such a model, novel numerical methods have been developed. It is common practice to neglect the combined influence of agglomeration and growth on the surface area of crystal populations. It was herein demonstrated that this introduces high errors in such models. A method was proposed to parametrize a population balance model that considers both the evolution of crystal volume and area correctly. Because such models are still numerically challenging and computationally expensive even if not included in a flowsheet, they are currently not suitable for simulation of integrated flowsheets. Therefore, a simpler model was included in the simulation platform Dyssol. It is demonstrated that Dyssol can be used to efficiently calculate integrated crystallization processes.

## References

1. Kovačević, T., Reinhold, A., Briesen, H.: Identifying faceted crystal shape from three-dimensional tomography data. *Cryst. Growth Des.* **14**(4), 1666–1675 (2014)
2. Kovačević, T., Schock, J., Pfeiffer, F., Briesen, H.: Shape identification of primary particles in potash alum aggregates using three-dimensional tomography data. *Cryst. Growth Des.* **16**(5), 2685–2699 (2016)
3. Kovačević, T., Briesen, H.: Determining the full geometric complexity of crystal aggregates via Monte Carlo Simulation. In: *PARTEC: International Congress of Particle Technology*, Nuremberg, pp. 19–21 (2016)
4. Kovačević, T., et al.: Disorientation angle distribution of primary particles in potash alum aggregates. *J. Cryst. Growth* **467**, 93–106 (2017)
5. Heisel, S., Kovačević, T., Briesen, H., Schembecker, G., Wohlgemuth, K.: Variable selection and training set design for particle classification using a linear and a non-linear classifier. *Chem. Eng. Sci.* **173**, 131–144 (2017)
6. Kovačević, T., Briesen, H.: Simulations of crystal aggregation and growth: towards correct crystal area. *AIChE J.* **65**(5) (2019)
7. Kulozik, S., Buchholz, M., Kovačević, T., Haus, J., Heinrich, S., Briesen, H.: Dynamic flowsheet simulation of a crystallization reactor with material recovery via a hydrocyclone. In: *PARTEC 2019*, Nuremberg, VDI Verlag (2019)
8. Reinhold, A., Briesen, H.: High dimensional population balances for the growth of faceted crystals: combining Monte Carlo integral estimates and the method of characteristics. *Chem. Eng. Sci.* **127**, 220–229 (2015)
9. Reinhold, A., Schorsch, S., Mazzotti, M., Briesen, H.: Modeling and measurement of abraded particles. *Powder Technol.* **271**, 134–140 (2015)
10. Ma, C.Y., Wang, X.Z., Roberts, K.J.: Morphological population balance for modeling crystal growth in face directions. *AIChE J.* **54**(1), 209–222 (2008)
11. Reinhold, A., Briesen, H.: Convex geometry for the morphological modeling and characterization of crystal shapes. *Part. Part. Syst. Character.* **28**(3–4), 37–56 (2012)
12. Borchert, C., Sundmacher, K.: Morphology evolution of crystal populations: modeling and observation analysis. *Chem. Eng. Sci.* **70**, 87–98 (2012)

13. Singh, M.R., Verma, P., Tung, H.-H., Bordawekar, S., Ramkrishna, D.: Screening crystal morphologies from crystal structure. *Cryst. Growth Des.* **13**(4), 1390–1396 (2013)
14. Schneider, R.: *Convex Bodies: The Brunn-Minkowski Theory*. Cambridge University Press, Cambridge (2008)
15. Al-Rousan, T., Masad, E., Tutumluer, E., Pan, T.: Evaluation of image analysis techniques for quantifying aggregate shape characteristics. *Constr. Build. Mater.* **21**(5), 978–990 (2007)
16. Hentschel, M.L., Page, N.W.: Selection of descriptors for particle shape characterization. *Part. Part. Syst. Charact.* **20**(1), 25–38 (2003)
17. Masad, E., Button, J.W.: Unified imaging approach for measuring aggregate angularity and texture. *Comput.-Aided Civil Infrastruct. Eng.* **15**(4), 273–280 (2000)
18. Pons, M.N., et al.: Particle morphology: from visualisation to measurement. *Powder Technol.* **103**(1), 44–57 (1999)
19. Burger, W., Burge, M.J.: *Principles of Digital Image Processing, Undergraduate Topics in Computer Science* (2009)
20. Schorsch, S., Ochsenbein, D.R., Vetter, T., Morari, M., Mazzotti, M.: High accuracy online measurement of multidimensional particle size distributions during crystallization. *Chem. Eng. Sci.* **105**, 155–168 (2014)
21. Gahn, C., Mersmann, A.: Brittle fracture in crystallization processes Part A. Attrition and abrasion of brittle solids. *Chem. Eng. Sci.* **54**(9), 1273–1282 (1999)
22. Briesen, H.: Model-based analysis of the effect of particle and impact geometry on attrition of brittle material. *Powder Technol.* **178**(2), 87–98 (2007)
23. Briesen, H.: Two-dimensional population balance modeling for shape dependent crystal attrition. *Chem. Eng. Sci.* **64**(4), 661–672 (2009)
24. Gorski, K.M., et al.: HEALPix: a framework for high-resolution discretization and fast analysis of data distributed on the sphere. *Astrophys J* **622**(2), 759–771 (2005)
25. Naruse, Y.: HEALPix Library for Matlab. 1.0 ed (2011)
26. Neubeck, A., Van Gool, L.: Efficient non-maximum suppression. In: Presented at the 18th International Conference on Pattern Recognition (ICPR'06) (2006)
27. WAHBA, G.: A least-squares estimate of satellite attitude, Problem 65–1. *SIAM Rev.* **7** (1965)
28. Markley, F.L.: Attitude determination using vector observations and the singular value decomposition. *J. Astronaut. Sci.* **36**(3), 245–258 (1988)
29. Fernández, G., Kunt, M., Zrýd, J.P.: A new plant cell image segmentation algorithm. In: *Image Analysis and Processing (Lecture Notes in Computer Science)*, pp. 229–234 (1995)
30. Indhumathi, C., Cai, Y.Y., Guan, Y.Q., Opas, M.: An automatic segmentation algorithm for 3D cell cluster splitting using volumetric confocal images. *J. Microsc.* **243**(1), 60–76 (2011)
31. Vincent, L., Soille, P.: Watersheds in digital spaces: an efficient algorithm based on immersion simulations. *IEEE Trans. Pattern Anal. Mach. Intell.* **13**(6), 583–598 (1991)
32. Gonzales, R.C., Woods, R.E., Eddis, S.L.: *Digital Image Processing Using Matlab*, 2nd ed. McGraw Hill Education, India (2010)
33. Mackenzie, J.K., Thomson, M.J.: Some statistics associated with the random disorientation of cubes. *Biometrika* **44**(1–2), 205–210 (1957)
34. Vegelius, J., Janson, S., Johansson, F.: Measures of similarity between distributions. *Qual. Quant.* **20**(4) (1986)
35. Renkonen, O.: *Statistisch-ökologische Untersuchungen über die terrestrische Käferwelt der finnischen Bruchmoore*. Dissertation, Societas zoologica-botanica Fennica Vanamo (1938)
36. Omar, H.M., Rohani, S.: Crystal population balance formulation and solution methods: a review. *Cryst. Growth Des.* **17**(7), 4028–4041 (2017)
37. Ramkrishna, D.: *Population Balances*. Academic Press, San Diego (2000)
38. Kroese, D.P., Taimre, T., Botev, Z.I.: *Handbook of Monte Carlo Methods*. Wiley, Hoboken (2011)
39. Press, W.H., Teukolsky, S.A., Vetterling, W.T., Flannery, B.P.: *Numerical Recipes in C++, 2 ed.* Cambridge University Press, Cambridge (2007)
40. Snyder, R.C., Doherty, M.F.: Faceted crystal shape evolution during dissolution or growth. *AIChE J.* **53**(5), 1337–1348 (2007)

41. Briesen, H.: Hierarchical characterization of aggregates for Monte Carlo simulations. *AIChE J.* **52**(7), 2436–2446 (2006)
42. Reinhold, A.: *Crystal Shape Modeling and Convex Geometry—Analysis of Geometric State Spaces*. Dissertation, Fakultät Wissenschaftszentrum Weihenstephan, Technische Universität München (2015)
43. Fukuda, K.: *cdd library*, 094 g ed (2012)
44. Wright, D.L., McGraw, R., Rosner, D.E.: Bivariate extension of the quadrature method of moments for modeling simultaneous coagulation and sintering of particle populations. *J. Colloid Interface Sci.* **236**(2), 242–251 (2001)
45. Kraft, M.: Modelling particulate processes. *KONA Powder Part J.* **23**, 18–25 (2005)
46. Zucca, A., Marchisio, D.L., Vanni, M., Barresi, A.A.: Validation of bivariate DQMOM for nanoparticle processes simulation. *AIChE J.* **53**(4), 918–931 (2007)
47. Kim, D.Y., Yang, D.R.: A novel method for measurement of crystal growth rate. *J. Cryst. Growth* **373**, 54–58 (2013)
48. Briesen, H.: Aggregate structure evolution for size-dependent aggregation by means of Monte Carlo simulations. *KONA Powder Particle J.* **25**, 180–189 (2007)
49. Fichthorn, K.A., Weinberg, W.H.: Theoretical foundations of dynamical Monte Carlo simulations. *J. Chem. Phys.* **95**(2), 1090–1096 (1991)
50. Kulikov, V., Briesen, H., Grosch, R., Yang, A., von Wedel, L., Marquardt, W.: Modular dynamic simulation for integrated particulate processes by means of tool integration. *Chem. Eng. Sci.* **60**(7), 2069–2083 (2005)
51. Schopfer, G., Yang, A., von Wedel, L., Marquardt, W.: CHEOPS: A tool-integration platform for chemical process modelling and simulation. *Int. J. Softw. Tools Technol. Transfer* **6**(3), 186–202 (2004)
52. Jones, A.G., Mydlarz, J.: Continuous crystallization of potash alum: MSMPR kinetics. *Canadian J. Chem. Eng.* **68**(2), 250–259 (1990)
53. Qamar, S., Elsner, M.P., Angelov, I.A., Warnecke, G., Seidel-Morgenstern, A.: A comparative study of high resolution schemes for solving population balances in crystallization. *Comput. Chem. Eng.* **30**(6–7), 1119–1131 (2006)
54. Skorych, V., Dosta, M., Hartge, E.-U., Heinrich, S.: Novel system for dynamic flowsheet simulation of solids processes. *Powder Technol.* **314**, 665–679 (2017)
55. Braun, B.: *Theoretische und experimentelle Untersuchungen des Einflusses der Feststoffkonzentration und der Partikelgrößenverteilung auf das Trennverhalten von Hydrozyklonen*, Dissertation, Universität Braunschweig (1989)



## Chapter 5

### Results

#### 5.1 Paper II: Analysis of Nonideal Shape Evolution during Potash Alum Crystallization Using Microcomputed Tomography and Three-Dimensional Image Analysis (Schiele et al. 2021a)

##### Summary

Today crystallization processes and crystalline bulk materials are analyzed using 2D image analysis. The advantage of such methods is that they are fast and can be applied in-line. However, a major drawback is that they are fundamentally not able to capture the exact shape of crystals. It has been discussed before in this text that crystal shape is, however, an important property. In consequence, previous work of the Briesen group focused on the development of 3D imaging and image analysis methods. 3D images contain full shape information. This study focuses for the first time on the 3D analysis of crystal populations and their evolution instead of the appearance of single crystals. While previously only roughly 100 crystals have been analyzed, in this study, 11 000 crystals were analyzed in 3D. To achieve this, the experimental and image analysis methods had to be optimized. By sorting crystals into 3D-printed scaffolds, almost 800 crystals could be included in a single  $\mu$ CT scan. This also led to higher total crystal masses in each measurement and crystal mass could be considered for binarization. Statistical considerations based on 2D imaging revealed that for the present case roughly 1000 crystals should be analyzed to represent a population well. The high number of crystals per  $\mu$ CT scan then enabled analysis of the evolution of 3D crystal populations over the course of a batch cooling crystallization process. This yielded volume and surface distributions and their evolution without the need for any assumptions regarding crystal morphology. This is already a great achievement because volume and surface area are two important coupled process variables that are hard to determine using other analysis methods. Further analysis was enabled by the application of 3D crystal models. This analysis revealed an unexpected shape shifting phenomenon. Seed crystals were damaged and mostly not faceted. They grew to entirely faceted crystals within the first 30 min of the process. These crystals, however, were unexpectedly not fully symmetric according to their cubic unit cell. The shapes shifted towards the expected symmetry over the course of the experiment. However, most crystals never reached ideal symmetry. Shape shifting is explained by face independent growth in the study. However, the employed model did not explain the existence of the non-ideal shapes. The hypothesis was that the asymmetries resulted from the damaged and often asymmetric seed material. A further analysis of this hypothesis is conducted by Schiele et al. (2021b).

##### Author contributions

H. Briesen came up with the idea for this work. S. Schiele developed the experimental and image analysis methods, conducted all experiments, the evaluation of the experiments, the modelling, and the simulations. F. Antoni and R. Meinhardt helped developing the experimental and image analysis methods. S. Schiele supervised the work of F. Antoni and R. Meinhardt. H. Briesen supervised all work. The article was written by S. Schiele with help by R. Meinhardt. H. Briesen corrected and proofread the article.

##### Copyright

The following section is reprinted with permission from (Schiele et al. 2021a). Copyright 2021 American Chemical Society.



# Analysis of Nonideal Shape Evolution during Potash Alum Crystallization Using Microcomputed Tomography and Three-Dimensional Image Analysis

Simon A. Schiele, Felix Antoni, Rolf Meinhardt, and Heiko Briesen\*

Cite This: *Cryst. Growth Des.* 2021, 21, 1751–1761

Read Online

ACCESS |



Metrics &amp; More

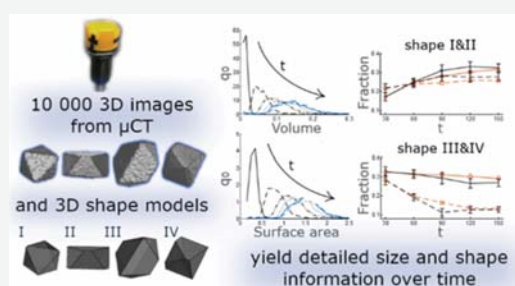


Article Recommendations



Supporting Information

**ABSTRACT:** Nowadays, it is common to analyze crystallization processes and crystalline products using two-dimensional image analysis. Various techniques exist but they are not fundamentally capable of capturing the full morphology of particles due to their limitation in two dimensions. This is particularly true when complex shapes, e.g., through agglomeration or broken crystals, occur. Here, an approach is presented in which potash alum crystals are sampled from a laboratory-scale reactor at six time points over the course of a crystallization process. Three-dimensional (3D) images of all crystals in the samples were obtained by microcomputed tomography and used for morphological characterization. The method directly yields volume and surface area distributions without the need for any assumption regarding particle morphology. Applying geometric crystal models allowed for a more detailed analysis of the crystals. In the example considered, it was shown that most crystals assumed nonideal shapes over the course of the process. The supporting model provides indication that the shapes approach ideality through face-independent crystal growth. Overall, more than 11 000 crystals were analyzed. In general, this work aims at demonstrating the potential of crystal analysis by means of microcomputed tomography and 3D image analysis.



## 1. INTRODUCTION

Shape is an important quality feature of a crystalline product. It not only affects the efficiency of downstream processes in production<sup>1,2</sup> but also has significant influence on the bioavailability of pharmaceuticals.<sup>3,4</sup> Also, in the case of metal nanocrystals, crystal morphology has a considerable influence on the material properties.<sup>5</sup> In the framework of crystal shape engineering,<sup>6,7</sup> researchers have attempted to design crystallization processes to produce specific crystal shapes and sizes. Consequently, significant effort was also made to experimentally analyze crystal shapes and sizes. In most cases, size measurements build upon some kind of shape assumption or shape measurement. It is, for example, common to assume spherical shapes and then measure sizes of particles as diameters. However, crystals express faceted shapes and are usually not well represented by spheres. Some crystals may be well described by cubes. In such cases, the side length is a good measure for size. However, in many other examples, crystals have more complex shapes that need more sophisticated shape models. Consequently, methods for size and shape measurements are closely related.

Focused beam reflectance measurement (FBRM) is a robust method for inline particle analysis.<sup>8</sup> It measures a chord length using the time that a laser with known velocity needs to pass over a particle. Such chord lengths can either be directly used as size information or transformed into more meaningful size

measures by applying either geometric shape models<sup>9,10</sup> or empirical models.<sup>11</sup> They can also be used to distinguish between different crystal shapes.<sup>12</sup> However, because of the inherent nonuniqueness of the measured chord for a given crystal, it is difficult to evaluate sizes of nonuniform particles.<sup>9,10</sup> Most methods yielding shape information rely on two-dimensional (2D) image analysis.<sup>13,14</sup> These techniques allow for an estimation of the size and shape of particles. Assumptions regarding morphology may help to make more accurate measurements.<sup>15,16</sup> However, because of the limitation to two dimensions, exact results are still difficult to achieve. Therefore, authors have attempted to increase the information content and/or the dimensionality of their measurements. For example, the combination of FBRM and 2D image analysis has been applied.<sup>17</sup> Another method is stereoscopic imaging that uses two orthogonal 2D images and assumptions regarding morphology for online crystal analysis.<sup>18,19</sup> A similar method where binocular inline imaging is used for three-dimensional (3D) reconstruction of particles

Received: December 4, 2020

Revised: January 20, 2021

Published: February 4, 2021



was developed by Huo et al.<sup>20</sup> These advanced methods provide a better understanding of the appearance of crystals. However, they are still unable to capture their exact shapes. Kovačević et al.<sup>21</sup> discuss that these limitations are particularly challenging to overcome when concave particles, such as agglomerates, occur. In the past few years, our group has worked on the development of an inherently 3D method for crystal analysis.<sup>21–24</sup> The method uses microcomputed tomography ( $\mu$ CT) to capture 3D images of crystals. These images contain detailed size and shape information of the particles. Assumptions regarding the morphology of the crystals then allow for fitting geometric crystal models to measured particles.<sup>21</sup> This includes, but is not limited to, agglomerates. On the basis of these models, analysis of the crystals in ways that were impossible with only 2D information became feasible. Kovačević et al.<sup>23</sup> studied the disorientation angle distribution between primary particles in agglomerates. In our previous studies,<sup>21–24</sup> the number of crystals analyzed by 3D imaging has been limited to the order of  $10^2$  crystals. This was mainly because only few crystals could be included in the time-consuming  $\mu$ CT measurements.

In the present study, we were able to increase the number of crystals to be analyzed by  $\mu$ CT toward about  $10^4$  crystals analyzed in total by improving the experimental procedure. This for the first time allows for the study of crystal populations instead of single crystals. It also enables the analysis of a time evolution instead of a single end point. To illustrate the potential of the availability of such population information over time, the method is applied to comprehensively analyze the evolution of the crystals' shape over time in a laboratory-scale crystallization process of potash alum (PA). This study sheds light on the shape evolution of nonideal crystals over time.

## 2. MATERIALS AND METHODS

All concentrations are expressed as loads with the unit gram PA hydrate per gram water.

**2.1. Materials.** PA ( $\geq 99\%$  Ph. Eur.), ethanol ( $\geq 99.8\%$ ), and cellulose Rotilabo-round filter type 113A were purchased from Carl Roth GmbH & Co. KG (Germany). For 50 vol % ethanol solutions, ethanol was diluted with deionized water. PA seed material was obtained by sieving (200–315  $\mu$ m) the material that was bought. Acetone ( $\geq 99.5\%$  Ph. Eur.) was purchased from Sigma-Aldrich Chemie GmbH (Germany).

**2.2. Crystallization.** All crystallization experiments were conducted in an OptiMax 1001 Synthesis workstation (Mettler Toledo Inc.) with 500 mL of reactor volume. For inline process analysis, an FBRM probe (Mettler Toledo Inc.) and an inline microscope (particle vision and measurement, PVM; Mettler Toledo Inc.) were installed in the reactor. For sampling suspension, a stainless steel pipe with an inner diameter of 7.5 mm was also installed.

A 300 g amount of deionized water was added to the reactor together with 73.01 g of PA for each experiment. The corresponding load was  $w = 0.2434$  g/g, which is the amount soluble in water at 40 °C.<sup>23</sup> Kovačević et al.<sup>23</sup> give the saturation concentration as a function of temperature

$$w_{\text{sat}}(T) = 0.18 \frac{\text{g}}{\text{kg K}^2} T^2 - 102.726 \frac{\text{g}}{\text{kg K}} T + 14\,760.7 \frac{\text{g}}{\text{kg}} \quad (1)$$

Subsequently, the temperature was increased to 45 °C over the course of approximately 20 min, and the stirrer (diameter 4.5 cm, four blades, pitched down) was set to 300 rpm. The rationale behind this choice of stirrer speed is given in Appendix I. After complete dissolution (FBRM counts  $< 10$ ), the temperature was decreased to 39 °C (10.1 K/min) and 3 g of the seed material was manually added to the reactor (within approximately 10 s). This marked the start of the

crystallization process to be monitored. The temperature was decreased at a constant rate of 10 K/h until it reached 20 °C. The temperature was held for another 30 min, after which the reactor was turned off. This marked the end of the crystallization experiment.

**2.3. Sampling.** During crystallization, two kinds of samples were taken from the reactor: (A) samples for concentration measurements and (B) samples for the analysis of the crystal population. Each of these samples was taken every 30 min (corresponding to every 5 K). The concentration was additionally measured shortly before and after seeds were added.

Samples for concentration measurements were retrieved through an opening in the reactor lid with a syringe through a  $0.8 \times 120$  mm<sup>2</sup> needle (B. Braun Melsungen AG, Germany) with a volume of 2 mL. Ideal mixing of the liquid was assumed. Directly after sampling, the samples were filtered with 1  $\mu$ m syringe filters (Chromafil GF 100/25, Machery-Nagel GmbH & Co. KG, Germany) into sample tubes and stored for later analysis. Filtering ensured that as few crystals as possible were contained in these samples. In case solids precipitated during storage, they could be dissolved at 45 °C before measuring the concentration. Concentration measurements were performed by first diluting the samples by a factor of 1:25 (mass) with deionized water. Next, the conductivity was measured (703 Laboratory Conductivity Meter, Knick GmbH & Co., Germany), and the concentration was calculated according to our calibration (accuracy 0.9% for 95% confidence).

Sampling suspensions is more complex and discussed in the literature.<sup>25–28</sup> The results of these studies suggest that fast sampling velocities are beneficial and that for narrow particle size distributions, classification of particles seems to be a minor issue. Even if in this work the number of crystals to be analyzed at a single point could be increased significantly over previous investigations, the number is still limited. Significant effort has been put into development of a proper sampling routine to provide the best representativeness possible. To achieve comparability, all probes and the stainless steel pipe for sampling were mounted at the same height inside the reactor. This was the height of the 200 mL filling mark, which was the deepest the FBRM probe could reach. The tips of the probes were aligned on the same reference diameter (Figure 1). The probes and stainless steel pipe were evenly mounted over the whole circumference, which should result in similar flow conditions in their vicinity.

On the basis of the procedures proposed by Genck<sup>27</sup> and Sha and Palosaari,<sup>28</sup> the suspension for crystal analysis was sampled using a vacuum. A plastic tube (inner diameter 4 mm, outer diameter 6 mm) to which a valve was attached was used. A syringe (25 mL, B. Braun) was attached at the other side of the valve. The tube was inside the aforementioned stainless steel pipe and filled with air during most of the experiment. This minimized the dead volume inside the reactor.

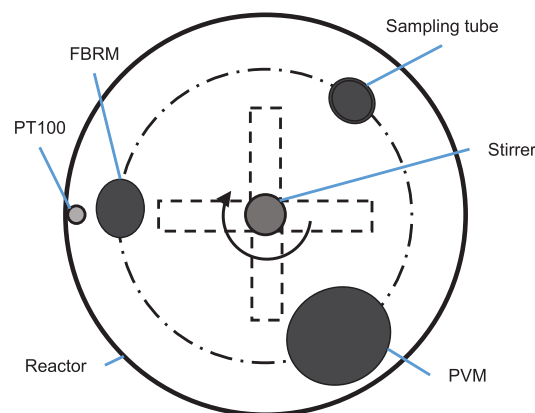


**Figure 1.** Schematic of the position of the instruments in the crystallization reactor. FBRM: focused beam reflectance method and PVM: particle vision and measurement. Note that the probes are mounted in an angle and therefore are displayed elliptically.

For sampling, the tips of the stainless steel pipe and the sampling tube were aligned inside the reactor. The valve was initially closed. The syringe was then used to generate a vacuum inside it ( $V = 6$  mL). The valve was rapidly opened, which equalized the pressure by sucking in a suspension sample. Next, the tube was withdrawn from the stainless steel pipe, and its contents were emptied onto a Buchner funnel with water-wetted cellulose filter paper on it. The liquid fraction of the suspension was removed using the filter and discarded. When all liquid was removed, the crystals were first washed with 50 vol % ethanol and then with acetone (both nonsolvents for PA). Afterward, the clean crystals were dried on the filter paper through natural evaporation of the remaining acetone. During the whole sampling and washing procedure, care was taken not to destroy any crystals and to produce as little new crystals through antisolvent addition as possible. This was achieved through careful removal of as much PA solution as possible before washing with ethanol.

To verify that the sampling method produced representative samples, a separate test crystallization process was conducted. After crystallization was completed, five samples were retrieved from the reactor and treated as described earlier (referred to as sample 1–5, later). Finally, the whole content of the reactor was also filtered, and the crystals were washed and dried (referred to as sample 6, later). All samples were separately analyzed using dynamic image analysis (DIA; QicPic, Sympatec GmbH, Germany). The analysis yielded projections of individual crystals for which each the diameter of a circle of equal projection area ( $d_{EQPC}$ ) was calculated by QicPic. Only particles with  $d_{EQPC} > 200$   $\mu\text{m}$  were considered because this was also the minimal size we aimed to analyze using  $\mu\text{CT}$ . The analysis of the crystals of sample 6 yielded about 59 000 diameters of individual particles and was therefore considered to perfectly represent the population (left, black curve in Figure 2). We chose a class size of  $\Delta x = 7.6$   $\mu\text{m}$  to

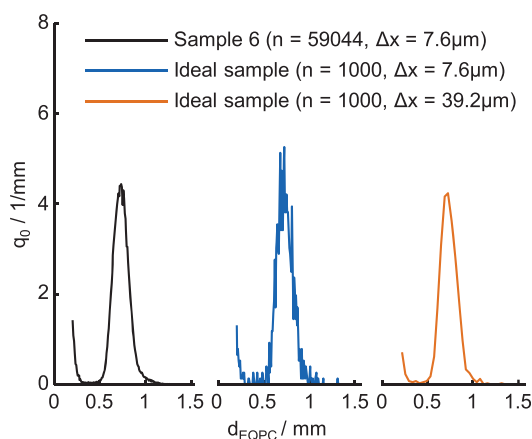


**Figure 2.** Distribution of the whole reactor content with 500 classes (left, black curve) and distributions of an ideal sample with 500 classes (center, blue curve) and 97 classes (right, orange curve).

represent this population (500 equally sized classes in the size interval of 0.2–4 mm). The other samples each yielded about 1000 projections and corresponding diameters. Note that the number of particles was higher than the number of projections in all samples because QicPic does not yield a projection for every particle. To estimate how effectively a sample of 1000 crystals could represent the whole population, a bootstrap method was applied.<sup>29</sup> A total of 100 different populations of 1000 randomly chosen crystals were created out of sample 6 (that contained about 59 000 crystals). These samples are referred to as ideal samples later because experimental sampling bias is excluded (i.e., the whole reactor content is considered). An example of such a population with the same class size as that of sample 6 is shown as a blue curve in Figure 2 (center). The ideal samples of 1000 crystals each could not adequately represent the population with the same class size as the much larger sample 6. To find a suitable class size for the ideal samples, the class size was

increased to minimize the squared difference between sample 6 and 100 different ideal samples. This procedure revealed that the ideal samples could represent sample 6 best with a class size of  $\Delta x = 39.2$   $\mu\text{m}$  (97 equally sized classes in the region of 0.2–4 mm). An example of an optimized distribution of an ideal sample is shown as an orange curve in Figure 2 (right).

The standard deviation and the mean of the ideal samples (blue curves in Figure 3; dashed lines indicate 95% confidence) can now

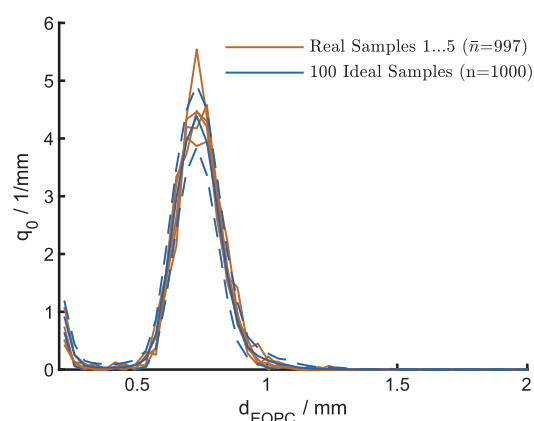


**Figure 3.** Accuracy that can be expected from samples of 1000 particles as estimated from 100 ideal samples (blue curves). The orange curves represent distributions of samples 1–5 that were retrieved from the reactor with the sampling methods described in this article. Dashed lines indicate 95% confidence.

also be used to evaluate the accuracy that can be expected from a sample of 1000 crystals when perfectly sampled from the real reactor. The orange curves in Figure 3 represent the five samples 1–5 that were taken from the reactor. The comparison of the curves reveals that most parts of the distributions of samples 1–5 lie within the 95% confidence interval of the ideal samples. In one sample, the main peak is slightly over-represented. Therefore, considering the sampling challenges mentioned earlier, these results indicate that the proposed sampling method produced good samples. The solid concentration obtained from samples 1–5 was  $0.11 \pm 0.02$  g solids per g solution ( $\pm 1$  standard deviation). The solid concentration of sample 6 was 0.11 g/g.

**2.4.  $\mu\text{CT}$  Measurements and Image Analysis.** 3D images were acquired using a custom-built X-ray microtomography system (XCT-1600HR; Matrix Technology AG, Germany). A total of 1600 radiographic 2D projections were obtained from various angles. The projections were used to reconstruct 3D images using a custom software (Matrix Technology) based on CERA (Siemens AG, Germany). These 3D images contained  $2008 \times 2008 \times 1250$  voxels and had a voxel spacing of 8  $\mu\text{m}$ . This means that the volume captured by one image was approximately  $16 \times 16 \times 10$   $\text{mm}^3$ . The time for obtaining one 3D image was approximately 1 h. Hence, a fundamental challenge for our work was to visualize as many crystals with one  $\mu\text{CT}$  image as possible. The method described by Kovačević et al.<sup>21</sup> was useful to examine about 20 large crystals; however, it was infeasible for larger populations. The aim here was to examine all crystals of each sample that was taken from the crystallization process. The samples visualized by  $\mu\text{CT}$  each had between 1300 and 2800 crystals. In addition, the aim was to prevent particles from being in contact during the  $\mu\text{CT}$  measurements. Thus, it would be assured that in the 3D images, connected particles were actually agglomerates and not particles that were in contact during measurement only. To achieve this goal, crystals were manually sorted into measurement scaffolds. Computer-aided design (CAD) models of the scaffolds are shown in Figure 4A and B. The scaffolds comprised plates that had cavities that were aligned in a grid. Each cavity had a squared cross section that was either sized  $2 \times 2$  or  $1 \times 1$   $\text{mm}^2$ . Their depths were

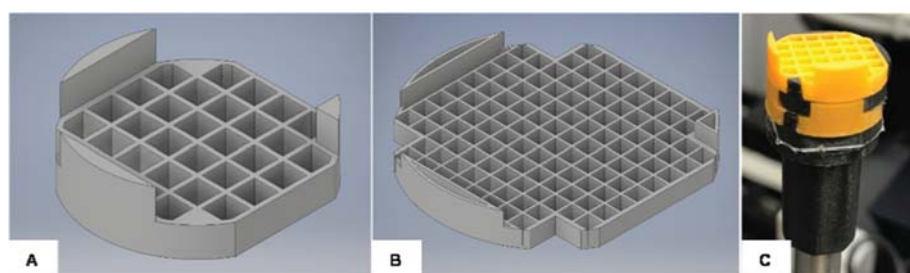


**Figure 4.** (A) CAD model of a  $\mu$ CT measurement scaffold with 32  $2 \times 2 \times 2$  mm<sup>3</sup> cavities. (B) CAD model of a  $\mu$ CT measurement scaffold with 128  $1 \times 1 \times 1$  mm<sup>3</sup> cavities. (C) Four stacked  $2 \times 2 \times 2$  mm<sup>3</sup> scaffolds inside the  $\mu$ CT.

either 2 mm for the larger cross sections or 1 mm for the smaller ones. Each scaffold contained either 32 ( $2 \times 2$  mm<sup>2</sup> cross section) or 128 ( $1 \times 1$  mm<sup>2</sup> cross section) cavities. The scaffolds were further designed such that they could be stacked (Figure 4C). Six 1 mm thick scaffolds could be fitted into one 3D image, resulting in 786 particles that could be included in one 3D image. The thin scaffolds with small cross sections were used as default, but the other ones had to be used for large particles. The scaffolds with  $2 \times 2$  mm<sup>2</sup> cross section were 3D-printed with an Ultimaker 3 (Ultimaker BV, the Netherlands using Innofil3D PET filament, BASF AG, Germany). For finer scaffolds, a more accurate Form 3 3D printer was used (Formlabs Inc., using clear Formlabs photopolymer resin FLGPCL02). Thus, with this procedure, only about four  $\mu$ CT measurements were necessary to visualize a population of 2000 crystals. Note that because crystals have to be manually sorted into the scaffolds using tweezers, this procedure excludes small crystals ( $<200$   $\mu$ m) from the analysis.

After images were obtained by  $\mu$ CT, 3D images of single particles were extracted from them. The procedure could be automatically performed in Matlab (version 2019a, Mathworks Inc.). The image analysis algorithm is summarized in Figure 5 and briefly described as follows. The first step was to apply an anisotropic diffusion filter (Matlab's *imdiffusefilt* function) to reduce blur but preserve edges. The next step was to find a global binarization threshold. It was chosen such that the mass of the crystals was conserved. For details on this step, check Appendix II. The threshold was then applied using Matlab's *imbinarize* function. An exemplary binary image is shown in Figure 6. An animation that better visualizes the 3D character of the images is provided in the Supporting Information.

To identify crystals in the binary images, connected regions were determined using Matlab's *bwconncomp* function (connectivity of 26). In a next step, all regions that had a volume less than the volume of a sphere with a diameter of 200  $\mu$ m were considered as blur and excluded from the image. Note that very small crystals were not included in the images because crystals were sorted manually using tweezers. We chose 200  $\mu$ m as the threshold for blur because the seeds were sieved with this mesh size. In some cases, the removal of blur resulted in a reduction of the volume greater than the volume corresponding to 0.05 mg (accuracy of the scale). In these cases, the threshold was recalculated using eq S1 (Appendix II) with the mass of blur  $m_{\text{blur}}$  that had previously been removed. Finally, the remaining regions were saved as individual 3D images for later analysis.

**2.5. Volume and Surface Area Determination.** The analysis of the 3D images of the crystals was performed in different levels of complexity. Previous methods for evaluation of the detailed geometry were based on geometric crystal models. Such an approach was also considered here (see Section 2.6). However, when crystallization processes are modeled, particle volume and surface area are already two important particle properties.<sup>30</sup> Using established particle analysis techniques, one would need the crystal shape to determine the volume and the surface area (Appendix III). However, at the same time, the shape is hard to predict. Using  $\mu$ CT particle analysis, the volume and the microscopic surface area can be directly extracted, without the need of any shape assumption. The volume  $V$  of each crystal was determined using eq 2

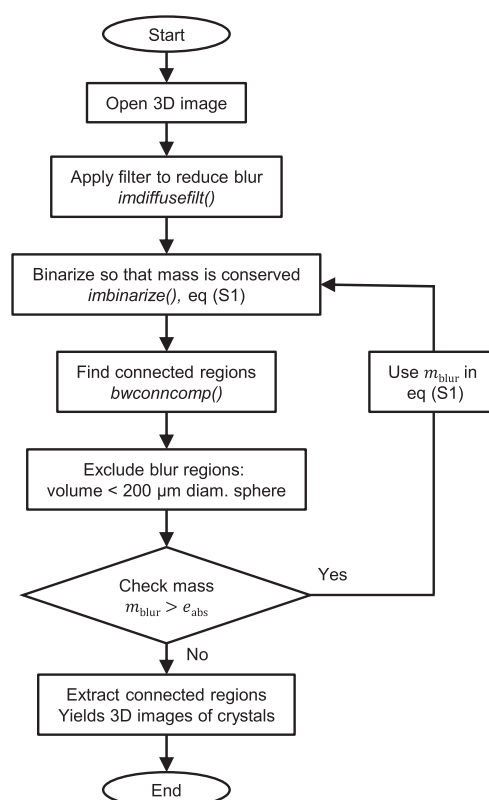


**Figure 5.** Algorithm to extract crystals from  $\mu$ CT images.  $e_{\text{abs}}$  is 0.05 mg.

$$V = \text{res}^3 \cdot n_{\text{voxel}} \quad (2)$$

where  $n_{\text{voxel}}$  is the number of voxels that describe the crystal and  $\text{res}$  is the voxel spacing of the image ( $\text{res} = 8$   $\mu$ m). Note that in a previous step, the mass of the crystals was used for binarization. Hence, the mass of crystals is preserved in each 3D image. Assuming an equal distribution of the error in mass over all crystals in an image, one can also assume that the mass, and therefore also the volume, is accurately determined for each individual crystal. The determination of the surface area is more complex. The  $\mu$ CT measurements had a voxel spacing of 8  $\mu$ m. Therefore, as a rule of thumb, it captures features that have a size of  $16 \times 16 \times 16$   $\mu$ m<sup>3</sup>. The microscopic shape of the particles is, therefore, captured. When the microscopic shape and volume are assumed to be accurate, the microscopic surface is also accurately captured. It must be noted that the features on the nanoscale such as surface roughness, steps in the crystal lattice, and dislocations are not captured but at the same time may have an impact on the surface area. Such features can be visualized with methods that offer sub-micrometer scale resolution, for example, atomic force microscopy.<sup>31</sup> However, such analysis is not the scope of

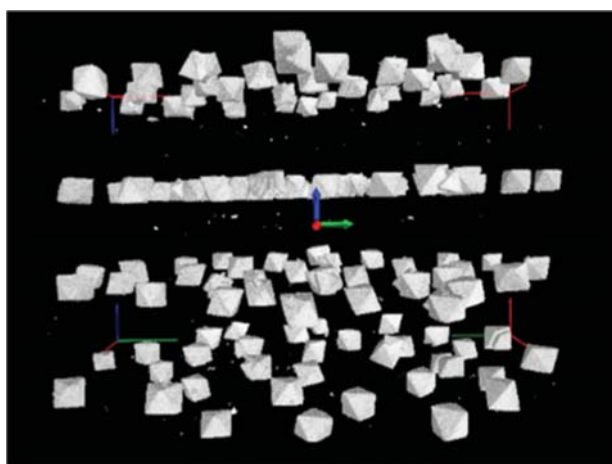


**Figure 6.** Rendered 3D image of 128 PA crystals after binarization. For this image, four  $2 \times 2 \times 2$  mm<sup>3</sup> scaffolds had been stacked.

this contribution. To determine the microscopic surface area of the crystals, the surface of the crystals was triangulated using Matlab's isosurface function. The sum of the areas of all triangles could then be used as the surface area. However, because of the description of the crystals through discrete voxels, the surfaces are not flat. They have steps that make the surfaces appear rough (Figure 10). This roughness is also initially contained in the triangulation. Hence, the surface area would be measured too high. Therefore, the triangulation was smoothed according to Desbrun et al.<sup>32</sup> using the smoothpatch library obtained from Matlab's central file exchange.<sup>33</sup> The smoothing was applied three times. This procedure was validated by determining the surface areas of the first 10 crystals obtained from the first and last samples using the commercial 3D image analysis software Modular Algorithms for Volume Images (MAVI, Fraunhofer Institute for Industrial Mathematics, Germany<sup>34</sup>). The first sample contained mostly small crystals, whereas the last sample contained the largest crystals. The mean relative deviation between the surface areas obtained using MAVI and those obtained using the smoothing method was 1% for the subset.

**2.6. Geometric Crystal Models.** A more detailed analysis of the crystals is enabled by the tools described by Kovačević et al.<sup>21–23</sup> A comprehensive summary of this work is provided by Schiele et al.<sup>24</sup> The method uses H-representations to describe the geometry of each crystal. In the case of crystal agglomerates, an H-representation is found for each primary crystal of the agglomerate. H-representations consist of a matrix  $\mathbf{A}$  and a vector  $\mathbf{h}$ .  $\mathbf{A}$  is a set of vectors that describe the direction of the face normals. In principle, PA crystals could express faces with the Miller indices [111], [100], and [110].<sup>35</sup> However, in the measurements presented here, only [111] faces were observed. Hence,  $\mathbf{A}$  consists of eight vectors that describe the eight [111] faces. Kovačević et al.<sup>22</sup> show how the orientation of a crystal is described by applying a rotation matrix to  $\mathbf{A}$ . To describe the size and shape of a crystal,  $\mathbf{h}$  is used. It describes the distance of each face to a reference point. An example of a 2D H-representation is shown in Figure 7.  $\Phi_n$  is a shape factor that is defined according to eq 3.

$$\Phi_n = \frac{\mathbf{h}}{\|\mathbf{h}\|_{\max}} \quad (3)$$

To describe agglomerates, Kovačević et al.<sup>23</sup> described how user interactions can be used to improve the segmentation of agglomerates into primary crystals. However, because of the large number of crystals that were analyzed in the context of this work, manual interaction became infeasible. Therefore, the interaction modules were removed from the program, and the initial conditions of the interaction modules were used. This may result in oversegmentation (e.g., a single crystal is separated into several parts) or undersegmentation (an agglomerate is not separated into correct primary

Expressed faces defined by

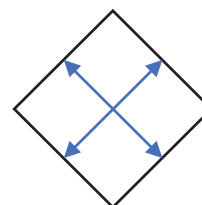
$$\mathbf{A} = 1/\sqrt{2} \begin{pmatrix} 1 & 1 \\ 1 & -1 \\ -1 & -1 \\ -1 & 1 \end{pmatrix}$$

Shape defined by

$$\mathcal{H} = \mathbf{A} \cdot \mathbf{h}$$

Ideal Shape

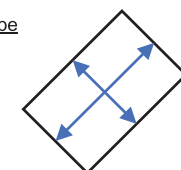
$$\mathcal{H} = \mathbf{A} \cdot \begin{pmatrix} 2 \\ 2 \\ 2 \\ 2 \end{pmatrix}$$



$$\Phi_n = \begin{pmatrix} 1 \\ 1 \\ 1 \\ 1 \end{pmatrix}$$

Non-Ideal Shape

$$\mathcal{H} = \mathbf{A} \cdot \begin{pmatrix} 2 \\ 1 \\ 2 \\ 1 \end{pmatrix}$$



$$\Phi_n = \begin{pmatrix} 1 \\ 0.5 \\ 1 \\ 0.5 \end{pmatrix}$$

**Figure 7.** Illustration of the geometric crystal representation in 2D for ideal and nonideal shapes.

particles). It is very likely that for such badly separated particles, fitting is not successful. Therefore, the number of successful fits is expected to be lower compared to a procedure that includes user interaction.

**2.7. Modeling Crystal Growth.** A crystal growth model is used to interpret the experimentally observed shape evolution of crystals through face-independent growth (Section 3.2). The model considers the evolution of experimental sets of crystals that are characterized by H-representations, as explained in Section 2.6. The 30 min sample is used as the initial set because the fit accuracy for the 0 min sample was insufficient (only 34 successful fits). We consider the index  $i$  to represent the different sampling time points  $t_i$  from  $\mathbf{t} = (30 \text{ min}, 60 \text{ min}, 90 \text{ min}, 120 \text{ min}, 150 \text{ min})$ . From the sets of H-representations, volumes are calculated according to Kovačević and Briesen.<sup>30</sup> Using these volumes, normalized number distributions with respect to volume with 25 classes are created. These distributions are represented by discrete vectors  $\mathbf{q}_{0,\text{exp},i}$ . All matrices  $\mathbf{A}$  of the H-representations only differ in rotation and rotation has no influence on volume. Therefore, an experimental normalized number distribution with respect to volume can be calculated for any set of face distance vectors  $\mathbf{h}$  (i.e., at all sampling times  $t_i$ ,  $\mathbf{q}_{0,\text{exp},i} = f_{\mathbf{h} \rightarrow \nu}(\mathbf{h}_i)$ ). The resulting distributions are similar to those shown in Figure 9 because a low deviation of volume is considered as a quality criterion in the fitting algorithm.<sup>22</sup> However, in the context of this growth model, the distributions that are calculated from the H-representations are used to ensure overall model consistency.

The growth of the sampled crystals at  $t_1 = 30$  min is modeled by increasing all of the entries in  $\mathbf{h}$  of its H-representations by the same  $\Delta h_i$  (time-dependent but face-independent growth). Thus,  $\Delta h_i$  is used to increase the size and hence the volume of the crystals. Using different  $\Delta h_i$  for different time steps results in differently sized crystal populations at the time points  $t_i$ . The number density distribution resulting from the model can be formulated as a function of the initial 30 min  $\mathbf{h}_1$  and the respective  $\Delta h_i$ .

$$\mathbf{q}_{0,\text{mod},i} = f_{\mathbf{h} \rightarrow \nu}(\mathbf{h}_1 + \Delta h_i) \quad (4)$$

As the crystals sampled at the different time points are obviously not the same ones, the determination of reasonable  $\Delta h_i$  is not trivial. We chose to demand consistency with the overall volume evolution instead of evolution of individual crystals. To achieve this,  $\Delta h_i$  are chosen such that the distance between the distributions of the numerically grown sample  $\mathbf{q}_{0,\text{mod},i}$  and those of the actually measured sample at the corresponding time point  $\mathbf{q}_{0,\text{exp},i}$  becomes minimal. The minimization problem formulated in eq 5 is solved using the simplex method<sup>36</sup> (Matlab's `fminsearch` function).

$$\min_{\Delta h_i} \|\mathbf{q}_{0,\text{mod},i} - \mathbf{q}_{0,\text{exp},i}\|_2 \quad (5)$$

The optimization is done separately for all  $i \in \{2,3,4,5\}$ . Results are shown and discussed in Section 3.2.

### 3. RESULTS AND DISCUSSION

The crystallization conditions during the process are summarized in Figure 8. The figure shows the linear

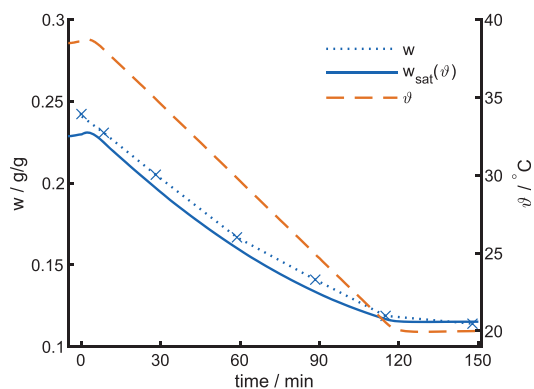


**Figure 8.** Course of temperature (orange dashed line) during the crystallization experiment. The course of the saturation concentration (blue solid line) results from the course of the temperature. The measured concentrations are displayed as crosses that are connected by dotted lines. Seeds were added at 0 min.

temperature profile (orange dashed line), the corresponding saturation concentration as calculated from eq 1 (solid blue line), and the measured concentrations (crosses–dotted line).

This shows that a slight supersaturation was maintained while temperature was decreased. The supersaturation profile is shown in Sup. 8. Once 20 °C was reached, the concentration quickly approached saturation. Hence, no crystal growth should be expected after 150 min.

**3.1. Volume and Surface Area Distributions.** To obtain both the surface area and the volume of the crystals, DIA (Appendix III) and the proposed  $\mu$ CT method were applied. The crystal samples were first analyzed by  $\mu$ CT and subsequently by DIA. During the experiment, inline FBRM measurements were performed to determine the state of full dissolution. DIA yields 2D projections of particles, and 3D images of particles are obtained by  $\mu$ CT. The most detailed information on the volume and the surface area of the crystals can be extracted from 3D images (Section 2.5). The normalized number density distributions with respect to volume as measured by  $\mu$ CT are shown in the top row of Figure 9. The corresponding distributions with respect to surface areas are shown in the bottom row of Figure 9. Note that at this point no geometric model was necessary to determine these distributions.

In both cases, the seed crystal distribution (0 min) is narrow. Over time, volumes and surface areas of the crystals increased. The distributions became wider. Only little change of the distributions between 120 and 150 min was observed. This is in accordance with the small change in concentration within this time window (Figure 8). Generally, the increase in volume and surface area is due to the growth of the crystals. These results are compared to those obtained by DIA in Appendix III in the Supporting Information.

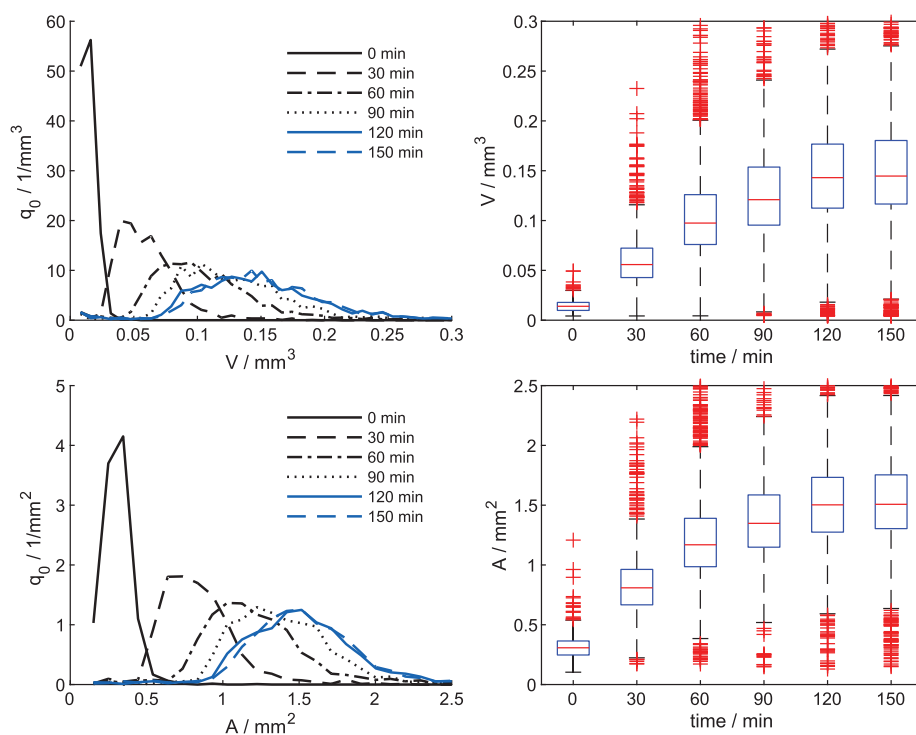


**Figure 9.** Normalized number density distributions with respect to volume (top left) and surface area (bottom left) as determined by  $\mu$ CT and the corresponding box-plots (right column). Boxes indicate the 25th and 75th percentile and median. Outliers are shown as red crosses. Whiskers cover approximately 99% of the data points.

A more detailed understanding of the crystal population evolution can be obtained by the following detailed shape analysis.

**3.2. Shape Analysis.** As discussed in the Introduction section, the shape of crystals is an important quality criterion and process parameter. At the same time, crystal shape is very hard to describe using established analysis methods. The 3D images obtained by  $\mu$ CT, however, contain full shape information. The method described by Kovačević et al.<sup>23</sup> was used to fit geometric models of crystals to  $\mu$ CT data with some adjustments as described in the Materials and Methods section. These geometric models are herein used for a detailed shape analysis.

Six exemplary crystals obtained from the proposed  $\mu$ CT method are shown in Figure 10. The left column shows the raw 3D images as obtained by  $\mu$ CT, the middle column shows the corresponding geometric crystal models that were fitted to the 3D images, and the right column shows a combination of both.

The number of crystals per sample and the corresponding number of successful fits to single crystals and agglomerates are

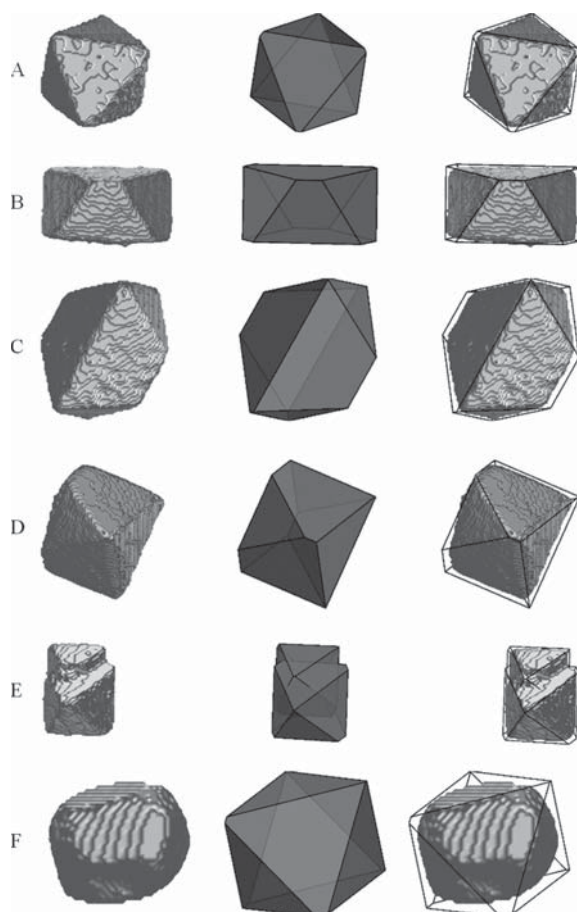


**Figure 10.** Examples of crystals that were analyzed. The left column shows the raw 3D images as obtained by  $\mu$ CT, the middle column shows a geometric crystal model that was fitted, and the right column shows a combination of both. (A) A well-fitted single crystal that has an almost ideal octahedral shape, (B) a well-fitted single crystal that has a flattened shape, (C) a well-fitted crystal with an elongated shape, (D) a well-fitted crystal with irregular shape, (E) a well-fitted agglomerate, and (F) a seed crystal that shows signs of breakage and abrasion, and the fit was classified as a bad fit.

summarized in Table 1. About 85% of all crystals of each sample were successfully fitted with the exception of the seed

**Table 1. Summary of the Number of Crystals Analyzed by  $\mu$ CT per Sample**

sample time/min	0	30	60	90	120	150
number of crystals	1296	1696	2593	1300	1866	2758
number of fitted single crystals	34 <sup>a</sup>	1272	1861	970	1379	2028
number of fitted agglomerates	3 <sup>a</sup>	240	309	164	237	297

<sup>a</sup>Low number of successful fits is due to nonideal shapes.

crystals where only 3% of the fits were successful (34 crystals). The low success rate for the seed crystals is caused by the highly nonideal, nonfaceted shape of these crystals. A larger part of the seed material showed signs of abrasion and breakage. Although in many cases, faces were identified and potential fits were found, the quality constraints were not met (Figure 10F). Out of the successful fits of the other samples, about 85% were detected as single crystals (Figure 10A–D) and 15% were agglomerates of two primary crystals (Figure 10E). Less than 1% of the particles were agglomerates that had more than two primary crystals. It is interesting to see that these percentages remained constant throughout the experiment. This suggests that formation of agglomerates only occurred before 30 min.

We have discussed before<sup>21,30</sup> that nonidealities can be introduced by agglomerates. The analysis of the agglomerates corroborates our previous results<sup>23</sup> with higher statistical significance and is shown in Appendix IV. Moreover, the shape of single crystals may deviate from an ideal shape. It is quite common to assume ideal crystal shapes for modeling and other calculations. In the case of PA, an octahedral shape is often assumed (Figure 10A, here forth considered as the ideal shape). When described by an H-representation, all entries in  $\mathbf{h}$  would then be the same. In the following, we study the shape of single crystals and ignore agglomerates.

To evaluate how effectively the crystals of our crystallization process are represented by this idealized shape (i.e., perfect octahedron), the aspect ratio  $\Phi_n$  within the  $\mathbf{h}$ -vector of each individual crystal was calculated (section 2.6,  $\Phi_n = \mathbf{h}/\|\mathbf{h}\|_{\max}$ ). In an ideal octahedron, all entries in  $\Phi_n$  would be 1. Nonideal crystals would have some entries in  $\Phi_n$  that are smaller than 1. The number density distributions of all entries of  $\Phi_n$  are shown in Figure 11. It can be seen that there are lots of nonideal faces and that the faces become more ideal over time (distribution shifts toward  $\Phi_n$  of 1).

2D examples of an ideal and nonideal shape are shown in Figure 7. This figure also illustrates that because the center of a crystal is used as the origin of  $\mathbf{A}$ , opposing faces have the same entries in  $\mathbf{h}$  and  $\Phi_n$ . In the geometric models of real measured crystals, there may be some opposing faces with different face distances due to inaccuracies in the  $\mu$ CT measurements and fitting of the models. We define four different types of 3D shapes for PA (Figure 12):

1. an ideal octahedron in which all entries in  $\Phi_n$  are close to 1; for example: Figure 10A with  $\Phi_n = (0.92, 1, 1, 0.99, 0.97, 0.97, 0.97, 0.94)$ ,<sup>1</sup>
2. a flattened shape in which six entries in  $\Phi_n$  are close to 1; for example: Figure 10B with  $\Phi_n = (0.57, 0.92, 1, 0.89, 0.85, 0.95, 0.88, 0.58)$ ,

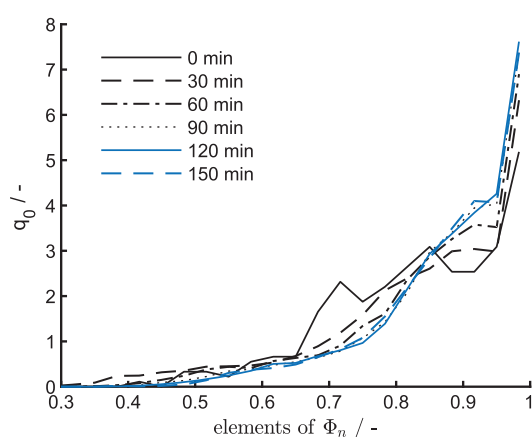


**Figure 11.** Normalized number density distribution of the aspect ratios in single crystals. Note that due to the nonideal shape of the seed material (0 min), only 34 crystals (corresponding to 272 entries in  $\Phi_n$ ) were successfully fitted. This is opposed to at least 970 successful fits (7760 entries in  $\Phi_n$ ) for the other samples. Therefore, the statistical relevance of the distribution of the seed material is much lower.

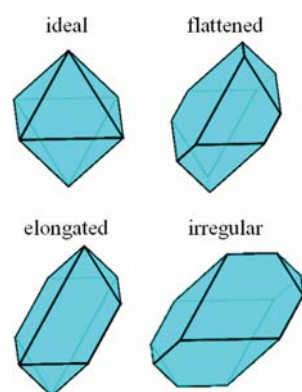


**Figure 12.** Four different types of shapes that were observed in the data set. In the nonideal shapes, all non-1 entries in  $\Phi_n$  were chosen to be 0.5 for illustration. Examples of real crystals of such shapes are shown in Figure 10.

3. an elongated shape in which four entries in  $\Phi_n$  are close to 1; for example: Figure 10C with  $\Phi_n = (0.67, 0.97, 1, 0.58, 0.57, 0.96, 0.93, 0.69)$ ,
4. and an irregular shape in which only two entries in  $\Phi_n$  are close to 1; for example: Figure 10D with  $\Phi_n = (0.60, 1, 0.87, 0.89, 0.75, 0.74, 0.82, 0.67)$ .

In the context of this work, 0.85 was chosen as the threshold to define what is considered “close to 1”. The threshold was applied to the mean face distance of two opposing faces. The four types of shapes are illustrated in Figure 12.

The fractions of crystals of different shapes in the samples are shown in Figure 13 as black lines. Note that the number of successful fits in the seed population was too small for this shape analysis. Therefore, only data from 30 min and later is shown in Figure 13. Error bars result from a similar bootstrap approach as explained in Section 2.3 and indicate 95% confidence. Details are explained in Appendix V. It can be seen that at 30 min, the fraction of elongated and irregular crystals is 33 and 28%, respectively. In addition, 17% of the crystals are ideal octahedrons and 22% are flattened. As the

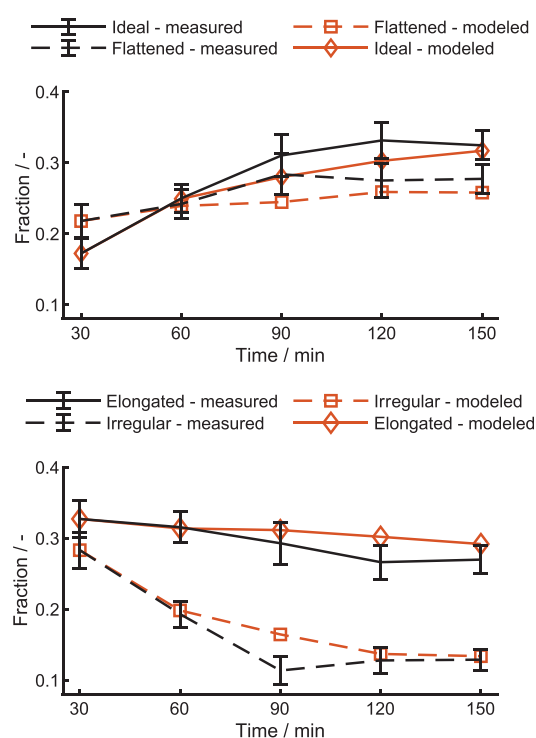


**Figure 13.** Fraction of crystals of different shapes over time. Error bars indicate 95% confidence.

experiment proceeds, the crystals become less elongated and less irregular but more ideal and flattened. While particle shape change is usually attributed to face-dependent growth rates, the observed results here can be explained by face-independent crystal growth: as growth proceeds, the absolute difference in face distances remains constant. However, the relative difference decreases because the face distances increase. This relative difference is expressed in  $\Phi_n$ . Hence, as growth proceeds, face distances become more ideal. In an irregular crystal, three pairs of face distances are nonideal. If such a crystal grows, the two longest nonideal face distances become ideal; the crystal is then classified as an elongated crystal. If this crystal grows even further, again, its two longest nonideal face distances become ideal. Thus, the crystal’s shape is classified as flattened. This continues until all crystals have an ideal shape or growth stops. The model shown below provides strong indication that this mechanism based on face-independent growth is the cause of the observed change of shape toward ideal crystals. After 120 min, only little growth occurs. Accordingly, little change in the shapes is observed. An animation of this growth behavior is provided in the Supporting Information.

To assess this growth behavior, the growth of the crystals starting from the 30 min sample is modeled (Figure 13 orange lines, according to Section 2.7). This is done by increasing the  $h$ -vectors of the 30 min sample by time-variant face displacements  $\Delta h_i$ , until the corresponding volume distribution resembles that of a sample at a later time point. Details on the numerical procedure are given in Section 2.7. The  $H$ -representations of the 30 min sample were grown by  $\Delta h_i \in \{40.4, 55.7, 72.0, 76.8\} \mu\text{m}$  to, respectively, reach the volume distributions at  $t_i \in \{60, 90, 120, 150\}$  min. For most times, the results of the model lie within the error bars. This indicates

that the observed shape-shifting process is due to face-independent crystal growth. This discards an alternative explanation where the face-dependent growth could govern shape-shifting based on, e.g., different surface energies originating from mechanical damage like abrasion of the different faces.

Ideal crystal shapes may be preferable during production (e.g., for easier solid–liquid separation). Using the same model, it can be estimated as to how much the crystals of the 30 min sample would need to grow until most crystals have reached ideal shapes. To do this, the H-representations of the 30 min sample are grown until 90% of its crystals have ideal shapes. The results of this simulation are shown in Figure 14,

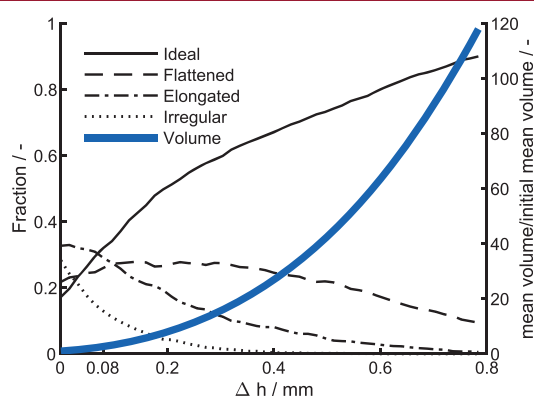


**Figure 14.** Modeled growth of the 30 min sample. Thin black lines show the fraction of crystals of different shapes with respect to the absolute face displacement  $\Delta h$ . The thick blue line indicates the resulting relative increase in volume. The region between 0 and 0.08 mm is the region that is displayed in Figure 13 and relevant for the herein analyzed process.

which shows the fractions of crystals over face displacement and the corresponding relative increase in volume. To produce a population of 90% ideal crystals, the crystals need to grow by 0.8 mm. This corresponds to an increase in volume by a factor of roughly 120. This illustrates that on the one hand, ideal crystal growth leads to more ideal shapes. However, on the other hand, shape-shifting requires the crystals to grow to a high manifold of their volume. From a process point of view, nonideal shapes of very small crystals (e.g., nuclei) can become ideal through ideal crystal growth. Larger seed crystals with nonideal shapes or crystals resulting from breakage or agglomeration events hardly assume a fully ideal shape.

The disadvantage of the  $\mu$ CT method is that it can only be used as an offline technique; hence, sampling is a crucial and complicated step. However, sampling is also complicated for any other nonlinear technique. Currently, the greatest disadvantage of  $\mu$ CT measurements is the highly work-intensive sample preparation. As described in the Materials and Methods section, each of the 11 000 crystals was individually sorted into a measurement scaffold. Along with the sorting problem comes the challenge that the particles need a certain size to be handled by tweezers. Here, the minimum particle size investigated was 200  $\mu\text{m}$ . All smaller particles had to be discarded. Great care must be taken to avoid damaging the particles in the sorting process. Further, the 3D image analysis tool described by Kovačević et al.<sup>23</sup> is highly hardware-demanding. Only fitting of the crystals analyzed in the context of this work took roughly 1 week on a standard desktop

computer (6 CPU kernels working at 3.2 GHz, 16 GB memory). The segmentation of individual crystals (see Section 2.4) took overall about 1 day on a server-computer (6 CPU kernels working at 3.7 GHz each, 128 GB memory).

On the other hand,  $\mu$ CT provides the potential of a very detailed analysis of convex and concave particles. This potential was only illustrated here by the application to a specific crystallization process. The viability of particle population analysis by  $\mu$ CT in general was demonstrated by the visualization of 11 000 individual particles and a subsequent 3D shape analysis.

#### 4. CONCLUSIONS

A method for 3D particle population analysis using  $\mu$ CT was proposed and applied to samples of a crystallization process. The samples were retrieved at several time points during an exemplary seeded cooling crystallization of PA. The sampling was optimized to yield samples that were able to represent particle populations as measured by DIA.

For the  $\mu$ CT analysis, sampled crystals were sorted into scaffolds that ensured that the crystals were not in close contact with each other but at the same time allowed up to 786 crystals to be included in each 3D image at a voxel spacing of 8  $\mu\text{m}$ . Overall, 11 000 crystals were visualized and subsequently analyzed. The binarization of the images was done in a way that the mass of the crystals was conserved. It was discussed that the method yielded accurate results of the volume and the microscopic surface area without the need for geometric crystal models.

Furthermore, 3D image analysis allowed a more detailed analysis of the crystals. The focus of our present work was the analysis of single crystals. Single crystals were classified into four different shape categories according to the aspect ratios of their faces that were calculated from their geometric models. It became apparent that many crystals had nonideal shapes. It was further interesting to see that the shapes of the crystals somehow approached an ideal shape over time. Such changes in shape are often attributed to face-dependent growth. To evaluate this behavior, the growth of the crystals was modeled. The simulation showed that indeed face-independent crystal growth led to the observed shape-shifting effect for the crystals in our data set. Through growth, relative differences in face distances become smaller and hence the crystals in our data set appeared more ideal. The growth model also demonstrated that fully ideal shapes can only be expected for very small crystals (e.g., nuclei). The larger crystals of our data set would need to grow to a manifold of their volume to become ideal.

In summary,  $\mu$ CT is a viable method for particle population analysis. Together with appropriate image analysis techniques, it enables detailed shape analysis of crystals. Here, the effect of ideal crystal growth on crystal shape was studied. In future work, we aim to further apply this technique to gain deeper insight into the morphological changes during crystallization processes.

#### ■ ASSOCIATED CONTENT

##### Supporting Information

The Supporting Information is available free of charge at <https://pubs.acs.org/doi/10.1021/acs.cgd.0c01644>.

3D nature of our  $\mu$ CT measurements (MPG)

Illustrates how crystals approach an ideal shape through face-independent growth; left panel shows a crystal and

the corresponding vector  $\mathbf{h}$  containing the face distances; face-independent growth is applied to this vector; only four entries of  $\mathbf{h}$  are shown because opposing faces have the same face distances; and right panel contains a normalized version (according to eq 3) of the same crystal and illustrates the evolution of shape through face-independent growth (MPG)

Appendix I explains how the rotational speed of the stirrer was chosen; Appendix II explains the binarization method, including eq S1; Appendix III compares the volume and surface area as obtained from DIA and  $\mu$ CT; Appendix IV deals with the disorientation angles in agglomerates; Appendix V explains how the error bars of Figure 13 are estimated; and Appendix VI contains additional figures (PDF)

## AUTHOR INFORMATION

### Corresponding Author

**Heiko Briesen** – Chair of Process Systems Engineering, Technical University of Munich, 85354 Freising, Germany; [orcid.org/0000-0001-7725-5907](https://orcid.org/0000-0001-7725-5907); Phone: +498161715383; Email: [heiko.briesen@mytum.de](mailto:heiko.briesen@mytum.de); Fax: +498161714510

### Authors

**Simon A. Schiele** – Chair of Process Systems Engineering, Technical University of Munich, 85354 Freising, Germany; [orcid.org/0000-0003-3026-2768](https://orcid.org/0000-0003-3026-2768)

**Felix Antoni** – Chair of Process Systems Engineering, Technical University of Munich, 85354 Freising, Germany

**Rolf Meinhardt** – Chair of Process Systems Engineering, Technical University of Munich, 85354 Freising, Germany

Complete contact information is available at: <https://pubs.acs.org/10.1021/acs.cgd.0c01644>

### Notes

The authors declare no competing financial interest.

## ACKNOWLEDGMENTS

The authors (S.A.S. and H.B.) are grateful for the support of Deutsche Forschungsgemeinschaft (DFG) through the Priority Program SPP 1679, Dynamic Simulation of Coupled Solids Processes, project number 238696028. The OptiMax Synthesis workstation was funded by the DFG through grant 263666176 and the  $\mu$ CT through grant 198187031. The authors thank Michaela Thalhammer for her persistent support with the  $\mu$ CT measurements and in the laboratory and Dr. Markus Gütlich and Martin Ortner for making this work possible through their great commitment for the maker space at our campus and their help with the 3D printing. Further, we thank Dr. Hannes Petermeier for the fruitful discussion on the statistics and Dr. Cornelia Eder for taking her time for the frequent discussions on crystallization.

## GLOSSARY

$\mathbf{A}$ (–)	matrix with face normals for H-representation
$A$ (mm <sup>2</sup> )	surface area
$d_{\text{EQPC}}$ (mm)	diameter of a circle with equal projected area
$\mathbf{h}, h_i$ (–)	histogram vector of an image, its elements

$\mathbf{h}, h_i$ (mm)	vector of the face distances of a crystal (at a time $t_i$ )
$H$ (–)	H-representation of a crystal
$m$ (kg)	mass
$\mathbf{q}_{0,\text{exp},i}, \mathbf{q}_{0,\text{mod},i}$ (mm <sup>–3</sup> )	discrete vector of experimentally determined (index exp) and modeled (index mod) normalized number distribution with respect to volume at time point $t_i$
res ( $\mu\text{m}/\text{voxel}$ )	resolution of the $\mu$ CT measurements
$\mathbf{t}$ (min)	vector of sampling times
$t_i$ (min)	sampling points
$T$ (–)	threshold for binarization
$T$ (K)	temperature in Kelvin
$V$ (mm <sup>3</sup> )	volume
$w, w_{\text{sat}}$ (g/g)	load, saturation load
$\Delta h_i$ ( $\mu\text{m}$ )	change of $\mathbf{h}$ within a time $t_i$
$\Delta x$ ( $\mu\text{m}$ )	class size
$\rho$ (g/cm <sup>3</sup> )	density of potash alum ( $\rho = 1.75$ g/cm <sup>3</sup> )
$\vartheta$ (°C)	temperature
$\Phi_n$ (mm)	shape factor according to eq 3

## ABBREVIATIONS

1D, one-dimensional; 2D, two-dimensional; 3D, three-dimensional; CAD, computer-aided design; DIA, dynamic image analysis; FBRM, focused beam reflectance measurements; MAVI, Modular Algorithms for Volume Images; PA, potash alum; PVM, particle vision and measurement;  $\mu$ CT, micro-computed tomography

## ADDITIONAL NOTE

<sup>1</sup>Entries in  $\Phi_n$  correspond to opposing faces in the following scheme: (a b c d d c b a).

## REFERENCES

- (1) Viankaval, N.; Cote, A. S.; Doherty, M. F. From form to function: Crystallization of active pharmaceutical ingredients. *AIChE J.* **2008**, *54*, 1682–1688.
- (2) Beck, R.; Häkkinen, A.; Malthe-Sørensen, D.; Andreassen, J.-P. The effect of crystallization conditions, crystal morphology and size on pressure filtration of l-glutamic acid and an aromatic amine. *Sep. Purif. Technol.* **2009**, *66*, 549–558.
- (3) Dandekar, P.; Kuvadia, Z. B.; Doherty, M. F. Engineering Crystal Morphology. *Annu. Rev. Mater. Res.* **2013**, *43*, 359–386.
- (4) Blagden, N.; de Matas, M.; Gavan, P. T.; York, P. Crystal engineering of active pharmaceutical ingredients to improve solubility and dissolution rates. *Adv. Drug Delivery Rev.* **2007**, *59*, 617–630.
- (5) Xia, Y.; Xiong, Y.; Lim, B.; Skrabalak, S. E. Shape-controlled synthesis of metal nanocrystals: simple chemistry meets complex physics? *Angew. Chem., Int. Ed.* **2009**, *48*, 60–103.
- (6) Simon, L. L.; Pataki, H.; Marosi, G.; Meemken, F.; Hungerbühler, K.; Baiker, A.; Tummala, S.; Glennon, B.; Kuentz, M.; Steele, G.; Kramer, H. J. M.; Rydzak, J. W.; Chen, Z.; Morris, J.; Kjell, F.; Singh, R.; Gani, R.; Gernaey, K. V.; Louhi-Kultanen, M.; O'Reilly, J.; Sandler, N.; Antikainen, O.; Yliruusi, J.; Froberg, P.; Ulrich, J.; Braatz, R. D.; Leyssens, T.; von Stosch, M.; Oliveira, R.; Tan, R. B. H.; Wu, H.; Khan, M.; O'Grady, D.; Pandey, A.; Westra, R.; Delle-Case, E.; Pape, D.; Angelosante, D.; Maret, Y.; Steiger, O.; Lenner, M.; Abbou-Oucherif, K.; Nagy, Z. K.; Litster, J. D.; Kamaraju, V. K.; Chiu, M.-S. Assessment of Recent Process Analytical Technology (PAT) Trends: A Multiauthor Review. *Org. Process Res. Dev.* **2015**, *19*, 3–62.

- (7) Lovette, M. A.; Browning, A. R.; Griffin, D. W.; Sizemore, J. P.; Snyder, R. C.; Doherty, M. F. Crystal Shape Engineering. *Ind. Eng. Chem. Res.* **2008**, *47*, 9812–9833.
- (8) Ruf, A.; Worlitschek, J.; Mazzotti, M. Modeling and Experimental Analysis of PSD Measurements through FBRM. *Part. Part. Syst. Charact.* **2000**, *17*, 167–179.
- (9) Heath, A. R.; Fawell, P. D.; Bahri, P. A.; Swift, J. D. Estimating Average Particle Size by Focused Beam Reflectance Measurement (FBRM). *Part. Part. Syst. Charact.* **2002**, *19*, 84–95.
- (10) Kail, N.; Briesen, H.; Marquardt, W. Advanced Geometrical Modeling of Focused Beam Reflectance Measurements (FBRM). *Part. Part. Syst. Charact.* **2007**, *24*, 184–192.
- (11) Li, H.; Kawajiri, Y.; Grover, M. A.; Rousseau, R. W. Application of an Empirical FBRM Model to Estimate Crystal Size Distributions in Batch Crystallization. *Cryst. Growth Des.* **2014**, *14*, 607–616.
- (12) Barthe, S. C.; Grover, M. A.; Rousseau, R. W. Observation of Polymorphic Change through Analysis of FBRM Data: Transformation of Paracetamol from Form II to Form I. *Cryst. Growth Des.* **2008**, *8*, 3316–3322.
- (13) Wirz, D.; Hofmann, M.; Lorenz, H.; Bart, H.-J.; Seidel-Morgenstern, A.; Temmel, E. A Novel Shadowgraphic Inline Measurement Technique for Image-Based Crystal Size Distribution Analysis. *Crystals* **2020**, *10*, No. 740.
- (14) Kiernan, L.; Jones, I.; Kurki, L.; Cullen, P. J.; El Arnaout, T. Adaptive Background Correction of Crystal Image Datasets: Towards Automated Process Control. *Sens. Imaging* **2020**, *21*, No. 821.
- (15) Borchert, C.; Sundmacher, K. Morphology evolution of crystal populations: Modeling and observation analysis. *Chem. Eng. Sci.* **2012**, *70*, 87–98.
- (16) Borchert, C.; Temmel, E.; Eisenschmidt, H.; Lorenz, H.; Seidel-Morgenstern, A.; Sundmacher, K. Image-Based in Situ Identification of Face Specific Crystal Growth Rates from Crystal Populations. *Cryst. Growth Des.* **2014**, *14*, 952–971.
- (17) Kempkes, M.; Eggers, J.; Mazzotti, M. Measurement of particle size and shape by FBRM and in situ microscopy. *Chem. Eng. Sci.* **2008**, *63*, 4656–4675.
- (18) Schorsch, S.; Ochsenbein, D. R.; Vetter, T.; Morari, M.; Mazzotti, M. High accuracy online measurement of multidimensional particle size distributions during crystallization. *Chem. Eng. Sci.* **2014**, *105*, 155–168.
- (19) Reinhold, A.; Schorsch, S.; Mazzotti, M.; Briesen, H. Modeling and measurement of abraded particles. *Powder Technol.* **2015**, *271*, 134–140.
- (20) Huo, Y.; Liu, T.; Yang, Y.; Ma, C. Y.; Wang, X. Z.; Ni, X. In Situ Measurement of 3D Crystal Size Distribution by Double-View Image Analysis with Case Study on L-Glutamic Acid Crystallization. *Ind. Eng. Chem. Res.* **2020**, *59*, 4646–4658.
- (21) Kovačević, T.; Schock, J.; Pfeiffer, F.; Briesen, H. Shape Identification of Primary Particles in Potash Alum Aggregates Using Three-Dimensional Tomography Data. *Cryst. Growth Des.* **2016**, *16*, 2685–2699.
- (22) Kovačević, T.; Reinhold, A.; Briesen, H. Identifying Faceted Crystal Shape from Three-Dimensional Tomography Data. *Cryst. Growth Des.* **2014**, *14*, 1666–1675.
- (23) Kovačević, T.; Wiedmeyer, V.; Schock, J.; Voigt, A.; Pfeiffer, F.; Sundmacher, K.; Briesen, H. Disorientation angle distribution of primary particles in potash alum aggregates. *J. Cryst. Growth* **2017**, *467*, 93–106.
- (24) Schiele, S.; Kovačević, T.; Briesen, H. Morphological Modelling and Simulation of Crystallization Processes. In *Dynamic Flowsheet Simulation of Solids Processes*, 1st ed.; Springer International Publishing, 2020; Vol. 1, pp 435–473.
- (25) Kuzmanić, N.; Kessler, E. M. Continuous Sampling of Floating Solids Suspension from a Mixing Tank. *Ind. Eng. Chem. Res.* **1997**, *36*, 5015–5022.
- (26) Ayazi Shamlou, P.; Koutsakos, E. Solids suspension and distribution in liquids under turbulent agitation. *Chem. Eng. Sci.* **1989**, *44*, 529–542.
- (27) Genck, W. J. Temperature Effects on Growth and Nucleation Rates in Mixed Suspension Crystallization. Retrospective Theses and Dissertations, Iowa State University, 1969.
- (28) Sha, Z.; Palosaari, S. Mixing and crystallization in suspensions. *Chem. Eng. Sci.* **2000**, *55*, 1797–1806.
- (29) Efron, B. Bootstrap Methods: Another Look at the Jackknife. *Ann. Statist.* **1979**, *7*, 1–26.
- (30) Kovačević, T.; Briesen, H. Simulations of crystal aggregation and growth: Towards correct crystal area. *AIChE J.* **2019**, *65*, No. e16525.
- (31) Dandekar, P.; Doherty, M. F. Materials science. Imaging crystallization. *Science* **2014**, *344*, 705–706.
- (32) Desbrun, M.; Meyer, M.; Schröder, P.; Barr, A. H. In *Implicit Fairing of Irregular Meshes using Diffusion and Curvature Flow*, SIGGRAPH '99: Proceedings of the 26th Annual Conference on Computer Graphics and Interactive Techniques, 1999; pp 317–324.
- (33) Kroon, D.-J. Smooth Triangulated Mesh, 1.1.0.0., 2010. <https://de.mathworks.com/matlabcentral/fileexchange/26710-smooth-triangulated-mesh>. Matlab Central File Exchange.
- (34) Ohser, J.; Nagel, W.; Schladitz, K. Miles Formulae for Boolean Models Observed on Lattices. *Image Anal. Stereol.* **2009**, *28*, No. 77.
- (35) Ma, C. Y.; Wan, J.; Wang, X. Z. Faceted growth rate estimation of potash alum crystals grown from solution in a hot-stage reactor. *Powder Technol.* **2012**, *227*, 96–103.
- (36) Lagarias, J. C.; Reeds, J. A.; Wright, M. H.; Wright, P. E. Convergence Properties of the Nelder–Mead Simplex Method in Low Dimensions. *SIAM J. Optim.* **1998**, *9*, 112–147.



## 5.2 Paper III: Growth of abraded crystals tracked in three dimensions (Schiele et al. 2021b)

### Summary

In the previously presented study (Schiele et al. 2021a), asymmetric crystals were observed but their existence could not be explained. The hypothesis was that their asymmetry was caused by damaged and asymmetric seed material. More generally, there is little literature on growth of damaged crystals even though e.g. abrasion is abundant in most crystallization processes. The goal of this study was, therefore, to better understand the growth of damaged crystals by studying growth of abraded potash alum crystals.

In a first step, a new 3D imaging method was established. Potash alum crystals were adhered to racks for growth and  $\mu$ CT imaging. After an initial 3D image was obtained the crystals were placed in supersaturated, agitated solution for growth. Agitation was fast enough to prevent diffusion limitation. Subsequently, the crystals were imaged again. Imaging/growth-cycles were repeated until the crystals appeared fully faceted. This yielded a series of 3D images of crystals during different states of their growth.

As a next step, a new image analysis method was developed that was used to determine the displacement of surface through growth in all directions. For 1200 directions corresponding growth rates were averaged and described using spherical harmonics functions. This analysis showed that the directions corresponding to the known crystal faces of potash alum grew at the slowest rates. In consequence, fast growing surface disappeared in favor of the known faces. The measurements were used to parametrize a growth model that is able to track the size and shape evolution of single abraded potash alum crystals through growth. The model was applied to seed crystals of the previous study (Schiele et al. 2021a) and simulations confirmed that asymmetric seeds grow to become faceted but remain asymmetric. Initially symmetric shapes remained symmetric. In conclusion, non-ideal crystal shape was shown to be an important process variable for growth-abrasion interaction and can be accurately tracked using  $\mu$ CT imaging.

### Author contributions

S. Schiele came up with the idea for this work and developed the experimental and image analysis methods, conducted experiments, the evaluation of all experiments, the modelling, and the simulations. R. Hupfer helped developing the experimental and image analysis methods and conducted experiments. S. Schiele supervised the work of R. Hupfer. F. Luxenburger conducted the BFDH calculations. H. Briesen supervised all work. The article was written by S. Schiele with help of F. Luxenburger (BFDH sections). H. Briesen and F. Luxenburger corrected and proofread the article.

### Copyright

The following section is reprinted with permission from (Schiele et al. 2021b). Copyright 2021 American Chemical Society.



## Growth of Abraded Crystals Tracked in Three Dimensions

Simon A. Schiele, Ricardo Hupfer, Frederik Luxenburger, and Heiko Briesen\*

Cite This: *Cryst. Growth Des.* 2021, 21, 6373–6384

Read Online

ACCESS |



Metrics &amp; More



Article Recommendations



Supporting Information

**ABSTRACT:** The interaction between crystal growth and abrasion is essential during crystallization. Although each of these phenomena has been independently studied in the literature in detail, their interaction is not well understood. Here, we present a method to track the growth of abraded potash alum crystals in three dimensions. The method is based on micro-computed tomography. This technique distinguishes between different growth domains in three dimensions and is used to track the growth of crystal faces and abraded regions. We observed how abraded regions grew faster than crystal faces. Therefore, growth leads to ideally faceted crystals. Further, growth rates in all directions were derived and used to parametrize a growth model. The model is able to describe the size and shape evolution of abraded potash alum crystals in three dimensions.

## 1. INTRODUCTION

Crystal size has long been known as an important variable in crystallization processes. More recently, the shape of crystals has attracted increasing attention. The shape of crystals is not only important to yield certain product features,<sup>1,2</sup> but it is also an important process parameter.<sup>3–7</sup> Crystal shape engineering<sup>4,8–10</sup> has emerged from the need to control the shape of crystals. Crystal shape is often described using a geometric characteristic, which is often a shape factor, such as aspect ratio.<sup>11–13</sup> There are also approaches in which another geometric measure, such as surface area, is used as a proxy for shape.<sup>14</sup> However, complex crystal shapes are usually not well described by such representations.

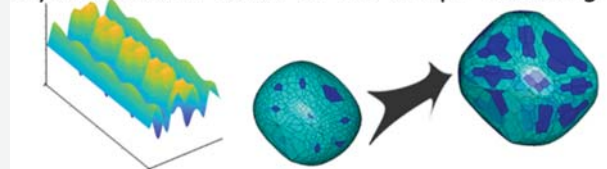
In the past decade, researchers have developed several methods to describe shapes of faceted crystals. For example, polygonal shape models were set up and parametrized using two-dimensional (2D),<sup>15–17</sup> stereoscopic,<sup>18,19</sup> or three-dimensional (3D)<sup>20,21</sup> imaging techniques. A common representation of such shape models is the H-representation.<sup>22</sup> Therein, each face of a crystal is described by a normal vector and a distance to a reference point. The reference point is often chosen as the center of mass of a crystal. It is also convenient to use H-representations to model crystallization processes<sup>3,4,23–27</sup> because growth occurs in the normal direction of the faces. Therefore, the growth of crystals can be described through an increase in the face distances that are used in H-representations. Such geometric models are well suited to describe ideally faceted crystals.

However, not only growth occurs during crystallization processes. Crystallizers are often agitated to suspend crystals and to equalize concentration and temperature gradients.

## 3D Images of Crystals...



## ...yield Growth Rates for 3D Shape Modeling



Agitation imposes mechanical stress on crystals, leading to attrition, abrasion, and breakage, which can result in nonideal crystal shapes.<sup>6,12,13</sup> We use the term attrition for damage events that are caused by the impact of crystals with reactor components, such as the stirrer. In contrast to breakage, the size of a crystal is largely preserved during attrition. Abrasion is similar to attrition. However, it is caused by crystal–crystal contacts.

Attrition,<sup>28–30</sup> abrasion,<sup>29–31</sup> and breakage<sup>12,13</sup> have been quite well studied individually. In most studies, damage events are only considered to reduce size. Additionally, it is often assumed that damaged crystals grow at the same rates as undamaged ones.<sup>30,31</sup> However, Ulrich et al. show that crystal fragments and abraded crystals grow at rates up to 90% higher than undamaged crystals if their growth is integration limited.<sup>32</sup> As the growth of crystal fragments and abraded crystals proceeds, their growth rates approach those of undamaged crystals. In these studies, crystal growth was described in terms of mass change, and face-specific growth was not considered. Briesen modeled the impact of crystal shape on attrition using population balance modeling.<sup>11</sup> In the model, damaged crystals were assumed to be cubes with cutoff corners. The growth of the resulting additional faces was modeled so that the shape was not affected by growth: it was only affected by attrition. Additionally,

Received: July 27, 2021

Revised: October 4, 2021

Published: October 18, 2021



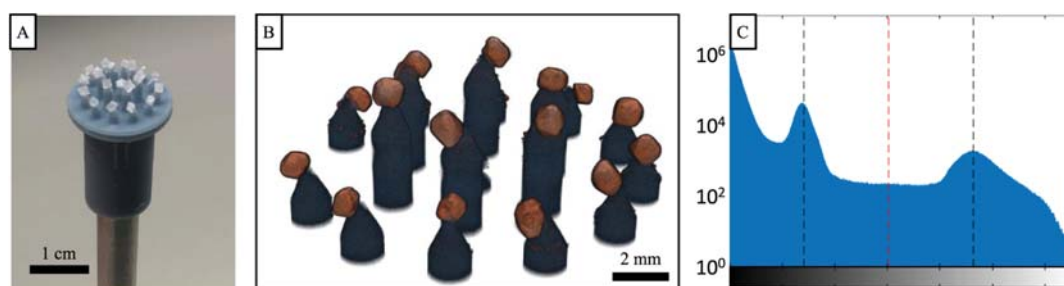


**Figure 1.** (A) Image of growth rack (blue) with adhered crystals and micro-computed tomography ( $\mu$ CT) sample holder. (B) Rendered three-dimensional (3D)  $\mu$ CT image of a rack with crystals after 17 min of growth with the background removed. (C) Brightness histogram of a raw 3D  $\mu$ CT image. The left dashed line marks the peak from the rack structure, the center dashed red line marks the binarization threshold that is used to extract the crystals, and the right dashed line marks the peak from the crystals.

Briesen did not use experimentally determined rates. More recently, Ma and Roberts<sup>26</sup> studied the effect of breakage on crystal shape and growth using a similar concept. They assumed that crystals would always break in the same direction. This assumption yielded the same basic morphology that was expressed as an additional face that would not be present in an undamaged crystal. The growth rate was assumed to be 2 times higher than that of an undamaged face. Ma and Roberts<sup>26</sup> emphasize that such a growth rate should be experimentally determined for their model to yield quantitative results. It is unknown whether a broken region would grow by face displacement.

As an alternative approach, phase-field modeling has been used to estimate the morphology of dissolving<sup>33</sup> or growing<sup>34</sup> 3D crystalline systems in silico. The underlying concept is to model energetic or kinetic anisotropies of interfaces using high-order Taylor polynomials.<sup>35</sup> Some parameters of these polynomials can be set to zero based on crystal symmetry, while values for others are derived from thermodynamic and geometric considerations. Notably, all appearing faces need to be known. Additionally, depending on what is modeled, the relative difference of the face-specific growth or dissolution rates are used as inputs. In summary, phase-field models require experimental data as inputs.

In a recent study,<sup>27</sup> we showed that asymmetric shapes of potash alum (PA) occurred during seeded batch cooling crystallization. This was surprising as PA crystals have a cubic unit cell, and the observed [111] faces should all grow at the same rates, leading to only symmetrical, octahedral crystals. Instead, we observed many flattened, elongated, and irregularly shaped crystals. We hypothesized that the nonideal shapes were introduced through damaged seed material that did not grow according to established growth laws.

In the present study, we aim to gain deeper insight into the growth of abraded PA crystals using micro-computed tomography ( $\mu$ CT) to track the growth of individual, abraded crystals. Volume images of the crystals are used to determine growth rates of abraded regions. The growth rates are used to parametrize a crystal growth model. The model is employed to simulate growth of abraded crystals under consideration of crystal size and shape. Modeled crystals are compared to experimentally crystallized ones.

## 2. MATERIALS AND METHODS

All concentrations are expressed as loads with the unit gram of PA hydrate per gram water.

**2.1. Materials.** Ethanol ( $\geq 99.8\%$ ), PA ( $\geq 99\%$  Ph. Eur.), and cellulose Rotilabo-round filters type 113A were purchased from Carl Roth GmbH + Co. KG (Germany). Ethanol was diluted with deionized water to obtain 50% ethanol solutions. Acetone ( $\geq 99.5\%$  Ph. Eur.) was purchased from Sigma-Aldrich Chemie GmbH (Germany).

**2.2. Reactor Setup.** An OptiMax 1001 reactor (Mettler Toledo Inc.) was used for all experiments. Temperature was controlled to  $\pm 0.1$  K. The reactor was equipped with a stirrer, with a diameter of 4.5 cm and four blades, which were pitched down. A focused beam reflectance method (FBRM) probe (Mettler Toledo Inc.) and a baffle were installed during the production of abraded crystals.

**2.3. Production of Abraded Crystals.** Abraded crystals were produced by sieving the bought PA (500–1000  $\mu\text{m}$ ). Then, 100 g of this material was suspended in 373 g of saturated PA solution at 40 °C. The saturation concentration was published previously.<sup>36</sup> Then, the stirrer was set to  $n = 1000$  rpm, and the solution was cooled to 20 °C within 2 h using a linear temperature profile. Then, a temperature of 20 °C and stirring at 1000 rpm was held for another 30 min. Subsequently, the suspension was filtered, washed with 50% ethanol solution and acetone, which are both antisolvents to PA, and finally dried using natural evaporation of the remaining solvents. Then, the crystals were sieved (500–1000  $\mu\text{m}$ ) to remove the fines. This procedure produced 104 g of abraded crystals.

The Reynolds number of the stirrer was estimated to be  $Re = \frac{n \cdot d^2 \cdot \rho}{\eta} \approx 10^4$  using the density of a PA solution at 20 °C ( $\rho = 1046 \text{ kg/m}^3$ ),  $d = 4.5 \times 10^{-2} \text{ m}$ ,  $n = 16.7 \frac{1}{s}$ , and the dynamic viscosity of water at 20 °C ( $\eta = 10^{-3} \text{ Pa s}$ ). The density of the PA solution was measured by producing a saturated PA solution at 20 °C and measuring its volume using a graduated cylinder. The same density can be calculated by neglecting excess volume. These conditions introduce high mechanical stress to the suspension. Stress is considered the primary cause of abrasion. Attrition may have also happened. However, limited damage to the crystals was observed in preliminary experiments at a lower solid concentration (results not shown), which indicates that abrasion was the dominating phenomenon here.

**2.4. Micro-Computed Tomography and Crystal Growth.** Three-dimensional images were acquired using a custom-built  $\mu$ CT system (XCT-1600HR; Matrix Technology AG, Germany). For each image, 1600 radiographic 2D projections were obtained. From these projections, 3D images were constructed using custom software (Matrix Technology, Germany), which is based on CERA software (Siemens AG, Germany). Images were acquired so that the voxel spacing was 8  $\mu\text{m}$ . The volume of one 3D image was  $16 \times 16 \times 10 \text{ mm}^3$  ( $2000 \times 2000 \times 1225 \text{ voxel}^3$ ), and the imaging procedure took 25 min per 3D image.

Two growth experiments were conducted: in the first run, 17 single abraded crystals were adhered to the tips of growth racks using super glue with a gel-like consistency (UHU Sekundenkleber Gel, UHU GmbH & Co. KG, Germany), and in the second run, 18 crystals were used. The relative size of crystals compared to the rack structure can be seen in Figure 1A,B. A sketch of a growth rack is shown in the

Supporting Information (Sup. 6), and an image of a rack with crystals is shown in Figure 1A. The crystals on the rack were visualized using  $\mu$ CT before growth. Then, the whole rack was submerged in a supersaturated PA solution (300 g water, 35.166 g PA,  $\Delta w = 2$  mg/g,  $\sigma = 0.0174$ ) at 20 °C close to the stirrer. The solution was stirred at 150 rpm, with a tip velocity of 0.35 m/s. Under these conditions, no diffusion limitation is expected for crystal growth below 11  $\mu\text{m}/\text{min}$ .<sup>37</sup> The highest growth rates measured in this study were  $\sim 5$   $\mu\text{m}/\text{min}$  (cf. Figure 12). After 1 min, the rack was removed from the reactor, washed with 50% ethanol, and dried by applying pressurized air. Subsequently, another  $\mu$ CT image was obtained. Such growth/imaging cycles were repeated until the crystals appeared to be fully faceted in the  $\mu$ CT images. The solution temperature in the reactor was ramped up to 25 °C, while  $\mu$ CT images were acquired to prevent nucleation. The saturation temperature at the concentration used was 20.7 °C. Supersaturation was assumed to be constant during the growth phases. This assumption was based on the 17 crystals adhering to the racks in the first run having an initial mass of 9.2 mg and a mass of 13.0 mg after growth. Volume was determined using  $\mu$ CT and a density of PA  $\rho_{\text{PA}} = 1750$  g/cm<sup>3</sup> was used. This corresponds to 3.8 mg of material that was crystallized and is approximately what can be expected as the accuracy of the scale used for weighing the reactor content with a resolution of  $\epsilon = 1$  mg. Additionally, the mass of PA solved was 600 mg above the solubility before growth started. Hence, the absolute supersaturation decreased by 0.63%, which corroborates our assumption of constant supersaturation. The washing procedure showed no significant effect on the volume of the crystals, which was validated by repeating the cycle of washing a sample and  $\mu$ CT imaging without growth 3 times and comparing the volumes of the crystals in the images.

**2.5. Basic Image Analysis.** The brightness histograms of the raw  $\mu$ CT images contained three peaks (Figure 1C): one peak contained dark gray and black voxels (background), another peak contained the rack structure in dark gray (left dashed line in Figure 1C), and the last peak contained the crystals in light gray (right dashed line in Figure 1C). Images of individual crystals were extracted from the raw  $\mu$ CT images by finding the individual peaks (Matlab's findpeaks function). A binarization threshold was then set in-between the second and third peaks (center dashed line in Figure 1C), yielding an image that only contained the crystals. An image that contained the rack structure was generated by binarization between the first and second peaks using Otsu's method (Matlab's imbinarize function).

The aim of the following image analysis steps is to overlay images of each crystal at its different states of growth to calculate the displacement of its surface through growth. To achieve this, a correction of the position and orientation of the crystals in each  $\mu$ CT image is necessary because it is impossible to reposition the sample holder at the exact same position for different  $\mu$ CT measurements. For finding the orientation and position of a growth rack in each  $\mu$ CT image, two reference points in the images were used. One point was a dent in the center pin of the rack (cf. Sup. 6), which provided the location of the center of the rack. The second reference point was the missing pin of the rack (cf. Sup. 6). Both points together provide a rotation around the rack's vertical axis. The  $\mu$ CT images were manually divided into images containing one crystal each, which were saved together with the center point of the rack and its rotation around the vertical axis. Using this information, the images of crystals at different time points could be overlaid. This was achieved by first converting each voxel-based image of the crystals to a triangulated surface structure (Matlab's isosurface function). This mesh was smoothed by applying the function smoothpatch<sup>38,39</sup> three times (parameter *itt* = 3) to smoothen steps in the surface caused by discretization into voxels by  $\mu$ CT. Previously, we reported that this did not affect the volume or shape of similar crystals.<sup>27</sup> For the overlaying procedure, the rotation and center point of the last  $\mu$ CT image served as reference. Hence, each triangulated surface of the crystals was moved and rotated according to the difference of its corresponding center point and rotation to those of the last measurement. With this procedure, the crystals overlaid quite well. However, the overlay was still not perfect. This was likely because of small deformations of the racks over the course of the experiments.

Additional errors were introduced because the center point and rotation of the racks could not be perfectly determined.

To correct for the small overlaying errors, the positions of the crystals' surfaces were numerically optimized to overlay better. The procedure explained below is based on the idea that due to the cubic unit cell of PA crystals, growth rates in all [111] directions should be equal. To satisfy this condition and hence reach optimal overlay, a correction vector was calculated for each crystal at each time point. The correction vector moves each crystal surface such that the standard deviation of displacements of its surface in all eight [111] directions toward its final state becomes minimal.

To apply this concept, we determined the directions of the [111] faces in each last measurement, which contains a faceted shape of each crystal, using our previously published face detection algorithm<sup>20</sup> and the geometric crystal model that is shown in Figure 2. The algorithm yields

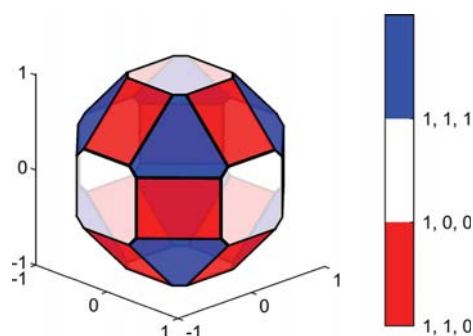


**Figure 2.** Geometric crystal model of potash alum with [111, 110, 100] faces according to Ma et al.<sup>15</sup> Opposing faces are assumed to be symmetrical.

- a rotation matrix that rotates the normals of the crystal model such that it fits to an image of a crystal
- and distances of the crystal's faces to its center of mass. The procedure only assumes symmetry for opposing faces because we have observed<sup>27</sup> that PA crystals do not necessarily have an octahedral shape.

Notably, this method is only able to determine the direction of face normals of faceted crystals. However, because the crystals were glued to the rack, their orientation with respect to the rack did not change during the experiment. Therefore, if the orientation of the crystal is known at one point in time during the experiment, then its orientation is also known at all other times. It was, therefore, sufficient to find the rotation matrix for the faceted version of each crystal (last point in time).

In a next step, we calculated the distances between the surfaces of a crystal at each of its states of growth to its final state in [111] directions according to Section 2.6. We then numerically optimized a correction vector for each state of growth of each crystal toward the corresponding final state such that the standard deviation of the distances in [111] directions became minimal at each point in time. The numerical optimization was done using the interior point algorithm through Matlab's fmincon function. This yielded optimal overlap. We chose the [111] faces for optimization because they were the largest faces of the faceted crystals and they should all grow at the same rates because of the cubic unit cell of PA. This optimization step resulted in corrections between zero and three voxel lengths, with the mean length of the correction vectors of all optimizations being about 0.6 voxel lengths. As a rule of thumb, the resolution of the  $\mu$ CT is two voxel lengths. In conclusion, the error of the overlaying procedure is less than the measurement error of the  $\mu$ CT.

**2.6. Calculation of Three-Dimensional Growth Rates.** Growth vectors were calculated from these overlaid meshes as displacements of the crystal surface between time points (Figure 3). As a first step, the regions where the crystals were glued to the racks were removed from

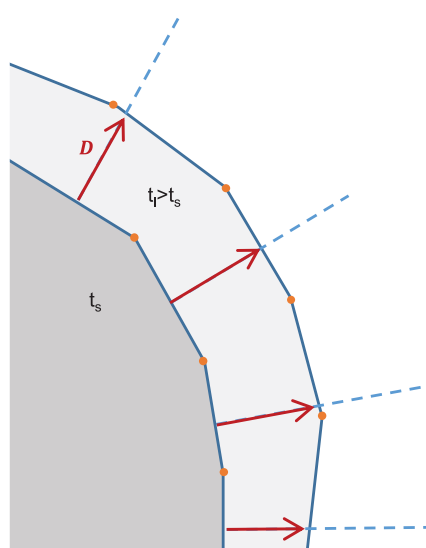


**Figure 3.** Two-dimensional scheme of the distance calculation. Orange dots indicate vertices of the inner mesh (dark gray,  $t_s$ ) and the outer mesh (light gray,  $t_l$ ). Red arrows indicate the distance vectors that point in the normal direction of the inner mesh's border lines, representing triangles in three dimensions.

the meshes. This was done by manually determining three points within the glued region of the last measurement of each crystal. From these points, a plane was constructed. Then, two meshes were considered: a smaller mesh from an earlier time point ( $t_s$  and dark gray in Figure 3) and a larger one from a later time point ( $t_l > t_s$  and light gray in Figure 3). The overlaying procedure (Section 2.5) ensured that the smaller mesh was inside the larger one. Then, the plane was displaced in its normal direction toward the crystal center by 10 voxel lengths ( $80 \mu\text{m}$ ). All points of the inner mesh that were on the opposite side of the plane with respect to the crystal center were deleted from the mesh. This ensured that the glued areas, where no growth could occur, would not affect the measurements.

It is now described how growth vectors were calculated from these cut meshes. For better visualization, the scheme is represented only in 2D in Figure 3. The conceptual extension to 3D is straightforward. For each triangulation element of the small mesh, lines through their center and in the normal direction were constructed (dashed blue lines in Figure 3) and intersected with the outer surface. The results provided direction-dependent distances (red arrows in Figure 3). Even though the concept is quite simple, the calculations become numerically expensive for the  $\sim 10^5$  surface elements per crystal. The algorithm is explained in the Supporting Information. We applied the inverse rotation obtained by the fitting algorithm (Section 2.5) such that all crystals are orientated according to the shape model shown in Figure 2. Like this, differently orientated crystals can be compared. We also applied symmetry conditions corresponding to the cubic unit cell of PA. Details for this are explained in the Supporting Information.

In this article, we present the distance vectors in spherical coordinates with the polar angle  $0 \leq \theta < \pi$  and azimuthal angle  $0 \leq \varphi < 2\pi$ . The length of the displacements was divided by the time of growth  $\Delta t = t_l - t_s$  to gain displacement rates  $G_{\text{measured}}$  averaged over the sampling time interval. An example is shown in Figure 4.

It is feasible to describe such data using a function to make it useful for modeling purposes. Therefore, spherical harmonics (SH) functions were fitted to the discretized displacement rates. The least-squares fitting method of Zotkin et al.<sup>40</sup> was used. For this, it is assumed that the displacements can be described as a function of  $\theta$  and  $\varphi$

$$G(\Theta, \varphi) = \sum_{n=0}^{\infty} \sum_{m=-n}^n C_n^m Y_n^m(\Theta, \varphi) \quad (1)$$

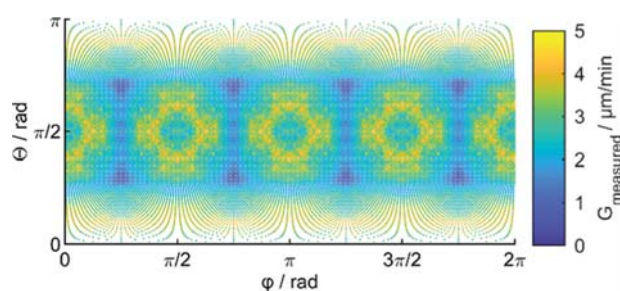


**Figure 4.** Discretized displacement rates of crystal 1 of experiment 1 between 0 and 4 min with applied symmetry conditions.

$$Y_n^m(\Theta, \varphi) = (-1)^m \sqrt{\frac{2n+1(n-|m|)!}{4\pi(n+|m|)!}} P_n^{|m|}(\cos \Theta) e^{im\varphi} \quad (2)$$

where  $\sigma$  is a parameter that determines the number ( $n = \sigma^2 + 2\sigma + 1$ ) of SH  $Y_n^m(\Theta, \varphi)$ , and corresponding weights  $C_n^m \cdot P_n^{|m|}(x)$  are Legendre polynomials. We chose  $\sigma = 20$ , and hence  $n = 441$ . The rationale behind this choice is explained in the Supporting Information. To determine the weights, one may set up eq 1 for each measured displacement rate. In each equation,  $\Theta$ ,  $\varphi$ , and  $Y_n^m$  are constants. This yields a linear set of equations that can be solved for the weights using the least-squares method<sup>40</sup> (Matlab's lsqr function). For assessment of the quality of the fits to this linear model, we calculated the coefficient of determination  $R^2$ . An exemplary graphical representation of the fitted function to the data in Figure 4 is shown in Figure 5.

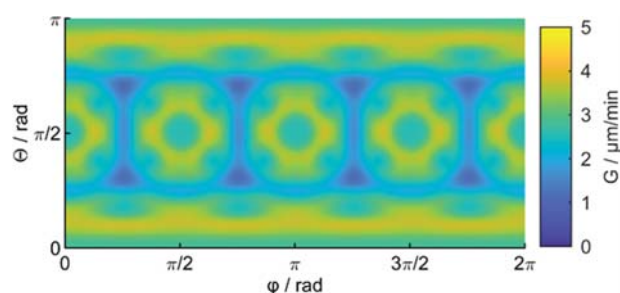


**Figure 5.** Graphical representation of eq 1 as fitted to the surface displacement rates of crystal 1 of experiment 1 between 0 and 4 min.  $R^2 = 0.91$ .

**2.7. Crystal Growth Model.** Crystal growth was modeled using H-representations according to Reinhold et al.<sup>23</sup> In 3D, H-representations describe convex bodies through a set of confining planes. Each plane is defined by a normal  $a_i$  (face normal) and a corresponding distance to a reference point  $h_i$  (face distance). The normals  $a_i$  are summarized in a matrix  $A$ , and the distances  $h_i$  are summarized in a vector  $h$ . This representation is convenient for crystal growth models because growth can be modeled by increasing the face distances. Notably,  $A$  contains no size information. Therefore, it remains unchanged during simulations.

We defined matrix  $A$  using the HEALPix algorithm<sup>41</sup> using a grid resolution of 10 to model the growth of crystals. This resulted in 1200 face normals. The actual shape of a crystal is defined by the vector  $h$ . For a sphere with radius  $r$ ,  $h = r \cdot (1 \ 1 \ 1 \dots)^T$  can be used. Other shapes are little more complex and are explained below. The first step to produce an initial H-representation ( $h_{\text{init}}$  and  $A$ ) is to define a convex body that is to be investigated. This can either be done through another H-representation or a set of vertices (V-representation). Both representations can be converted into each other using the software package *cddlib*.<sup>42</sup> As a 2D example, Figure 6 considers a square with the vertices  $(1 \ 1)^T$ ,  $(-1 \ 1)^T$ ,  $(1 \ -1)^T$ , and  $(-1 \ -1)^T$  that can be summarized in a matrix  $V$ .

$$V = \begin{pmatrix} 1 & -1 & 1 & -1 \\ 1 & 1 & -1 & -1 \end{pmatrix} \quad (3)$$

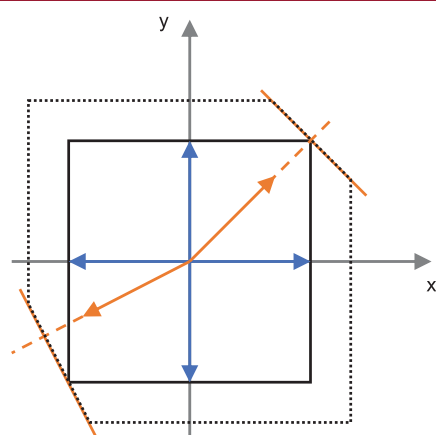


**Figure 6.** Two-dimensional scheme of the growth model. The black square indicates an initial shape that is defined by the blue face normals. Additional orange face normals can be defined, and face distances can be calculated so that they do not affect the initial shape. The initial shape is grown by increasing the face distances and leads to the dotted outline.

This corresponds to an H-representation with the normals  $(1\ 0)^T$ ,  $(-1\ 0)^T$ ,  $(0\ 1)^T$ , and  $(0\ -1)^T$  (blue arrows in Figure 6) and a corresponding face distance vector  $(1\ 1\ 1\ 1)^T$ . This is the minimum number of faces needed to describe this shape. However, the shape can also be described using additional normal vectors  $a_i$  (e.g., the orange ones in Figure 6). These vectors represent the normals defined by HEALPix in matrix  $A$ . The corresponding face distances  $h_{\text{init}}$  are then chosen so that just no additional vertex is generated. This corresponds to the scalar product  $h_{i,\text{init}} = \|a_i^T \circ V\|_{\text{max}}$ . Growth can now easily be modeled by increasing the entries in  $h$ . The rates may vary for each  $h_i$  and can be chosen according to a function (i.e., eq 1) of the direction of the normals in  $A$ . As an example, in Figure 6, the growth of the normals in the direction of the axes (blue vectors) is considered to be much faster than that of the two additional faces (orange vectors) to yield the dotted shape. This illustrates how direction-dependent growth leads to the appearance of slowly growing faces.<sup>23,25,43</sup>

We described initial shapes that resulted from  $\mu$ CT measurements using 1200 HEALPix face normals to model their growth. For these shapes, two challenges are:

- (1) The imaged crystals were not perfectly convex. However, H-representations can only describe convex bodies. A convex hull was calculated (Matlab's `convhull` function) for each  $\mu$ CT image to overcome this issue. This yielded a V-representation from which an initial shape was created.
- (2) The glued regions did not grow in the experiments. This was considered in the growth model by adding a face with the same normal as the previously described glued face and setting its growth rate to 0.

The herein described growth model was compared to a benchmark model as described in Section 3.2. For the benchmark model, an octahedron was defined by [111] faces. Its volume was scaled to the volume of the initial  $\mu$ CT shape. Then, the glued plane was added to account for no growth in this direction. In both models, growth was considered by applying the growth rates of eq 1 to the initial face distances  $h_{\text{init}}$ , except for the glued plane where  $G = 0$ .

In Section 3.3, the calculations were conducted dimensionless. For this, an initial dimensionless H-representation ( $h_{\text{init}}^*$  and  $A$ ) was defined such that it had the same volume as a sphere with radius  $r = 1$

$$h_{\text{init}}^* = s \cdot h_{\text{init}} \quad (4)$$

The scale factor  $s$  was found by numerically finding the zero point of the function

$$f(s) = f_{h \rightarrow v}(s \cdot h_{\text{init}}) - \frac{4}{3}\pi \quad (5)$$

where  $f_{h \rightarrow v}$  is a function that calculates the volume of a H-representation.<sup>14</sup> The bisection method with  $10^{-3} \leq s \leq 10$  (Matlab's `fzero` function) was employed to find the zero point. The direction-dependent growth rate defined in eq 1 is normalized by

$$G^*(\Theta, \varphi) = \frac{G(\Theta, \varphi)}{G_{111}} \quad (6)$$

where  $G_{111}$  is the growth rate in the [111] direction. Growth is then modeled by

$$h^*(t) = h_{\text{init}}^* + 0.5 \cdot t \cdot G^*(\Theta, \varphi) \quad (7)$$

where  $\Theta$  and  $\varphi$  are the polar and azimuthal angles of  $A$  expressed in spherical coordinates. The dimensionless time factor  $t$  describes the increase of a crystal's size in the [111] direction. The factor 0.5 stems from the fact that there are two opposing [111] faces that grow in opposing directions. By applying the factor 0.5,  $t = 0.1$  can be interpreted as an increase in size in the [111] direction by 10% and  $h^*(t)$  describes the shape of a crystal and its size relative to the initial size. After each time step, it is checked whether  $h^*$  is valid. In this context, valid means that each of its entries  $h_i^*$  leads to a confinement (i.e.,  $h_i^* < \|a_i^T \circ V^*\|_{\text{max}}$ ). Otherwise, it is set to  $h_i^* = \|a_i^T \circ V^*\|_{\text{max}}$ . Details are explained by Reinhold et al.<sup>23</sup>

**2.8. Shape Measurement.** Crystal shape is hard to describe using a single measure. We used a measure that describes the fraction of ideal surface  $\alpha$ , and a 3D aspect ratio  $\Phi_n$ . However, we do not claim a complete description of shape using these simple measures. The shape factors are merely used for better visualization and easier interpretability. Notably, the H-representations and  $\mu$ CT images contain much more shape information.

For each analyzed crystal, the surface area  $S_i$  of each surface element was calculated. In addition, each element was classified into "ideal" or "not ideal" depending on the minimal angle of its normal vector to the normals of the geometric crystal model (Figure 2). An angle tolerance of  $5^\circ$  was applied to satisfy ideality. Eq 8 is then used to calculate  $\alpha$ .

$$\alpha = \frac{\sum S_{i,\text{ideal}}}{\sum S_i} \quad (8)$$

For a perfect crystal that is described well by a geometric model,  $\alpha$  approaches 1. Otherwise,  $0 \leq \alpha < 1$ .

To further evaluate the shape of the PA crystals, we applied a 3D aspect ratio  $\Phi_n$  before.<sup>27</sup> The vector  $\Phi_n$  describes the symmetry of a potash alum crystal

$$\Phi_n = \frac{h_{111}}{\|h_{111}\|_{\text{max}}} \quad (9)$$

Therein,  $h_{111}$  are the face distances in the eight [111] directions. For a fully symmetric crystal,  $\Phi_n$  is a vector of eight ones. Because we chose the center of mass of each crystal as a reference point of the H-representations, opposing faces have the same entries in  $\Phi_n$ . Therefore, asymmetric crystals may have up to six entries smaller than 1. For better readability and to avoid redundancy, we only give the four unique entries of  $\Phi_n$  in this text.

### 3. RESULTS AND DISCUSSION

In this section, first, the growth rates that are obtained from the  $\mu$ CT images are presented. Then, these rates are used to parametrize the growth model. Modeled crystals are compared to experimentally obtained crystals for validation. Finally, we used the model to simulate the growth of nonideal crystals.

**3.1. Growth Rates.** In the following, we first describe the results of our analysis for one exemplary crystal from the first

measurement series (denoted as crystal 1) and then combine the results of all successful analyses of the first series. The images of the second measurement series are used for validation only (Section 3.2).

Figure 7A,C shows images of a particular crystal in its initial state, and Figure 7B,D shows the same crystal after 17 min of

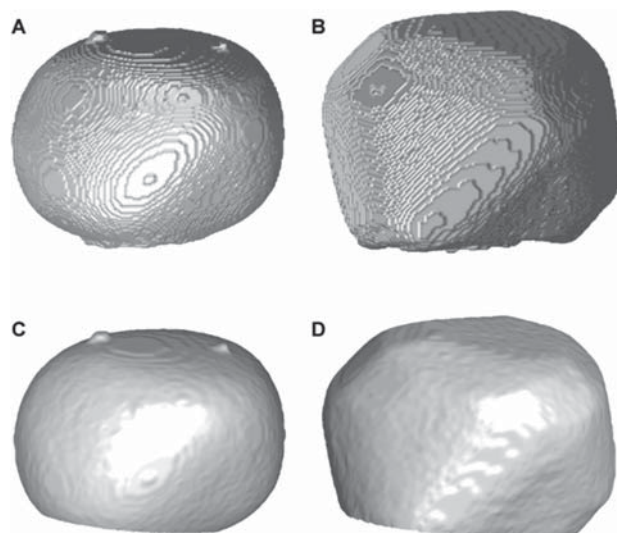


**Figure 7.** Images of crystal 1 before growth (0 min, A, C): (A) raw micro-computed tomography ( $\mu$ CT) image and (C) smoothed and glued region cut. The same crystals after 17 min growth (B, D): (B) raw  $\mu$ CT image and (D) smoothed and glued region cut. The glued spots are on the bottom of the  $\mu$ CT images. The bottom row (C, D) shows the surfaces that are used for distance calculations.

growth in its final state. Visual inspection of the  $\mu$ CT images indicated that they assumed a faceted shape after 17 min (Figure 7B; except the glued area on the bottom). A geometric shape model was fitted to this faceted shape (Figure 8). This gave the crystal's orientation. Because the crystals were adhered to the rack, their orientation did not change during the experiment.



**Figure 8.** Left: micro-computed tomography image of crystal 1 after 17 min of growth; center: geometric crystal model (Figure 2) fitted to the crystal; right: combination of crystal image and fitted model.

Overlaying images of crystals (Figure 9) also showed that growth was slow. The displacement rates in [111] directions, which were the slowest rates, were only around  $2 \mu\text{m}/\text{min}$  (Figure 12). This is below the resolution of the  $\mu$ CT measurements at a voxel spacing of  $8 \mu\text{m}$ . As a rule of thumb, the resolution is twice the voxel spacing (i.e.,  $16 \mu\text{m}$ ). Therefore, Figure 9A illustrates that overlaying images in 1 min intervals would not generate reasonable results. In many regions, the surface of the later point in time (red in Figure 9) is within the surface at an earlier time (blue in Figure 9). This would lead to

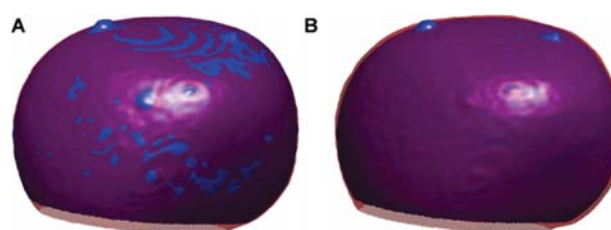


**Figure 9.** Overlaying surfaces of crystal 1 after (A) 0 and 1 min growth and (B) 0 and 4 min growth. The 0 min surface is displayed in opaque blue, and the other surface (1 or 4 min, respectively) is displayed in transparent red.

unphysical negative measured displacements. Consequently, the growth of the crystals was evaluated in 4 min steps (Figure 9B): between 0 min and 4 min, 1 min and 5 min, ..., 13 min and 17 min. This procedure leads to displacements of at least  $8 \mu\text{m}$  ( $4 \text{ min} \times 2 \mu\text{m}/\text{min}$ ) in each direction, resulting in an increase in size of at least  $16 \mu\text{m}$ . There were occasional overlapping inaccuracies that resulted from measurement artifacts, such as the two small regions on the top of Figure 9B. However, most of the surface overlaid well.

From these overlaying surfaces, displacement rates in all directions were calculated and fitted to SH functions (Section 2.6). An example of the resulting fit of eq 1 to the surface displacement rates is shown in Figure 10 together with the

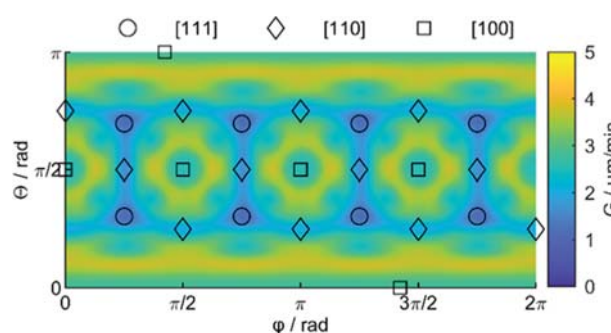


**Figure 10.** Average surface displacement rates of crystal 1 between 0 and 4 min. Markers indicate the orientation of the shape dominating faces of the same crystal after 17 min of growth.  $R^2 = 0.91$ .

orientation of the face groups that were considered for the geometric crystal model (Figure 2; that is, the [111], [110], and [100] face groups). These faces lie within the minima of the surface displacement rates. This can be seen as a first indication that our method yields reasonable results because slowly growing faces dominate the shape of crystals.<sup>23,25</sup>

Further, it is interesting that there are additional minima at orientations that are often not assumed as crystal faces of PA.<sup>15,23</sup> The Bravais–Friedel–Donnay–Harker (BFDH) method<sup>45</sup> is used to predict crystal morphologies based on the lattice geometry. According to the BFDH method, the six most dominant face groups of PA are [111], [100], [210], [211], [110], and [221]. According to experimental studies,<sup>15,37,44,46</sup> the shape of PA crystals is dominated by [111], [110], and [100] face groups. Additionally, fast-growing faces are the [221], [211], and [210] faces.<sup>44</sup> Their locations with respect to the measured growth rates are shown in Figure 11. The [211] face group lies within minima of the growth rates, while the [221] and [210] faces lie on saddle points or maxima of growth rates.

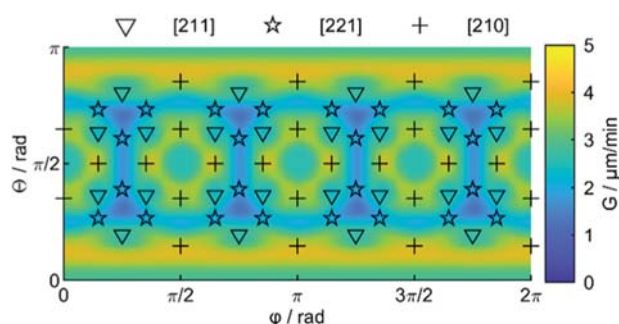


**Figure 11.** Surface displacement rates of crystal 1 between 0 and 4 min together with the orientation of fast-growing faces according to the literature<sup>44</sup> and the Bravais–Friedel–Donnay–Harker method.  $R^2 = 0.91$ .

Therefore, the [221] and [210] faces should not be expected to contribute to the shape of the crystals here. Only the [211] face is observed in some final shapes. However, it was very small and, therefore, not included in the geometric crystal model (Figure 2).

Rates obtained from different times and different crystals may be combined with a single data set (see Appendix III and Sup. 4 in the Supporting Information for more details). A fit of the combined data set to eq 1 is shown in Figure 12. The

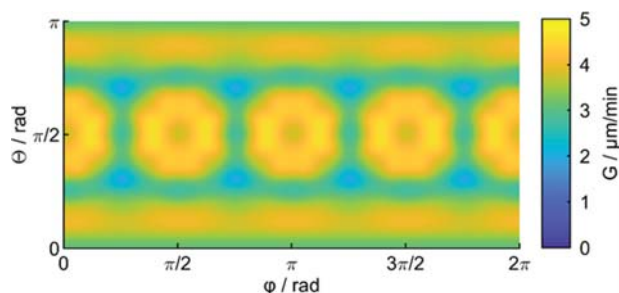


**Figure 12.** Surface displacement rates as calculated from all crystals from measurement series one and averaged over all time points.  $R^2 = 0.995$ .

corresponding 441 parameters  $C_n^m$  for eq 1 are provided in the Supporting Information. A fit of the displacement rates of all analyzed time points of crystal 1 to eq 1 is shown in Sup. 7.

A comparison of the growth rates obtained in this study with those in the literature can be seen in the Supporting Information. Here, we want to focus on the 3D nature of our data. Data in the literature are only available for certain faces.

**3.2. Validation.** The fitted  $G(\Theta, \varphi)$  (eq 1) that resulted from the combined data set (Figure 12) provides the growth rate in any direction. The rates can now be applied to varying initial shapes using our growth model (Section 2.7). As first performance test for the growth model, the growth of the initial shape of the measured crystals of measurement series one is simulated. As a validation, the model is applied to the crystals of measurement series two. Notably, the data of series two was not used to determine  $G(\Theta, \varphi)$ .

The modeled volumes are compared to the measured volumes in Figure 13 (left). The correct description of volume in crystallization models is important for accurate mass balances. Our new model slightly overestimates the growth of the crystals. This could be explained by the initial shapes of the crystals being

converted to strictly convex bodies for their growth to be modeled. The benchmark model (growth of octahedrons) considers growth of the slowly growing [111] faces only. This leads to an underestimation of the volume of about 20%. The new model also considers the abraded, faster-growing regions. In the literature,<sup>46,47</sup> fast growth of damaged crystals is attributed to strain and dislocations in the crystals. Our results demonstrate that the presence of fast-growing surfaces may also contribute to a faster increase in volume.

We are predominantly interested in the description of crystal shape. Therefore, Figure 13 (right) compares the fractions of ideal surface elements  $\alpha$ . The benchmark model considers growth of octahedrons. Therefore, it is not able to adequately describe crystal shape ( $\alpha = 1$  for all crystals). The model that we proposed here describes shape much better. However, quite low coefficients of determination must still be accepted ( $R^2 = 0.73$ ). The calculation of  $\alpha$  is likely affected by conversion to convex bodies to a greater extent than the calculation of volumes. Figure 14 graphically visualizes the modeled results for one exemplary crystal and qualitatively illustrates the description of shape.

Overall, Figures 13 and 14 illustrate that the growth model is able to describe the growth of nonfaceted crystals well. No difference between the modeled crystals from the validation and calibration experiments is observed (Figure 13). This finding supports the reproducibility of the experiments and the validity of the growth model. Most importantly, the model describes the shape of nonfaceted crystals.

**3.3. Effect on Crystal Shape.** In the literature, the effect of abrasion on crystal shape is studied.<sup>6</sup> Here, the effect of crystal growth on the shape of abraded crystals is studied, to advance the understanding of the interaction of crystal growth and abrasion.

In a previous study, we have examined the evolution of crystal shapes during a seeded crystallization process of PA.<sup>27</sup> The seed material has been damaged such that no geometric crystal model could be fitted to most of the crystals. This was because the crystals did not express the typical habit of PA. The change in shape has been most pronounced in the first 30 min of the process. During this time, the damaged seed material has grown and healed such that it could be described using [111] faces only. The volume has increased by a factor of about 4 within these first 30 min. Throughout the whole process, the seed crystals have increased their volume by a factor of about 10. The shape evolution after 30 min could be described using a classical growth model that considered only the growth of the [111] faces. However, we have shown that most crystals were asymmetrical even though all crystals expressed the typical habit of PA after 30 min. This was unexpected because PA crystals should grow symmetrically due to their cubic unit cell. Therefore, we have hypothesized that such crystals could only be the result of asymmetrical seed material.

To evaluate this hypothesis, we here applied the growth model (Section 2.7) to varying nonideal initial shapes ( $\alpha < 0.9$ ) until their shape could be well described using the faces shown in Figure 2 ( $\alpha \geq 0.9$ ). Results of our simulations are summarized in Figure 15. The modeled crystal shapes are displayed in gray. The borders of their faces are displayed in dark gray lines. The best representation of each shape using the geometric crystal model of PA (Figure 2) is displayed with black lines. This shows that the initial shapes did not express the typical habit of PA. Through growth, they approached the typical habit.

First, the general applicability of the growth model was demonstrated by the simulation of three exemplary shapes

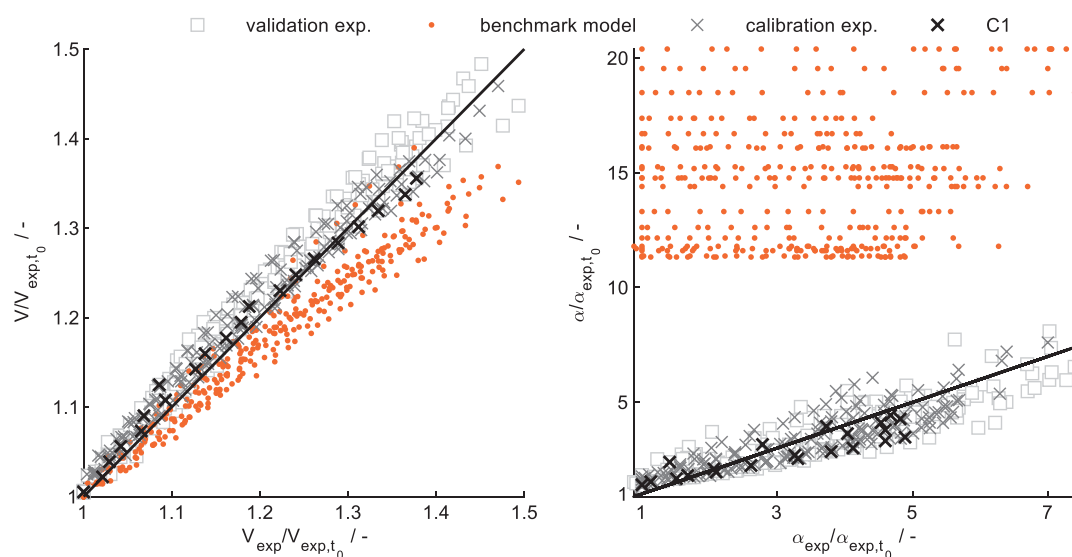


**Figure 13.** Validation of the growth model with respect to volume (left;  $R^2_{\text{calibration}} = 0.96$ ,  $R^2_{\text{validation}} = 0.95$ ,  $R^2_{\text{benchmark}} = 0.75$ ) and with respect to the fraction of ideal surface area  $\alpha$  (right;  $R^2_{\text{calibration}} = 0.73$ ,  $R^2_{\text{validation}} = 0.73$ , no reasonable  $R^2$  calculated for benchmark). Straight lines represent a perfect model ( $V = V_{\text{exp}}$ ). Data of crystal 1 of the calibration experiment (C1) are highlighted as black crosses.

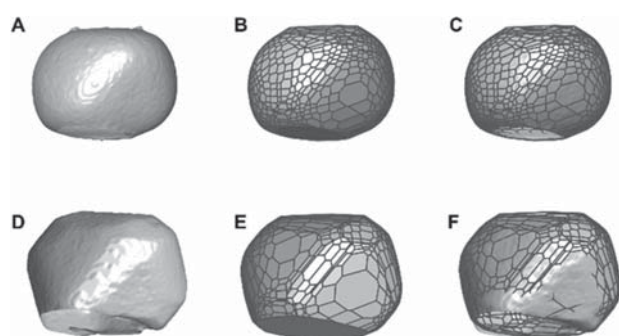


**Figure 14.** Micro-computed tomography ( $\mu$ CT) images of crystal 1 of the calibration experiment after 0 min of growth (A) and 17 min of growth (D). Corresponding convex initial shape (B) and 17 min shape (E) of the simulation. (C, F) Corresponding combinations of the  $\mu$ CT image (light gray) and modeled shape (outlines). In (F), the overlaying mesh shows that most regions of the crystals are described well. In some regions, the mesh is inside the crystal, which indicates that growth was faster at these regions in the experiments.

(Figure 15A–C). Then, the growth of three initial shapes that resulted from 3D images of the seed material of the previous study<sup>27</sup> were simulated (Figure 15D–F). Note, that only seeds could be considered that expressed some faces such that their orientation with respect to the unit cell was known. Therefore, this selection favored crystals that have been damaged to a lesser extent.

In a first simulation, the growth of a sphere was studied (Figure 15A). The size was increased by a factor of 1.56, and the volume by a factor of 2.9 to reach the typical habit of PA. In addition, it was initially perfectly symmetrical with respect to the geometric crystal model of PA (all entries in  $\Phi_n \geq 0.85$ ). Growth led to a symmetric PA crystal that expressed the [111], [110] and [100] faces. This shape was similar to the shapes we studied experimentally in Sections 3.1 and 3.2. As the second initial shape (Figure 15B), a platelike cuboid was chosen. The cuboid was rotated such that its faces did not have the same normals as any PA crystal face. This led to an asymmetrical initial shape with

respect to the geometric crystal model of PA. An increase in size by a factor of 3.16 and in volume by a factor of 18.8 led to an asymmetrical shape of PA. Thirdly, the growth of a rod-shaped cuboid was simulated (Figure 15C). It was oriented in the same way as the platelike cuboid. Consequently, this initial shape was asymmetrical with respect to the crystal model as well. The size needed to be increased by a factor of 2.31 and the volume by a factor of 9.3 such that the typical habit of PA was generated. The crystal remained asymmetrical. These cuboid shapes could resemble damaged particles (e.g., broken or abraded).

Figure 15D–F illustrates the growth of three seed crystals of our previous study.<sup>27</sup> The crystal sizes were increased by factors of 1.78, 2.29, and 1.60, respectively, and the volumes were increased by factors 3.7, 3.9, and 3.5. In these cases, growth of the symmetric initial shape (Figure 15D) yielded a symmetric crystal and correspondingly the asymmetric initial shapes (Figure 15E,F) yielded asymmetric crystals. We have observed similar shapes in our previous study.<sup>27</sup>

Our results illustrate that the initial shape shown in Figure 15A could be healed during the particular crystallization process that we have studied previously. More extreme shapes as those shown in Figure 15B,C would not have healed within the first 30 min of the process. However, these examples show that crystal shapes that differ from the classical shape model heal and express the typical crystal faces. Such asymmetrical shapes could result from damaged seed material or breakage during a process. In addition, growth of asymmetrical initial shapes, without typical crystal faces, resulted in shapes with the typical habit of PA. The final shape depends on the initial shape and may be asymmetrical. We have observed similar asymmetric shapes in a previous study and described how their shapes become more symmetrical through crystal growth.<sup>27</sup> Figure 15D–F illustrates that such asymmetrical shapes could have been the result of healing of damaged seed crystals. The increases in volumes were comparable to those that we have observed in our previous study. We mentioned before, that only [111] faces have been observed in the previous study. Here, also [110] and [100] faces were observed. In the previously studied process, supersaturation has been higher than in this study. This causes

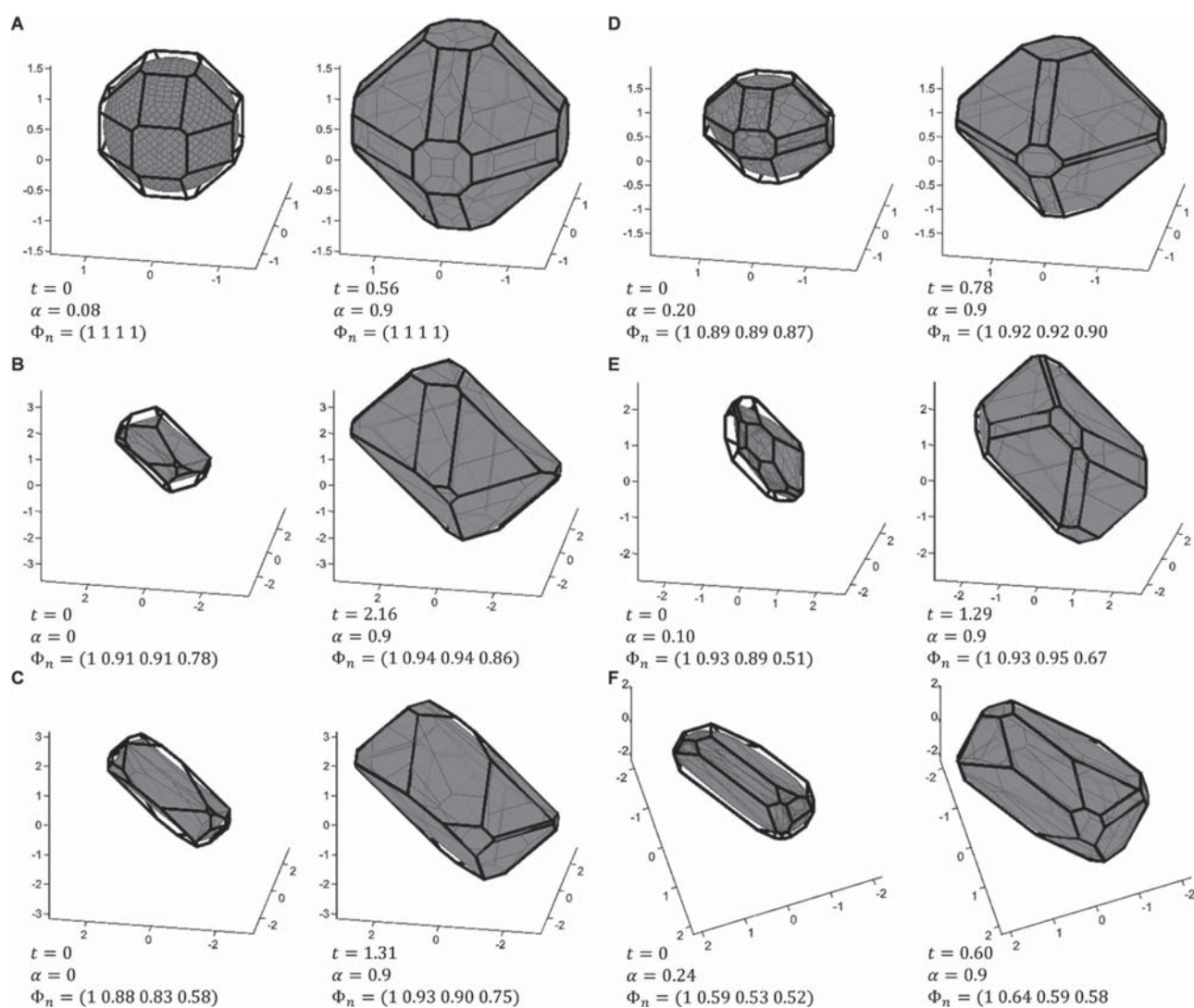


Figure 15. Modeled crystal shapes resulting from different initial crystals.

different relations between the face-specific growth rates. The rates of the  $[110]$  and  $[100]$  faces increase faster with increasing supersaturation than that of the  $[111]$  faces.<sup>15</sup> Therefore,  $[110]$  and  $[100]$  faces have disappeared more quickly at higher supersaturation.

From a more general perspective, our simulations show that nonideal shapes heal by fast growth of damaged regions. This results in faster growth with respect to the volume of abraded crystals (Figure 13 left, gray data) than ideally faceted crystals (Figure 13 left, orange benchmark). The results presented in Figure 15 and discussed in this section show that the increase in size (and hence volume) needed for crystals to heal strongly depends on the initial shape of the crystals. The model was designed such that it is independent of crystal size (Section 2.7) and results can conveniently be interpreted as a relative increase in size. When growth rates are assumed to be independent of size, small crystals will need less time to heal than large crystals even if they have the same shape. This is because an absolute growth of, e.g.,  $10 \mu\text{m}$  of a crystal would result in an increase in size by 100% of a  $10 \mu\text{m}$ -sized crystal but only an increase in size of 1% for a  $1 \text{ mm}$ -sized crystal. Our experimental method can so far only be applied to crystals larger than roughly  $500 \mu\text{m}$ .

Currently, the assumption of size-independent growth is only plausible but not proven.

#### 4. CONCLUSIONS

Crystal growth is commonly assumed to occur in the normal direction of crystal faces and is primarily discussed with respect to solution supersaturation. However, in crystallization processes, agitation often induces damage to the crystals and renders nonfaceted crystal shapes. Therefore, it is inaccurate to describe such crystals using only the common faces. In this contribution,  $\mu\text{CT}$  and 3D image analyses were used to track the growth of abraded crystals. From these images, growth rates in all directions of crystal surfaces were determined and described using spherical harmonics functions. These growth rates were used to parametrize a 3D crystal growth model. The model was able to describe the growth of nonfaceted growth domains in addition to the common crystal faces. Additionally, the shape of convex crystals was accurately described in 3D. The model was used to validate the measured growth rates and to simulate the growth of nonfaceted shapes. The results show that for the prediction of crystal shape evolution, thermodynamic properties (i.e., supersaturation, corresponding faceted growth rates) are

only one piece in the puzzle. The initial shape of crystals cannot be ignored.

Our simulations showed that the observed growth behavior led to accelerated growth in terms of volume compared to models that only considered the growth of crystal faces. We found that crystals heal and assume faceted shapes through fast growth of damaged regions. This study provides a foundation for detailed model-based analysis of the interaction of crystal growth and abrasion.

## ■ ASSOCIATED CONTENT

### Supporting Information

The Supporting Information is available free of charge at <https://pubs.acs.org/doi/10.1021/acs.cgd.1c00849>.

Algorithm used to calculate the distance between surfaces (Appendix I); choosing the order of spherical harmonics (Appendix II); face-specific growth rates and their comparison with data from the literature (Appendix III); and additional figures (Appendix IV) (PDF)

Parameters for the spherical harmonics function (TXT)

## ■ AUTHOR INFORMATION

### Corresponding Author

**Heiko Briesen** – Chair of Process Systems Engineering, Technical University of Munich, 85354 Freising, Germany; [orcid.org/0000-0001-7725-5907](https://orcid.org/0000-0001-7725-5907); Phone: +498161715383.; Email: [heiko.briesen@mytum.de](mailto:heiko.briesen@mytum.de); Fax: +498161714510

### Authors

**Simon A. Schiele** – Chair of Process Systems Engineering, Technical University of Munich, 85354 Freising, Germany; [orcid.org/0000-0003-3026-2768](https://orcid.org/0000-0003-3026-2768)

**Ricardo Hupfer** – Chair of Process Systems Engineering, Technical University of Munich, 85354 Freising, Germany

**Frederik Luxenburger** – Chair of Process Systems Engineering, Technical University of Munich, 85354 Freising, Germany

Complete contact information is available at: <https://pubs.acs.org/10.1021/acs.cgd.1c00849>

### Author Contributions

The manuscript was written through contributions of all authors. All authors have given approval to the final version of the manuscript.

### Notes

The authors declare no competing financial interest.

## ■ ACKNOWLEDGMENTS

S.A.S. and H.B. are grateful for the financial support by Deutsche Forschungsgemeinschaft (DFG) through Project Number 456595618. The OptiMax Synthesis workstation was funded by the DFG through Grant 263666176 and the  $\mu$ CT through Grant 198187031. The authors thank Michaela Thalhammer for her persistent support with the  $\mu$ CT measurements and outstanding management of the laboratory.

## ■ ABBREVIATIONS

2D, two-dimensional; 3D, three-dimensional; BFDH, Bravais–Friedel–Donnay–Harker method; FBRM, focused beam reflectance measurements; PA, potash alum; SH, spherical harmonics;  $\mu$ CT, micro-computed tomography

## ■ ROMAN LETTERS

<b>A</b>	matrix with face normals for H-representations
$a_i$	face normal that is an element of <b>A</b>
$C_n^m$ [ $\mu\text{m}/\text{min}$ ]	weights of the spherical harmonics functions
$d$ [cm]	diameter of stirrer
$G, G_{111}, G_{\text{measured}}$ [ $\mu\text{m}/\text{min}$ ]	displacement rate, displacement rate in the [111] direction, measured displacement rates
$G^*$	dimensionless growth rate
$h, h_p, h_{111}, h_{\text{init}}, h_{i,\text{init}}$ [ $\mu\text{m}$ ]	face distances of a H-representation, element of the latter, face distances in the [111] direction, initial values of the face distances for the growth model, element of the latter
$h_{\text{init}}^*, h^*, h_i^*$	dimensionless initial face distance vector, dimensionless face distance vector, element of the latter
$m$ [kg], $m$	mass, parameter of the spherical harmonics function
$N_s, N_l$	number of triangulations of small and large crystals, respectively
$n$	parameter of the spherical harmonics function
$n$ [1/s]	rotational speed of the stirrer
$o$	order parameter of the spherical harmonics function
$P_n^{lm}$	Legendre polynomials
$S_p, S_{i,\text{ideal}}$ [ $\mu\text{m}^2$ ]	surface area of a surface element, surface area of an ideal surface element
$s$	scale factor
$t$	time factor that describes the increase in size of a modeled crystal
$v, V$ [ $\mu\text{m}$ ]	vertex of a polytope, all vertices of a polytope
$V^*$	dimensionless vertices of a polytope
$Y_n^m$	spherical harmonics

## ■ GREEK LETTERS

$\alpha$	fraction of surface area that is ideal
$\Delta t$ [min]	time of growth between two analyzed $\mu$ CT measurements
$\Delta w$ [mg/g]	absolute supersaturation
$\eta$ [Pa s]	dynamic viscosity
$\theta$ [rad]	polar angle
$\rho_{\text{PA}}, \rho$ [ $\text{g}/\text{cm}^3$ ]	density of potash alum, solution density
$\sigma$	relative supersaturation $\Delta w/w_{\text{saturation}}$
$\Phi_n$	symmetry shape factor
$\varphi$ [rad]	azimuthal angle

## ■ REFERENCES

- (1) Dandekar, P.; Kuvadia, Z. B.; Doherty, M. F. Engineering Crystal Morphology. *Annu. Rev. Mater. Res.* **2013**, *43*, 359–386.
- (2) Blagden, N.; Matas, M.; de Gavan, P. T.; York, P. Crystal engineering of active pharmaceutical ingredients to improve solubility and dissolution rates. *Adv. Drug Delivery Rev.* **2007**, *59*, 617–630.

- (3) Borchert, C.; Sundmacher, K. Morphology evolution of crystal populations: Modeling and observation analysis. *Chem. Eng. Sci.* **2012**, *70*, 87–98.
- (4) Eisenschmidt, H.; Bajcinca, N.; Sundmacher, K. Optimal Control of Crystal Shapes in Batch Crystallization Experiments by Growth-Dissolution Cycles. *Cryst. Growth Des.* **2016**, *16*, 3297–3306.
- (5) Bötschi, S. *Optimization and Feedback Control of the Size and Shape Evolution of Elongated Crystals in Suspension*; ETH Zürich, 2019.
- (6) Reinhold, A.; Schorsch, S.; Mazzotti, M.; Briesen, H. Modeling and measurement of abraded particles. *Powder Technol.* **2015**, *271*, 134–140.
- (7) Szilágyi, B.; Nagy, Z. K. Model-based analysis and quality-by-design framework for high aspect ratio crystals in crystallizer-wet mill systems using GPU acceleration enabled optimization. *Comput. Chem. Eng.* **2019**, *126*, 421–433.
- (8) Lovette, M. A.; Browning, A. R.; Griffin, D. W.; Sizemore, J. P.; Snyder, R. C.; Doherty, M. F. Crystal Shape Engineering. *Ind. Eng. Chem. Res.* **2008**, *47*, 9812–9833.
- (9) Simon, L. L.; Pataki, H.; Marosi, G.; Meemken, F.; Hungerbühler, K.; Baiker, A.; Tummala, S.; Glennon, B.; Kuentz, M.; Steele, G.; Kramer, H. J. M.; Ryzdzak, J. W.; Chen, Z.; Morris, J.; Kjell, F.; Singh, R.; Gani, R.; Gernaey, K. V.; Louhi-Kultanen, M.; O'Reilly, J.; Sandler, N.; Antikainen, O.; Yliruusi, J.; Frohberg, P.; Ulrich, J.; Braatz, R. D.; Leysens, T.; Stosch, M.; von Oliveira, R.; Tan, R. B. H.; Wu, H.; Khan, M.; Des O'Grady, Pandey, A.; Westra, R.; Delle-Case, E.; Pape, D.; Angelosante, D.; Maret, Y.; Steiger, O.; Lenner, M.; Abbou-Oucherif, K.; Nagy, Z. K.; Litster, J. D.; Kamaraju, V. K.; Chiu, M.-S. Assessment of Recent Process Analytical Technology (PAT) Trends: A Multiauthor Review. *Org. Process Res. Dev.* **2015**, *19*, 3–62.
- (10) Bötschi, S.; Rajagopalan, A. K.; Rombaut, I.; Morari, M.; Mazzotti, M. From needle-like toward equant particles: A controlled crystal shape engineering pathway. *Comput. Chem. Eng.* **2019**, *131*, No. 106581.
- (11) Briesen, H. Two-dimensional population balance modeling for shape dependent crystal attrition. *Chem. Eng. Sci.* **2009**, *64*, 661–672.
- (12) Hill, P. J.; Reeves, S. M. Effect of particle breakage conditions on child particle aspect ratio. *Powder Technol.* **2019**, *355*, 564–572.
- (13) Hill, P. J. Statistics of multiple particle breakage accounting for particle shape. *AIChE J.* **2004**, *50*, 937–952.
- (14) Kovačević, T.; Briesen, H. Simulations of crystal aggregation and growth: Towards correct crystal area. *AIChE J.* **2019**, *65*, No. e16525.
- (15) Ma, C. Y.; Wan, J.; Wang, X. Z. Faceted growth rate estimation of potash alum crystals grown from solution in a hot-stage reactor. *Powder Technol.* **2012**, *227*, 96–103.
- (16) Borchert, C.; Temmel, E.; Eisenschmidt, H.; Lorenz, H.; Seidel-Morgenstern, A.; Sundmacher, K. Image-Based in Situ Identification of Face Specific Crystal Growth Rates from Crystal Populations. *Cryst. Growth Des.* **2014**, *14*, 952–971.
- (17) Eisenschmidt, H.; Voigt, A.; Sundmacher, K. Face-Specific Growth and Dissolution Kinetics of Potassium Dihydrogen Phosphate Crystals from Batch Crystallization Experiments. *Cryst. Growth Des.* **2015**, *15*, 219–227.
- (18) Huo, Y.; Liu, T.; Yang, Y.; Ma, C. Y.; Wang, X. Z.; Ni, X. In Situ Measurement of 3D Crystal Size Distribution by Double-View Image Analysis with Case Study on L-Glutamic Acid Crystallization. *Ind. Eng. Chem. Res.* **2020**, *59*, 4646–4658.
- (19) Schorsch, S.; Ochsenbein, D. R.; Vetter, T.; Morari, M.; Mazzotti, M. High accuracy online measurement of multidimensional particle size distributions during crystallization. *Chem. Eng. Sci.* **2014**, *105*, 155–168.
- (20) Kovačević, T.; Reinhold, A.; Briesen, H. Identifying Faceted Crystal Shape from Three-Dimensional Tomography Data. *Cryst. Growth Des.* **2014**, *14*, 1666–1675.
- (21) Kovačević, T.; Schock, J.; Pfeiffer, F.; Briesen, H. Shape Identification of Primary Particles in Potash Alum Aggregates Using Three-Dimensional Tomography Data. *Cryst. Growth Des.* **2016**, *16*, 2685–2699.
- (22) Schneider, R. *Convex Bodies: The Brunn–Minkowski Theory*, 2nd ed.; Cambridge University Press, 2013.
- (23) Reinhold, A.; Briesen, H. High dimensional population balances for the growth of faceted crystals: Combining Monte Carlo integral estimates and the method of characteristics. *Chem. Eng. Sci.* **2015**, *127*, 220–229.
- (24) Schiele, S.; Kovačević, T.; Briesen, H. Morphological Modelling and Simulation of Crystallization Processes. In *Dynamic Flowsheet Simulation of Solids Processes*; Heinrich, S., Ed.; Springer International Publishing, 2020; pp 435–473.
- (25) Zhang, Y.; Doherty, M. F. Simultaneous prediction of crystal shape and size for solution crystallization. *AIChE J.* **2004**, *50*, 2101–2112.
- (26) Ma, C. Y.; Roberts, K. J. Morphological population balance modelling of the effect of crystallisation environment on the evolution of crystal size and shape of para-aminobenzoic acid. *Comput. Chem. Eng.* **2019**, *126*, 356–370.
- (27) Schiele, S. A.; Antoni, F.; Meinhardt, R.; Briesen, H. Analysis of Nonideal Shape Evolution during Potash Alum Crystallization Using Microcomputed Tomography and Three-Dimensional Image Analysis. *Cryst. Growth Des.* **2021**, *21*, 1751–1761.
- (28) Briesen, H. Model-based analysis of the effect of particle and impact geometry on attrition of brittle material. *Powder Technol.* **2007**, *178*, 87–98.
- (29) Gahn, C.; Mersmann, A. Brittle fracture in crystallization processes Part A. Attrition and abrasion of brittle solids. *Chem. Eng. Sci.* **1999**, *54*, 1273–1282.
- (30) Szilágyi, B.; Lakatos, B. G. Model-based analysis of stirred cooling crystallizer of high aspect ratio crystals with linear and nonlinear breakage. *Comput. Chem. Eng.* **2017**, *98*, 180–196.
- (31) Gahn, C.; Mersmann, A. Brittle fracture in crystallization processes Part B. Growth of fragments and scale-up of suspension crystallizers. *Chem. Eng. Sci.* **1999**, *54*, 1283–1292.
- (32) Ulrich, J.; Stepanski, M. Einfluß der Oberflächen-Beschaffenheit auf das Kristallwachstum aus Lösungen. *Chem. Ing. Tech.* **1987**, *59*, 402–404.
- (33) Prajapati, N.; Späth, M.; Knecht, L.; Selzer, M.; Nestler, B. Quantitative Phase-Field Modeling of Faceted Crystal Dissolution Processes. *Cryst. Growth Des.* **2021**, *21*, 3266–3279.
- (34) Roy, A.; Gururajan, M. P. Phase Field Modelling of Morphologies Driven by Tetragonal Interfacial Energy Anisotropy. *Cryst. Growth Des.* **2021**, *21*, 1591–1603.
- (35) Nani, E. S.; Gururajan, M. P. On the incorporation of cubic and hexagonal interfacial energy anisotropy in phase field models using higher order tensor terms. *Philos. Mag.* **2014**, *94*, 3331–3352.
- (36) Kovačević, T.; Wiedmeyer, V.; Schock, J.; Voigt, A.; Pfeiffer, F.; Sundmacher, K.; Briesen, H. Disorientation angle distribution of primary particles in potash alum aggregates. *J. Cryst. Growth* **2017**, *467*, 93–106.
- (37) Mullin, J. W.; Garside, J. The crystallization of aluminium potassium sulphate: A study in the assessment of crystallizer design data Part I: Single crystal growth rates. *Trans. Inst. Chem. Eng.* **1967**, *45*, 285–290.
- (38) Kroon, D.-J. Smooth Triangulated Mesh, 2021, <https://www.mathworks.com/matlabcentral/fileexchange/26710-smooth-triangulated-mesh> (accessed on February 20, 2020).
- (39) Desbrun, M.; Meyer, M.; Schröder, P.; Barr, A. H. In *Implicit Fairing of Irregular Meshes Using Diffusion and Curvature Flow*, SIGGRAPH '99: Proceedings of the 26th Annual Conference on Computer Graphics and Interactive Techniques, 1999; pp 317–324.
- (40) Zotkin, D. N.; Duraiswami, R.; Gumerov, N. A. In *Regularized HRTF Fitting Using Spherical Harmonics*, IEEE Workshop on Applications, 2009; pp 257–260.
- (41) Gorski, K. M.; Hivon, E.; Banday, A. J.; Wandelt, B. D.; Hansen, F. K.; Reinecke, M.; Bartelmann, M. HEALPix: A Framework for High-Resolution Discretization and Fast Analysis of Data Distributed on the Sphere. *Astrophys. J.* **2005**, *622*, 759–771.
- (42) Fokuda, K. *cddlib*; ETH Zürich. [https://people.inf.ethz.ch/fukudak/cdd\\_home](https://people.inf.ethz.ch/fukudak/cdd_home), 2012.
- (43) Snyder, R. C.; Doherty, M. F. Faceted crystal shape evolution during dissolution or growth. *AIChE J.* **2007**, *53*, 1337–1348.

(44) Klapper, H.; Becker, R. A.; Schmiemann, D.; Faber, A. Growth-Sector Boundaries and Growth-Rate Dispersion in Potassium Alum Crystals. *Cryst. Res. Technol.* **2002**, *37*, 747.

(45) Donnay, J. D. H.; Harker, D. A new law of crystal morphology extending the Law of Bravais. *Am. Mineral.* **1937**, *22*, 446–467.

(46) Ristic, R. I.; Shekunov, B.; Shewood, J. N. Long and short period growth rate variations in potash alum crystals. *J. Cryst. Growth* **1996**, *160*, 330–336.

(47) McDonald, M. A.; Bommarius, A. S.; Grover, M. A.; Rousseau, R. W. Direct Observation of Growth Rate Dispersion in the Enzymatic Reactive Crystallization of Ampicillin. *Processes* **2019**, *7*, No. 390.

## Chapter 6

### Discussion

Crystal shape analysis has emerged from crystal shape engineering. Research on 2D image analysis methods for crystallization analysis is ongoing. However, literature agrees (Nagy et al. 2013; Heisel et al. 2017) that there are inherent limitations to 2D imaging, even for quite simple geometries such as rounded (Reinhold et al. 2015), or plate-like crystals (Jaeggi et al. 2021). Therefore, the work of Reinhold (2015), Kovačević (2018) and the present thesis focus on the development of 3D methods. Challenges are that 3D imaging is much more complex and time consuming than 2D imaging. 3D images use memory in the order of gigabytes instead of megabytes in the case of 2D images. This makes 3D image analysis methods hardware demanding and time consuming. However, the great potential is that 3D images contain full shape information.

#### 6.1 3D methods for crystal population analysis

One goal of the present work was, therefore, to optimize the experimental methods of Kovačević (2018) in such a way that they became feasible for larger populations of crystals. Kovačević (2018) analyzed roughly 100 crystals. It is discussed by Schiele et al. (2021a) that at least 1000 particles should be analyzed for a reasonable population analysis. This number was based on a statistical analysis of a mono-disperse population and crystal size was used as disperse characteristic. For different types of populations (e.g. poly-disperse) and different or even multiple disperse characteristics (multi-dimensional populations) more or less particles may be necessary. For the presented study, this meant that the number of analyzed crystals had to be increased by a factor of at least 10 in order to analyze a single population. The aim was, to analyze the evolution of a population over time. Therefore, multiple samples had to be analyzed. In context of the present work, a method was developed that involved sorting crystals in 3D printed scaffolds. Like this, about 800 crystals could be visualized with one single  $\mu$ CT measurement. Using the new method, in total about 11 000 crystals were analyzed. Their sizes ranged between 200  $\mu$ m and 2 mm. Schiele et al. (2021a) showed that off-line crystal population analysis is feasible using the image analysis tools of Kovačević (2018) in combination with optimized experimental procedures. For a broader application of the presented techniques, two challenges are discussed in the following.

**Challenge 1: Crystals are handled manually.** This fact poses a few challenges. One is that user bias has to be taken into account and effort has to be taken to minimize it. In addition, the proposed sorting process is time consuming, tedious, and a steady hand of the user is essential.

More importantly, manual handling leads to a limitation in size. Schiele et al. (2021a) studied only crystals larger than 200  $\mu$ m. At the applied voxel spacing of 8  $\mu$ m this is also roughly the size that one can expect to be well analyzed by the tools of Kovačević (2018). However, higher resolutions can be achieved when longer measurement times and smaller fields of view are accepted, or more advanced  $\mu$ CTs are used (see below).

The limitation in size is especially limiting to the application in crystal population analysis, because small crystals dominate the behaviors of many crystallization processes. This is because, damage to crystals through agitation and secondary nucleation can usually not be avoided or are even intentionally introduced. Nucleation leads to a high number of small particles that all together provide a huge surface area for crystal growth. At the same time, larger crystals tend to have more ideal shapes because growth leads to healing of some non-idealities (Schiele et al. 2021a; Schiele et al. 2021b). The behavior

of ideally shaped crystals is quite well understood. Therefore, if the aim of crystal population analysis is to understand certain crystallization phenomena, the analysis of small, non-ideal crystals is most promising.

Further development of the proposed methods should aim at avoiding manual handling of single crystals. In some preliminary experiments, it was tried to visualize crystals in bulk. However, unlike e.g. fungi pellets (Schmideder et al. 2021), most crystals touched such that their faces were in planar contact. This made segmentation even harder and agglomerates and single crystals could not be distinguished. It will hence be important to distribute populations in the measured volume such that they do not touch.

**Challenge 2: 3D imaging and 3D image analysis are time consuming.** The time needed for population analysis can be divided in three parts

1. Sample preparation; i.e. taking a sample, filtering, washing, sorting crystals into scaffolds
2.  $\mu$ CT imaging
3. Image analysis

During sample preparation, the sorting step is the most time consuming. The other steps would also have to be applied in a similar way for other off-line analysis methods and are, therefore, not discussed here. Sorting 800 crystals for one  $\mu$ CT measurement took around one to two hours, depending on average crystal size. Small crystals are harder to handle and hence sorting needs more time for them. Other challenges of the manual handling have been discussed above.

Using the described settings,  $\mu$ CT imaging needs about 25 min per 3D image and crystals may not change or move during this time. 2D imaging may take only a few milliseconds. This is much faster than most physical phenomena in crystallization. This means that changing and even moving particles can be tracked using 2D imaging techniques. In addition, 2D image analysis methods are often rapid as well. High-end  $\mu$ CT devices that have more powerful x-ray sources than the one used in context of the present work may significantly reduce the time needed for one 3D image. For example, 3D imaging using synchrotron x-ray sources may take only half a second (Finegan et al. 2015) and can be used to track batteries' electrodes during operation (Finegan et al. 2016). The authors tracked the combustion of batteries due to high currents and high temperatures ("thermal runaway"); a process that takes a few minutes. In these studies, similar resolutions and image sizes similar to those in the present work were achieved. Using such equipment, one could imagine  $\mu$ CT as in-line technique for crystallization, provided crystals do not move, or move slowly. Segmentation of solvent and crystals may be a challenge in such cases. Zhou et al. (2019) used electron tomography to track the shape, size and lattice structure of nuclei in solid-solid phase transition at atomic resolution. In that work, segmentation was possible due to the high resolution that enabled segmentation based on the lattice structure. Segmentation of crystals and solvent may also be feasible using neutron tomography. For example, Gruber et al. (2020) tracked freeze-drying of sugars using neutron tomography. The authors used deuterium (heavy water) as solvent. This led to good contrasts between solvent and sugars. However, neutron imaging takes a few hours and is hence even slower than x-ray imaging.

Using the current algorithms and data storages, analysis of a single crystal takes a few seconds. For high numbers of crystals to be analyzed, this may also become a limiting step. For example, the analysis of the crystals in the work of Schiele et al. (2021a) took several days on a standard desktop computer. The algorithms are not optimized for speed. Implementation in faster programming languages like C/C++ or Fortran and parallel computing could reduce calculation times. In addition, storage of the image files on fast drives (e.g. solid-state drives) instead of hard disk drives or even network drives would also increase the speed of 3D image analysis. However, in context of this work, calculation times did not limit the analysis.

In conclusion, the manual sample handling appears as the main challenge for a broader application of 3D imaging. However, 3D imaging has proven itself as a valuable tool for crystal population analysis and can be used for detailed shape analysis. In the studied process (Schiele et al. 2021a), symmetry of single crystals was tracked over time. In addition, the analysis of over 1000 crystal agglomerates corroborated the results of Kovačević et al. (2017) at higher statistical relevance. Both the single crystal symmetry and analysis of agglomerates would have been very hard—if not impossible—using 2D methods. We have learnt that

- crystals undergo a shape transition, even if face independent growth occurs and
- potash alum agglomerates have low disorientation angles

## 6.2 Studying interaction of crystallization phenomena

Using the discussed 3D population analysis, unexpected crystal shapes were observed. Schiele et al. (2021a) discuss that non-ideal shapes may be the result of damaged seed material. This motivated the work of Schiele et al. (2021b) who developed a method to track growth of individual crystals using  $\mu$ CT. The method was applied to study growth of abraded potash alum crystals. Even though the method was so far only applied to study the interaction of growth and abrasion, it is discussed below that it may also be promising for studying other crystallization phenomena as well.

### 6.2.1 Abrasion and Growth

Abraded crystals were fixed to racks for crystal growth and  $\mu$ CT imaging. Alternating growth and imaging yielded 3D images of the same crystals during different states of their growth. Like this, it was tracked how the initially round abraded crystals became faceted. Using the 3D images, growth rates were derived and used to parametrize a high dimensional crystal growth model. The growth model describes the shape and size evolution of abraded crystals through growth. It was shown that the initial shapes were decisive for the shape and volume evolution. Simulations confirmed that the non-ideal shapes observed by Schiele et al. (2021a) could result from damaged seed material.

From a more general perspective, depletion of supersaturation can be increased through abrasion in a process. The established theory explains fast depletion of supersaturation through an increased surface area for crystal growth through the creation of numerous small fragments (Bosetti and Mazzotti 2019). However, literature agrees that crystalline surface area alone is not sufficient to describe depletion of supersaturation. For example, growth rate dispersion (GRD) describes the observation that similar crystals grow at different rates. This may even apply to the same crystal that grows at a varying rate. GRD is often attributed to increased strain and number of defects in the lattice caused by damage or inclusion of impurities (Ristic et al. 1996; McDonald et al. 2019). Hence, e.g. damaged crystals may grow at increased rates until defects are healed. In addition, there is size dependent growth (SDG), which describes different apparent growth rates for differently sized crystals. This effect may be explained by size dependent hydrodynamic conditions. Mullin (2001) describes that crystals smaller than 10  $\mu\text{m}$  may follow turbulent eddies. Therefore, they may be growing in stagnant solution even if the suspension is well agitated. In consequence, small crystals may grow slowly under diffusion limited conditions, while growth of large ones may be integration limited and faster (Mullin and Garside 1967b). SDG may also be caused by size dependent damage to crystals. It is generally accepted that large crystals are rather subject to abrasion than small crystals (Gahn and Mersmann 1999a). Hence large crystals would rather suffer from GRD leading to SDG (Mullin 2001).

While these effects will most certainly play an important role, the work of Schiele et al. (2021b) shows that the magnitude of surface area, GRD and SDG are still not sufficient to accurately describe depletion of supersaturation. Schiele et al. (2021b) measured that abraded surfaces grow much faster than ideal crystal faces. It is explained that through

abrasion highly indexed faces—that are known to generally grow faster (Mullin 2001)—are exposed. This leads to faster increase in volume that has been observed in other studies (Ulrich and Stepanski 1987). Traditional analysis methods are usually not able to detect non-ideal shapes and such shapes were hence not considered in the past. In conclusion, instead of GRD or SDG, variations in growth rates may in fact be shape-dependent growth in some cases. Even though the herein developed methods were only applied to large crystals (diameter >0.5 mm), it is likely that smaller fragments would grow at increased rates too. That is, provided no diffusion limitation occurs. These results further emphasize that non-ideal crystal shape is an important process variable that can be tracked using 3D imaging.

So far, the measurements and simulations were only applied to single crystals. In order to evaluate the effect of non-ideal crystal surfaces on processes, a modelling approach may be chosen. Population balance modelling has emerged as a powerful tool for crystallization process modelling (Marchisio et al. 2003; Qamar et al. 2007; Aamir et al. 2009; Borchert et al. 2014; Bosetti and Mazzotti 2019; Kovačević and Briesen 2019; Ma and Roberts 2019). In such models, crystal shape has to be simplified in order to describe crystals by one or two measures. Higher dimensional models are possible but compromises at complexity of a modeled process have to be accepted in such cases (Reinhold and Briesen 2015; Ma and Roberts 2019). Briesen (2009) studied the effect of crystal shape on crystal attrition using population balance modelling. In that study, growth was considered but was assumed to have no effect of crystal shape. Schiele et al. (2021b) have shown that this is inaccurate.

In future work, one could use the rates determined by Schiele et al. (2021b) to evaluate the effect of growth on crystal shape using a multi-scale approach. Similar to the work of Kovačević and Briesen (2019), one could simulate the growth of multiple differently shaped crystals and derive rates for PBM modelling that account for the effect of shape on growth and vice versa. These rates could be included in the model of Briesen (2009). This would yield a model that considers interaction between crystal growth and abrasion under full consideration of crystal shape. That is, the effects of

- crystal growth on shape,
- shape on crystal growth,
- shape on abrasion,
- and abrasion on shape

would be considered. This concept is also similar to the work of Ma and Roberts (2019) who studied the effect of breakage on crystallization under consideration of crystal shape. However, the rates used for simulations were neither experimentally determined nor validated. In addition, similarly to Briesen (2009), shape was not considered to affect all phenomena. Ma and Roberts (2019) only considered the effect of growth on shape and shape on growth. For breakage, no shape influence was considered.

### **6.2.2 Breakage and Growth**

Considering crystal breakage, it would be highly interesting to apply the methods of Schiele et al. (2021b) to broken or ground crystals. Breakage is a phenomenon that may be deliberately introduced in processes in order to control crystal size (Salvatori and Mazzotti 2018; Hill and Reeves 2019) or may unintentionally occur during e.g. agitation. In addition, seed crystals may be broken from pre-processing (e.g. conveying, sieving, grinding). Broken crystals may be concave. For studying growth of concave crystals using  $\mu$ CT, some challenges must be overcome. The method of Schiele et al. (2021b) is based on convex geometry. Kovačević and Briesen (2019) developed methods to apply similar geometric methods to agglomerates (i.e. concave particles). However, in that case, agglomerates could be described through small numbers of convex crystal models. Broken crystals would likely be less regular and not so easily approximated by small numbers of convex crystals. In addition, breakage may yield many small fragments

of a crystal. Therefore, the size limitation of the measurements (>0.5 mm) that is discussed by Schiele et al. (2021b) must be tackled.

### 6.2.3 Dissolution and Growth

Models usually consider dissolution as inverse growth. That is, expressed faces are modeled to be displaced towards the crystals' center of mass. Inverse growth corresponds to the assumption that crystals remain faceted during dissolution. Snyder and Doherty (2007) consider that other faces may appear. This results from the idea that these faces are observed to grow faster and are, therefore, assumed to have lower solubility. However, the images presented by Eisenschmidt et al. (2016) and simulation results (Elts et al. 2016, 2017) suggest that crystals become round through dissolution. Still, rounding was not considered by Eisenschmidt et al. (2016). In the literature, dissolution of crystals is discussed from three perspectives

- In context of controlled drug release it is discussed that different polymorphs have different dissolution behavior and lead to different bioavailability (Blagden et al. 2007; Tung 2012; Reischl et al. 2015; Amrutha et al. 2020).
- Partial dissolution can be applied to reduce the fraction of fines in a process (Schmalenberg et al. 2021; Binel and Mazzotti 2021).
- Dissolution is applied in combination with growth for shape control (Snyder et al. 2007; Eisenschmidt et al. 2016).

For controlled drug release, a change in concentration in the dissolving solvent, which can be calculated from the change in overall crystal volume, is of importance. For shape control and reduction of fines, the shape of crystals would also have to be tracked in order to describe an initial condition for subsequent growth (Schiele et al. 2021b). Both, a change in volume and shape could be well modeled with a similar model as the one proposed by Schiele et al. (2021b). Corresponding simulations could quantify how edges and corners dissolve faster than faces to yield round crystals. For parametrization of the model the same experiments could be conducted. A challenge may be that crystals could detach from the racks through dissolution. Detachment may be fought by adhering crystals to racks, growing them to a certain size and then performing dissolution experiments until they reached their original size.

Besides dissolution behavior, growth behavior of crystals that previously partially dissolved would be essential for shape control and reduction of fines, too. Consequently, growth of partially dissolved crystals could be studied in the same way as it was done for abraded crystals. This would then give information on how such round crystals grow. A comparison of growth of round crystals that were produced through abrasion and such ones that were produced through partial dissolution would be highly interesting. Some experiments suggest that internal strain leads to increased growth rates (Ristic et al. 1996; McDonald et al. 2019). It is plausible that abraded crystals would have more internal stain than partially dissolved ones.

### 6.2.4 Ostwald ripening

Another interesting effect related to the present work is discussed by Garside and Davey (1980): Ostwald ripening. It was initially described for vapor droplets. Due to surface tension, small droplets have a higher pressure inside (Laplace pressure, described by Kelvin equation) and, therefore, solubility of droplets is size dependent. Diffusion leads to shrinkage of small droplets and growth of larger droplets. Ostwald ripening is well understood for isotropic, spherical droplets. Also an extension to faceted crystals is quite straightforward but leads to the conclusion that it should only be relevant for very small (<1  $\mu\text{m}$ ) crystals (Garside and Davey 1980). This contradicts experimental observations (Mullin 1976). More recently, Bosetti and Mazzotti (2019) have studied which effect Ostwald ripening would have on crystal populations. In context of the present work, crystal growth was measured for anisotropic surfaces of crystals. Such direction dependent crystal growth can also be connected to anisotropic surface energy.

It is, therefore, plausible that nuclei—that are usually not faceted (Zhou et al. 2019)—and non-ideal small crystals would have increased and anisotropic surface energies compared to those assumed by Garside and Davey (1980). This would again lead to a more pronounced Ostwald ripening even for crystals larger than 1  $\mu\text{m}$ . Spinning the wheel even further, anisotropic surface energy might even lead to anisotropic solubility of a crystal (i.e. face-dependent growth). In order to converge towards minimal surface energy, it would be plausible if crystals would undergo a shape transition such that damaged regions with high surface energy would disappear in favor of more stable surfaces. In precipitation processes for pigments, crystals are left in saturated suspension for so called annealing, aging or ripening phases (Myerson et al. 2019, 476ff). During this time, such effects may play a role. In addition, pigment quality depends on crystal shape. In order to study crystal shape and shape transition, tomography seems like the ideal tool. It is able to track crystal shape accurately and in three dimensions. Also relatively long imaging times would not be a problem because ripening is described to take many hours. High resolutions would be needed in order to image particles around 1  $\mu\text{m}$  in size. Using suitable tomography methods crystals can be tracked even at atomic resolution (Zhou et al. 2019).

## Chapter 7

### Conclusion

It is long accepted that crystal shape is an important process variable and crystal property. In the literature, ideal shapes are usually assumed. Crystals are then often inaccurately described by their faces only. One reason for that may be the lack of appropriate quantitative analysis methods. State of the art shape analysis is done using 2D imaging. It is discussed above that 2D imaging is not able to capture the exact shape of crystals due to its low dimensionality. Facetted shape models are used to extract meaningful information from 2D images. Therefore, non-ideal shapes are exceptionally hard to analyze.

Crystals approach ideal shapes through growth. However, in most applications not only growth occurs. Crystals nucleate, agglomerate and are damaged. These effects lead to non-ideal shapes that do not grow according to established growth laws. Accurate shape description under consideration of non-ideal shapes is, therefore, key to understanding the dynamic interactions of these crystallization phenomena. In recent work (Kovačević 2018), 3D imaging was established as new tool for more accurate crystal shape analysis. It was applied to understand the interaction of growth and agglomeration (Kovačević et al. 2017; Kovačević and Briesen 2019). The present work further explored the application of 3D imaging as a tool for crystal shape analysis. The aim was to understand the interaction of crystal growth and damaging events.

In a first step, 3D imaging was applied to analyze the evolution of crystal populations during a crystallization process. This analysis was enabled by developing new 3D imaging methods. The number of crystals that can be imaged was increased by a factor of about 100. Using this new method, it was tracked how non-ideally shaped (i.e. damaged and asymmetrical) seed material quickly grew to facetted but still unexpectedly asymmetric crystals. Crystals became more symmetric over time but still mostly remained asymmetric. It was discussed that the shape of seed material has decisive influence on the shape of the product crystals. However, the mechanisms remained in the dark. This motivated the second study in which new 3D imaging and 3D image analysis methods were developed and enabled to track growth of abraded crystals. The results were used to parametrize a growth model that describes the shape and size evolution of abraded crystals. In conclusion, in order to describe crystal growth accurate shape description is important in processes where either non-ideal seed material is used or abrasion occurs.

From a broader perspective, it was demonstrated that 3D imaging is an invaluable tool for detailed crystal shape analysis. Methods to analyze crystal populations and single crystals were presented and yielded detailed size and shape information. The new methods were applied to study the interaction of growth and abrasion. It is discussed that such methods are also highly promising for understanding the role of non-ideal shape in other interacting crystallization phenomena. For example, the application to the interactions of dissolution or breakage and growth would be highly interesting and fairly straightforward using the new methods. The main challenge for even further application of the methods lies in the manual handling of crystals, which leads to a limitation in crystal size to roughly 200  $\mu\text{m}$ . Many interesting phenomena happen at nanometer and molecular/atomic size scales. Therefore, lowering the 200  $\mu\text{m}$  barrier would enable interesting insights in further crystallization phenomena and their interactions. Modern 3D imaging methods are able to visualize crystals on molecular level and in 3D.

Another valuable tool to understanding process behavior and the interaction of crystallization phenomena is population balance modelling. Such models track the

evolution of disperse particle properties. This work has demonstrated that the classical crystal faces cannot describe crystal shape when considering growth and abrasion. A population balance modelling approach may be chosen to explore the influence of non-ideal crystal shapes on process behavior. The results of this study will help in choosing appropriate crystal description and to parametrize a corresponding model.

## Literature

Aamir, E.; Nagy, Z. K.; Rielly, C. D. (2010): Optimal seed recipe design for crystal size distribution control for batch cooling crystallisation processes. In *Chemical Engineering Science* 65 (11), pp. 3602–3614. DOI: 10.1016/j.ces.2010.02.051.

Aamir, E.; Nagy, Z. K.; Rielly, C. D.; Kleinert, T.; Judat, B. (2009): Combined Quadrature Method of Moments and Method of Characteristics Approach for Efficient Solution of Population Balance Models for Dynamic Modeling and Crystal Size Distribution Control of Crystallization Processes. In *Industrial & Engineering Chemistry Research* 48 (18), pp. 8575–8584. DOI: 10.1021/ie900430t.

Agimelen, Okpeafoh S.; Svoboda, Vaclav; Ahmed, Bilal; Cardona, Javier; Dziejewicz, Jerzy; Brown, Cameron J. et al. (2018): Multi-sensor inline measurements of crystal size and shape distributions during high shear wet milling of crystal slurries. In *Advanced Powder Technology*. DOI: 10.1016/j.appt.2018.09.003.

Ahn, Byeongho; Bosetti, Luca; Mazzotti, Marco (2021a): Accounting for the Presence of Molecular Clusters in Modeling and Interpreting Nucleation and Growth. In *Crystal Growth & Design*. DOI: 10.1021/acs.cgd.1c01193.

Ahn, Byeongho; Bosetti, Luca; Mazzotti, Marco (2021b): Secondary Nucleation by Interparticle Energies. II. Kinetics. In *Crystal Growth & Design*. DOI: 10.1021/acs.cgd.1c00928.

Alvarez Rodrigo, Angela; Lorenz, Heike; Seidel-Morgenstern, Andreas (2004): Online monitoring of preferential crystallization of enantiomers. In *Chirality* 16 (8), pp. 499–508. DOI: 10.1002/chir.20067.

Amrutha, S.; Giri, Lopamudra; SeethaLekshmi, Sunil; Varughese, Sunil (2020): Enhanced Aqueous Solubility of the Solid Forms of a BCS Class-II Anti-Tuberculosis Drug, Prothionamide. In *Crystal Growth & Design* 20 (8), pp. 5086–5096. DOI: 10.1021/acs.cgd.0c00266.

Beck, Ralf; Andreassen, Jens-Petter (2012): Influence of crystallization conditions on crystal morphology and size of CaCO<sub>3</sub> and their effect on pressure filtration. In *AIChE Journal* 58 (1), pp. 107–121. DOI: 10.1002/aic.12566.

Beckmann, Wolfgang (2000): Seeding the Desired Polymorph: Background, Possibilities, Limitations, and Case Studies. In *Org. Process Res. Dev.* 4 (5), pp. 372–383. DOI: 10.1021/op0000778.

Binel, Pietro; Mazzotti, Marco (2021): Selective Dissolution Process Featuring a Classification Device for the Removal of Fines in Crystallization: Experiments. In *Ind. Eng. Chem. Res.* 60 (43), pp. 15752–15765. DOI: 10.1021/acs.iecr.1c03401.

Blagden, N.; Matas, M. de; Gavan, P. T.; York, P. (2007): Crystal engineering of active pharmaceutical ingredients to improve solubility and dissolution rates. In *Adv. Drug Delivery Rev.* 59 (7), pp. 617–630. DOI: 10.1016/j.addr.2007.05.011.

Borchert, Christian; Sundmacher, Kai (2012): Morphology evolution of crystal populations. Modeling and observation analysis. In *Chem. Eng. Sci.* 70, pp. 87–98. DOI: 10.1016/j.ces.2011.05.057.

Borchert, Christian; Temmel, Erik; Eisenschmidt, Holger; Lorenz, Heike; Seidel-Morgenstern, Andreas; Sundmacher, Kai (2014): Image-Based in Situ Identification of Face Specific Crystal Growth Rates from Crystal Populations. In *Cryst. Growth Des.* 14 (3), pp. 952–971. DOI: 10.1021/cg401098x.

- Bosetti, Luca; Ahn, Byeongho; Mazzotti, Marco (2021): Secondary Nucleation by Interparticle Energies. I. Thermodynamics. In *Crystal Growth & Design*. DOI: 10.1021/acs.cgd.1c00927.
- Bosetti, Luca; Mazzotti, Marco (2019): Population Balance Modeling of Growth and Secondary Nucleation by Attrition and Ripening. In *Crystal Growth & Design* 20 (1), pp. 307–319. DOI: 10.1021/acs.cgd.9b01240.
- Bötschi, Stefan (2019): Optimization and Feedback Control of the Size and Shape Evolution of Elongated Crystals in Suspension. Zurich, E. T.H., <https://www.research-collection.ethz.ch/handle/20.500.11850/375357>.
- Bötschi, Stefan; Rajagopalan, Ashwin Kumar; Rombaut, Igor; Morari, Manfred; Mazzotti, Marco (2019): From needle-like toward equant particles. A controlled crystal shape engineering pathway. In *Comput. Chem. Eng.* 131. DOI: 10.1016/j.compchemeng.2019.106581.
- Briesen, Heiko (2006): Simulation of crystal size and shape by means of a reduced two-dimensional population balance model. In *Chemical Engineering Science* 61 (1), pp. 104–112. DOI: 10.1016/j.ces.2004.11.062.
- Briesen, Heiko (2007): Model-based analysis of the effect of particle and impact geometry on attrition of brittle material. In *Powder Technol.* 178 (2), pp. 87–98. DOI: 10.1016/j.powtec.2007.04.011.
- Briesen, Heiko (2009): Two-dimensional population balance modeling for shape dependent crystal attrition. In *Chem. Eng. Sci.* 64 (4), pp. 661–672.
- Buffham, B. A. (2000): The size and compactness of particles of arbitrary shape. application to catalyst effectiveness factors. In *Chemical Engineering Science* 55 (23), pp. 5803–5811. DOI: 10.1016/s0009-2509(00)00425-5.
- Chung, Serena H.; Ma, David L.; Braatz, Richard D. (1999): Optimal seeding in batch crystallization. In *The Canadian Journal of Chemical Engineering* 77 (3), pp. 590–596. DOI: 10.1002/cjce.5450770322.
- Cornehl, Bianca; Overbeck, Achim; Schwab, Annika; Büser, Jan-Philipp; Kwade, Arno; Nirschl, Hermann (2014): Breakage of lysozyme crystals due to compressive stresses during cake filtration. In *Chemical Engineering Science* 111, pp. 324–334. DOI: 10.1016/j.ces.2014.02.016.
- Dandekar, Preshit; Kuvadia, Zubin B.; Doherty, Michael F. (2013): Engineering Crystal Morphology. In *Annu. Rev. Mater. Res.* 43 (1), pp. 359–386. DOI: 10.1146/annurev-matsci-071312-121623.
- Eder, Cornelia; Briesen, Heiko (2019): Impedance spectroscopy as a process analytical technology (PAT) tool for online monitoring of sucrose crystallization. In *Food Control* 101, pp. 251–260. DOI: 10.1016/j.foodcont.2019.02.005.
- Eisenschmidt, H.; Voigt, A.; Sundmacher, K. (2014): Face-Specific Growth and Dissolution Kinetics of Potassium Dihydrogen Phosphate Crystals from Batch Crystallization Experiments. In *Cryst. Growth Des.* 15 (1), pp. 219–227. DOI: 10.1021/cg501251e.
- Eisenschmidt, Holger; Bajcinca, Naim; Sundmacher, Kai (2016): Optimal Control of Crystal Shapes in Batch Crystallization Experiments by Growth-Dissolution Cycles. In *Cryst. Growth Des.* 16 (6), pp. 3297–3306. DOI: 10.1021/acs.cgd.6b00288.
- Eltis, Ekaterina; Greiner, Maximilian; Briesen, Heiko (2016): Predicting Dissolution Kinetics for Active Pharmaceutical Ingredients on the Basis of Their Molecular Structures. In *Crystal Growth & Design* 16 (7), pp. 4154–4164. DOI: 10.1021/acs.cgd.6b00721.

- Eltis, Ekaterina; Greiner, Maximilian; Briesen, Heiko (2017): In Silico Prediction of Growth and Dissolution Rates for Organic Molecular Crystals: A Multiscale Approach. In *Crystals* 7 (10), p. 288. DOI: 10.3390/cryst7100288.
- Erdemir, Deniz; Lee, Alfred Y.; Myerson, Allan S. (2009): Nucleation of crystals from solution: classical and two-step models. In *Accounts of chemical research* 42 (5), pp. 621–629. DOI: 10.1021/ar800217x.
- Finegan, Donal P.; Scheel, Mario; Robinson, James B.; Tjaden, Bernhard; Hunt, Ian; Mason, Thomas J. et al. (2015): In-operando high-speed tomography of lithium-ion batteries during thermal runaway. In *Nat Commun* 6 (1), p. 6924. DOI: 10.1038/ncomms7924.
- Finegan, Donal P.; Tudisco, Erika; Scheel, Mario; Robinson, James B.; Taiwo, Oluwadamilola O.; Eastwood, David S. et al. (2016): Quantifying Bulk Electrode Strain and Material Displacement within Lithium Batteries via High-Speed Operando Tomography and Digital Volume Correlation. In *Adv. Sci.* 3 (3), p. 1500332. DOI: 10.1002/advs.201500332.
- Fokin, Vladimir M.; Zanutto, Edgar D. (2000): Crystal nucleation in silicate glasses: the temperature and size dependence of crystal/liquid surface energy. In *Journal of Non-Crystalline Solids* 265 (1-2), pp. 105–112. DOI: 10.1016/S0022-3093(99)00877-7.
- Gahn, C.; Mersmann, A. (1999a): Brittle fracture in crystallization processes Part A. Attrition and abrasion of brittle solids. In *Chem. Eng. Sci.* 54 (9), pp. 1273–1282. DOI: 10.1016/S0009-2509(98)00450-3.
- Gahn, C.; Mersmann, A. (1999b): Brittle fracture in crystallization processes Part B. Growth of fragments and scale-up of suspension crystallizers. In *Chem. Eng. Sci.* 54 (9), pp. 1283–1292. DOI: 10.1016/S0009-2509(98)00452-7.
- Garside, J.; Ristić, R. I. (1983): Growth rate dispersion among ADP crystals formed by primary nucleation. In *Journal of Crystal Growth* 61 (2), pp. 215–220. DOI: 10.1016/0022-0248(83)90357-3.
- Garside, John; Davey, Roger J. (1980): Secondary Contact Nucleation. Kinetics, Growth and Scale-Up. In *Chemical Engineering Communications* 4 (4-5), pp. 393–424. DOI: 10.1080/00986448008935918.
- Gruber, S.; Vorhauer, N.; Schulz, M.; Hilmer, M.; Peters, J.; Tsotsas, E.; Foerst, P. (2020): Estimation of the local sublimation front velocities from neutron radiography and tomography of particulate matter. In *Chemical Engineering Science* 211, p. 115268. DOI: 10.1016/j.ces.2019.115268.
- Guu, Mike Y. K.; Zall, Robert R. (1991): Lactose crystallization. effects of minerals and seeding. In *Process Biochemistry* 26 (3), pp. 167–172. DOI: 10.1016/0032-9592(91)80013-f.
- Heinrich, Stefan (Ed.) (2020): Dynamic Flowsheet Simulation of Solids Processes. Cham: Springer International Publishing.
- Heisel, Stefan; Kovačević, Tijana; Briesen, Heiko; Schembecker, Gerhard; Wohlgemuth, Kerstin (2017): Variable selection and training set design for particle classification using a linear and a non-linear classifier. In *Chemical Engineering Science* 173, pp. 131–144. DOI: 10.1016/j.ces.2017.07.030.
- Hill, Priscilla J. (2004): Statistics of multiple particle breakage accounting for particle shape. In *AIChE J.* 50 (5), pp. 937–952. DOI: 10.1002/aic.10091.
- Hill, Priscilla J.; Reeves, Sheena M. (2019): Effect of particle breakage conditions on child particle aspect ratio. In *Powder Technol.* 355, pp. 564–572. DOI: 10.1016/j.powtec.2019.07.068.

Huo, Yan; Liu, Tao; Yang, Yixuan; Ma, Cai Y.; Wang, Xue Z.; Ni, Xiongwei (2020): In Situ Measurement of 3D Crystal Size Distribution by Double-View Image Analysis with Case Study on L-Glutamic Acid Crystallization. In *Ind. Eng. Chem. Res.* 59 (10), pp. 4646–4658. DOI: 10.1021/acs.iecr.9b05828.

Jaeggi, Anna; Rajagopalan, Ashwin Kumar; Morari, Manfred; Mazzotti, Marco (2021): Characterizing Ensembles of Platelike Particles via Machine Learning. In *Ind. Eng. Chem. Res.* 60 (1), pp. 473–483. DOI: 10.1021/acs.iecr.0c04662.

Kail, Norbert; Briesen, Heiko; Marquardt, Wolfgang (2007): Advanced Geometrical Modeling of Focused Beam Reflectance Measurements (FBRM). In *Particle & Particle Systems Characterization* 24 (3), pp. 184–192. DOI: 10.1002/ppsc.200601036.

Kashchiev, D.; Vekilov, P. G.; Kolomeisky, A. B. (2005): Kinetics of two-step nucleation of crystals. In *J Chem Phys* 122 (24), p. 244706. DOI: 10.1063/1.1943389.

Kelton, K. F.; Greer, A. L. (2010): Heterogeneous Nucleation. In : Nucleation in Condensed Matter - Applications in Materials and Biology (Pergamon Materials Series), pp. 165–226.

Kempkes, Michel; Eggers, Jan; Mazzotti, Marco (2008): Measurement of particle size and shape by FBRM and in situ microscopy. In *Chemical Engineering Science* 63 (19), pp. 4656–4675. DOI: 10.1016/j.ces.2007.10.030.

Kovačević, Tijana (2018): Crystal Shape Characterization: From Single Crystals to Crystal Aggregates. Charakterisierung der Kristallform: Vom Einzelkristall zum Kristallaggregat. Dissertation. TU Munich, Freising, Germany. Fakultät Wissenschaftszentrum Weihenstephan. Available online at <https://mediatum.ub.tum.de/1398050>, checked on 9/8/2021.

Kovačević, Tijana; Briesen, Heiko (2019): Simulations of crystal aggregation and growth. Towards correct crystal area. In *AIChE J.* 65 (5). DOI: 10.1002/aic.16525.

Kovačević, Tijana; Reinhold, Alexander; Briesen, Heiko (2014): Identifying Faceted Crystal Shape from Three-Dimensional Tomography Data. In *Cryst. Growth Des.* 14 (4), pp. 1666–1675. DOI: 10.1021/cg401780p.

Kovačević, Tijana; Schock, Jonathan; Pfeiffer, Franz; Briesen, Heiko (2016): Shape Identification of Primary Particles in Potash Alum Aggregates Using Three-Dimensional Tomography Data. In *Cryst. Growth Des.* 16 (5), pp. 2685–2699. DOI: 10.1021/acs.cgd.5b01806.

Kovačević, Tijana; Wiedmeyer, Viktoria; Schock, Jonathan; Voigt, Andreas; Pfeiffer, Franz; Sundmacher, Kai; Briesen, Heiko (2017): Disorientation angle distribution of primary particles in potash alum aggregates. In *J. Cryst. Growth* 467, pp. 93–106. DOI: 10.1016/j.jcrysgro.2017.03.026.

Kulikov, Viatcheslav; Briesen, Heiko; Grosch, Robert; Yang, Aidong; Wedel, Lars von; Marquardt, Wolfgang (2005): Modular dynamic simulation for integrated particulate processes by means of tool integration. In *Chemical Engineering Science* 60 (7), pp. 2069–2083. DOI: 10.1016/j.ces.2004.11.037.

Larsen, P. A.; Rawlings, J. B.; Ferrier, N. J. (2007): Model-based object recognition to measure crystal size and shape distributions from in situ video images. In *Chemical Engineering Science* 62 (5), pp. 1430–1441. DOI: 10.1016/j.ces.2006.11.018.

Lovette, Michael A.; Browning, Andrea Robben; Griffin, Derek W.; Sizemore, Jacob P.; Snyder, Ryan C.; Doherty, Michael F. (2008): Crystal Shape Engineering. In *Ind. Eng. Chem. Res.* 47 (24), pp. 9812–9833. DOI: 10.1021/ie800900f.

Ma, Cai Y.; Roberts, Kevin J. (2019): Morphological population balance modelling of the effect of crystallisation environment on the evolution of crystal size and shape of

- para-aminobenzoic acid. In *Comput. Chem. Eng.* 126, pp. 356–370. DOI: 10.1016/j.compchemeng.2019.04.019.
- Ma, Cai Y.; Wan, Jian; Wang, Xue Z. (2012): Faceted growth rate estimation of potash alum crystals grown from solution in a hot-stage reactor. In *Powder Technol.* 227, pp. 96–103. DOI: 10.1016/j.powtec.2012.02.040.
- Ma, Cai Y.; Wang, Xue Z. (2008): Crystal growth rate dispersion modeling using morphological population balance. In *AIChE Journal* 54 (9), pp. 2321–2334. DOI: 10.1002/aic.11549.
- Ma, Cai Y.; Wang, Xue Z.; Roberts, Kevin J. (2008): Morphological population balance for modeling crystal growth in face directions. In *AIChE J.* 54 (1), pp. 209–222. DOI: 10.1002/aic.11365.
- Marchisio, Daniele L.; Pikturna, Jesse T.; Fox, Rodney O.; Vigil, R. Dennis; Barresi, Antonello A. (2003): Quadrature method of moments for population-balance equations. In *AIChE J.* 49 (5), pp. 1266–1276. DOI: 10.1002/aic.690490517.
- McDonald, Matthew A.; Bommarius, Andreas S.; Grover, Martha A.; Rousseau, Ronald W. (2019): Direct Observation of Growth Rate Dispersion in the Enzymatic Reactive Crystallization of Ampicillin. In *Processes* 7 (6), p. 390. DOI: 10.3390/pr7060390.
- McLeod, J.; Paterson, A. H. J.; Jones, J. R.; Bronlund, J. E. (2011): Primary nucleation of alpha-lactose monohydrate. The effect of supersaturation and temperature. In *International Dairy Journal* 21 (7), pp. 455–461. DOI: 10.1016/j.idairyj.2011.01.006.
- Mimouni, Arnaud; Schuck, Pierre; Bouhallab, Saïd (2005): Kinetics of lactose crystallization and crystal size as monitored by refractometry and laser light scattering. effect of proteins. In *Le Lait* 85 (4-5), pp. 253–260. DOI: 10.1051/lait:2005015.
- Mullin, J. (1976): *Industrial Crystallization*. New York, NY: Springer. Available online at <https://ebookcentral.proquest.com/lib/kxp/detail.action?docID=6710501>.
- Mullin, J. W. (2001): *Crystallization*: Elsevier.
- Mullin, J. W.; Garside, J. (1967a): The crystallization of aluminium potassium sulphate: A study in the assessment of crystallizer design data Part I: Single crystal growth rates. In *Trans. Instn Chem. Engrs* 45, pp. 285–290.
- Mullin, J. W.; Garside, J. (1967b): The crystallization of aluminium potassium sulphate: A study in the assessment of crystallizer design data Part II: Growth in a fluidized bed crystallizer. In *Trans. Instn Chem. Engrs* 45, pp. 291–295.
- Myerson, A. S.; Trout, B. L. (2013): Chemistry. Nucleation from solution. In *Science* 341 (6148), pp. 855–856. DOI: 10.1126/science.1243022.
- Myerson, Allan S.; Erdemir, Deniz; Lee, Alfred Y. (2019): *Handbook of industrial crystallization*. Third edition. Cambridge: Cambridge University Press.
- Nagy, Zoltan K.; Fevotte, Gilles; Kramer, Herman; Simon, Levente L. (2013): Recent advances in the monitoring, modelling and control of crystallization systems. In *Chemical Engineering Research and Design* 91 (10), pp. 1903–1922. DOI: 10.1016/j.cherd.2013.07.018.
- Ochsenbein, David R.; Schorsch, Stefan; Salvatori, Fabio; Vetter, Thomas; Morari, Manfred; Mazzotti, Marco (2015): Modeling the facet growth rate dispersion of  $\beta$  l-glutamic acid—Combining single crystal experiments with nD particle size distribution data. In *Chemical Engineering Science* 133, pp. 30–43. DOI: 10.1016/j.ces.2015.02.026.
- Puel, F.; Févotte, G.; Klein, J. P. (2003): Simulation and analysis of industrial crystallization processes through multidimensional population balance equations. Part

1. a resolution algorithm based on the method of classes. In *Chemical Engineering Science* 58 (16), pp. 3715–3727. DOI: 10.1016/s0009-2509(03)00254-9.
- Puel, F.; Marchal, P.; Klein, J. (1997): Habit Transient Analysis in Industrial Crystallization Using Two Dimensional Crystal Sizing Technique. In *Chemical Engineering Research and Design* 75 (2), pp. 193–205. DOI: 10.1205/026387697523444.
- Qamar, S.; Ashfaq, A.; Warnecke, G.; Angelov, I.; Elsner, M. P.; Seidel-Morgenstern, A. (2007): Adaptive high-resolution schemes for multidimensional population balances in crystallization processes. In *Computers & Chemical Engineering* 31 (10), pp. 1296–1311. DOI: 10.1016/j.compchemeng.2006.10.014.
- Rachah, Amira; Noll, Dominikus (2015): Modeling and control of a semi-batch cooling seeded crystallizer. In. 2015 6th International Conference on Modeling, Simulation, and Applied Optimization (ICMSAO), pp. 1–6.
- Rao, Guruprasad; Aghajanian, Soheil; Koironen, Tuomas; Wajman, Radosław; Jackowska-Strumiłło, Lidia (2020): Process Monitoring of Antisolvent Based Crystallization in Low Conductivity Solutions Using Electrical Impedance Spectroscopy and 2-D Electrical Resistance Tomography. In *Applied Sciences* 10 (11), p. 3903. DOI: 10.3390/app10113903.
- Reinhold, Alexander (2015): Crystal Shape Modeling and Convex Geometry - Analysis of Geometric State Spaces. Kristallformmodellierung und Konvexgeometrie - Analyse geometrischer Zustandsräume. Dissertation. TU Munich, Freising, Germany. Fakultät Wissenschaftszentrum Weihenstephan. Available online at <https://mediatum.ub.tum.de/1226562>, checked on 9/8/2021.
- Reinhold, Alexander; Briesen, Heiko (2015): High dimensional population balances for the growth of faceted crystals. Combining Monte Carlo integral estimates and the method of characteristics. In *Chem. Eng. Sci.* 127, pp. 220–229. DOI: 10.1016/j.ces.2015.01.035.
- Reinhold, Alexander; Schorsch, Stefan; Mazzotti, Marco; Briesen, Heiko (2015): Modeling and measurement of abraded particles. In *Powder Technol.* 271, pp. 134–140. DOI: 10.1016/j.powtec.2014.10.040.
- Reischl, Daniela; Röthel, Christian; Christian, Paul; Roblegg, Eva; Ehmman, Heike M. A.; Salzmann, Ingo; Werzer, Oliver (2015): Surface-Induced Polymorphism as a Tool for Enhanced Dissolution: The Example of Phenytoin. In *Crystal Growth & Design* 15 (9), pp. 4687–4693. DOI: 10.1021/acs.cgd.5b01002.
- Ristic, R. I.; Shekunov, B.; Shewood, J. N. (1996): Long and short period growth rate variations in potash alum crystals. In *J. Cryst. Growth* 160 (3-4), pp. 330–336. DOI: 10.1016/0022-0248(95)00741-5.
- Salvatori, Fabio; Mazzotti, Marco (2018): Experimental Characterization and Mathematical Modeling of Breakage of Needle-like Crystals in a Continuous Rotor-Stator Wet Mill. In *Crystal Growth & Design* 18 (10), pp. 5957–5972. DOI: 10.1021/acs.cgd.8b00761.
- Schiele, Simon; Kovačević, Tijana; Briesen, Heiko (2020a): Morphological Modelling and Simulation of Crystallization Processes. In Stefan Heinrich (Ed.): *Dynamic Flowsheet Simulation of Solids Processes*. Cham: Springer International Publishing, pp. 435–473.
- Schiele, Simon A.; Antoni, Felix; Meinhardt, Rolf; Briesen, Heiko (2021a): Analysis of Nonideal Shape Evolution during Potash Alum Crystallization Using Microcomputed Tomography and Three-Dimensional Image Analysis. In *Cryst. Growth Des.* 21 (3). DOI: 10.1021/acs.cgd.0c01644.

- Schiele, Simon A.; Hupfer, Ricardo; Luxenburger, F.; Briesen, Heiko (2021b): Growth of abraded crystals tracked in three dimensions. In *Cryst. Growth Des.* 21 (11), pp. 6373–6384. DOI: 10.1021/acs.cgd.1c00849.
- Schiele, Simon A.; Meinhardt, Rolf; Eder, Cornelia; Briesen, Heiko (2020b): ATR-FTIR spectroscopy for in-line anomer concentration measurements in solution. A case study of lactose. In *Food Control* 110. DOI: 10.1016/j.foodcont.2019.107024.
- Schmalenberg, Mira; Krell, Tobias; Mathias, Christopher; Kockmann, Norbert (2021): Continuous Miniaturized Draft Tube Baffle Crystallizer with Particle Screw for Supportive Suspension Discharge. In *Ind. Eng. Chem. Res.* DOI: 10.1021/acs.iecr.1c03748.
- Schmideder, Stefan; Müller, Henri; Barthel, Lars; Friedrich, Tiaan; Niessen, Ludwig; Meyer, Vera; Briesen, Heiko (2021): Universal law for diffusive mass transport through mycelial networks. In *Biotechnology and bioengineering* 118 (2), pp. 930–943. DOI: 10.1002/bit.27622.
- Schorsch, Stefan; Ochsenbein, David R.; Vetter, Thomas; Morari, Manfred; Mazzotti, Marco (2014): High accuracy online measurement of multidimensional particle size distributions during crystallization. In *Chem. Eng. Sci.* 105, pp. 155–168. DOI: 10.1016/j.ces.2013.11.003.
- Simone, Elena; Tyler, Arwen I. I.; Kuah, Daniel; Bao, Xiaofan; Ries, Michael E.; Baker, Daniel (2019): Optimal Design of Crystallization Processes for the Recovery of a Slow-Nucleating Sugar with a Complex Chemical Equilibrium in Aqueous Solution. The Case of Lactose. In *Organic Process Research & Development* 23 (2), pp. 220–233. DOI: 10.1021/acs.oprd.8b00323.
- Skorych, Vasyl; Dosta, Maksym; Hartge, Ernst-Ulrich; Heinrich, Stefan (2017): Novel system for dynamic flowsheet simulation of solids processes. In *Powder Technology* 314, pp. 665–679. DOI: 10.1016/j.powtec.2017.01.061.
- Snyder, Ryan C.; Doherty, Michael F. (2007): Faceted crystal shape evolution during dissolution or growth. In *AIChE J.* 53 (5), pp. 1337–1348. DOI: 10.1002/aic.11132.
- Snyder, Ryan C.; Studener, Stephan; Doherty, Michael F. (2007): Manipulation of crystal shape by cycles of growth and dissolution. In *AIChE J.* 53 (6), pp. 1510–1517. DOI: 10.1002/aic.11174.
- Tung, Hsien-Hsin (2012): Industrial Perspectives of Pharmaceutical Crystallization. In *Organic Process Research & Development* 17 (3), pp. 445–454. DOI: 10.1021/op3002323.
- Ulrich, Joachim; Stepanski, Manfred (1987): Einfluß der Oberflächen-Beschaffenheit auf das Kristallwachstum aus Lösungen. In *Chem. Ing. Tech.* 59 (5), pp. 402–404. DOI: 10.1002/cite.330590508.
- Variankaval, Narayan; Cote, Aaron S.; Doherty, Michael F. (2008): From form to function. Crystallization of active pharmaceutical ingredients. In *AIChE J.* 54 (7), pp. 1682–1688. DOI: 10.1002/aic.11555.
- Vekilov, P. G. (2019): Crystallization tracked atom by atom. In *Nature* 570 (7762), pp. 450–452. DOI: 10.1038/d41586-019-01965-2.
- Wang, G. C.; Wang, Q.; Li, S. L.; Ai, X. G.; Fan, C. G. (2014): Evidence of multi-step nucleation leading to various crystallization pathways from an Fe-O-Al melt. In *Sci Rep* 4 (1), p. 5082. DOI: 10.1038/srep05082.
- Wiedenbeck, E.; Kovermann, M.; Gebauer, D.; Colfen, H. (2019): Liquid Metastable Precursors of Ibuprofen as Aqueous Nucleation Intermediates. In *Angew Chem Int Ed Engl.* DOI: 10.1002/anie.201910986.

Zhang, Yongchun; Doherty, Michael F. (2004): Simultaneous prediction of crystal shape and size for solution crystallization. In *AIChE J.* 50 (9), pp. 2101–2112. DOI: 10.1002/aic.10182.

Zhou, J.; Yang, Y.; Kim, D. S.; Yuan, A.; Tian, X.; Ophus, C. et al. (2019): Observing crystal nucleation in four dimensions using atomic electron tomography. In *Nature* 570 (7762), pp. 500–503. DOI: 10.1038/s41586-019-1317-x.



# Appendix A

## List of Publications

### Journals and Books

**Schiele, S.**; Hupfer, R.; Luxenburger, F.; Briesen, H. (2021): „*Growth of abraded crystals tracked in three dimensions.*“, Cryst. Growth Des. 21 (11), <https://doi.org/10.1021/acs.cgd.1c00849>.

Olokede, O.; Hsu, S.; **Schiele, S.**; Ju, H.; Holtzapfle, M. (2021): „*Assessment of shock pretreatment and alkali pretreatment on corn stover using enzymatic hydrolysis.*“, Biotechnol Progress, e3217. <https://doi.org/10.1002/btpr.3217>.

**Schiele, S.**; Antoni, F.; Meinhardt, R.; Briesen, H. (2021): „*Analysis of Nonideal Shape Evolution during Potash Alum Crystallization Using Microcomputed Tomography and Three-Dimensional Image Analysis.*“, Cryst. Growth Des. 21 (3). <https://doi.org/10.1021/acs.cgd.0c01644>.

Krüger M., Oosterhoff L., van Wolferen M., **Schiele S.**, Walther A., Geijssen N., De Laporte L., van der Laan L., Kock L., Spee B. (2020) „*Cellulose Nanofibril Hydrogel Promotes Hepatic Differentiation of Human Liver Organoids*“, Advanced Healthcare Materials 9 (6), <https://doi.org/10.1002/adhm.201901658>

**Schiele S.**, Kovačević T., Briesen H. (2020) Morphological Modelling and Simulation of Crystallization Processes. In: Heinrich S. (eds) Dynamic Flowsheet Simulation of Solids Processes. Springer, Cham. [https://doi.org/10.1007/978-3-030-45168-4\\_13](https://doi.org/10.1007/978-3-030-45168-4_13)

**Schiele S.**, Meinhardt R., Eder C., Briesen H. (2020) “*ATR-FTIR spectroscopy for in-line anomer concentration measurements in solution: A case study of lactose*”, Food Control 110, <https://doi.org/10.1016/j.foodcont.2019.107024>

### Presentations at Conferences

**Schiele A.**, Hupfer R., Briesen H. (2021) “*3D imaging yields a physical explanation for growth rate dispersion and size dependent growth*” at 21<sup>st</sup> International Symposium on Industrial Crystallization, online conference

**Schiele A.**, Hupfer R., Eder C., Briesen H. (2021) “*Wachstumsanalyse von beschädigten Kristallen in 3D*” at the annual meeting of the ProcessNET working party on crystallization, online conference

**Schiele S.**, Antoni F., Meinhardt R., Briesen H. (2020) “*3D-Morphologiecharakterisierung einer Kristallisation*” at Jour Fixe Kristallisation (replacement of the annual meeting of the ProcessNET working party on crystallization), online conference

**Kulozik S.**, Kovačević T., Buchholz M., Haus J., Heinrich S., Briesen H. (2019) “*Dynamic Flowsheet Simulation of a Crystallization Reactor with Material Recovery via a Hydrocyclone*” at Partec, Nuremberg (Germany)

**Kulozik S.**, Kovačević T., Buchholz M., Haus J., Heinrich S., Briesen H. (2019) “*Dynamische Modellierung eines Kristallisationsprozesses mit Rückführung*” at the annual meeting of the ProcessNET working party on crystallization, Bamberg (Germany)

### Poster Presentations

**Schiele S.**, Briesen H. (2021) “*Growth of crystals tracked in 3D*” at 21<sup>st</sup> International Symposium on Industrial Crystallization, online conference, best poster award

**Schiele S.**, Meinhardt R., Eder C., Briesen H. (2021) "*Inline Übersättigungsmessung bei der Laktosekristallisation*" at the annual meeting of the ProcessNET working party on crystallization, online conference

**Kulozik S.**, Kovačević T., Briesen H. (2019) „*Präparation von Kristallen für umfassende Micro-Computertomographische Morphologiecharakterisierung*“ at the annual meeting of the ProcessNET working party on crystallization, Bamberg (Germany)